

2016-01-16

Complex Resistivity Spectra in Relation to Multiscale Pore Geometry in Carbonates and Mixed-Siliciclastic Rocks

Jan Henrik Norbistrath
University of Miami, jan.norbistrath@gmail.com

Follow this and additional works at: https://scholarlyrepository.miami.edu/oa_dissertations

Recommended Citation

Norbistrath, Jan Henrik, "Complex Resistivity Spectra in Relation to Multiscale Pore Geometry in Carbonates and Mixed-Siliciclastic Rocks" (2016). *Open Access Dissertations*. 1573.
https://scholarlyrepository.miami.edu/oa_dissertations/1573

This Open access is brought to you for free and open access by the Electronic Theses and Dissertations at Scholarly Repository. It has been accepted for inclusion in Open Access Dissertations by an authorized administrator of Scholarly Repository. For more information, please contact repository.library@miami.edu.

UNIVERSITY OF MIAMI

COMPLEX RESISTIVITY SPECTRA IN RELATION TO MULTISCALE PORE
GEOMETRY IN CARBONATES AND MIXED-SILICICLASTIC ROCKS

By

Jan Henrik Norbistrath

A DISSERTATION

Submitted to the Faculty
of the University of Miami
in partial fulfillment of the requirements for
the degree of Doctor of Philosophy

Coral Gables, Florida

May 2016

©2016
Jan Henrik Norbistrath
All Rights Reserved

UNIVERSITY OF MIAMI

A dissertation submitted in partial fulfillment of
the requirements for the degree of
Doctor of Philosophy

COMPLEX RESISTIVITY SPECTRA IN RELATION TO MULTISCALE PORE
GEOMETRY IN CARBONATES AND MIXED-SILICICLASTIC ROCKS

Jan Henrik Norbistrath

Approved:

Gregor P. Eberli, Ph.D.
Professor of Marine Geology
and Geophysics

Keir Becker, Ph.D.
Professor of Marine Geology
and Geophysics

Guoqing Lin, Ph.D.
Assistant Professor of Marine Geology
and Geophysics

Dean of the Graduate School

Ralf J. Weger, Ph.D.
Associate Scientist in Marine Geology
and Geophysics

Klaas Verwer, Ph.D.
Principal Exploration Geologist
Statoil ASA, Stavanger, Norway

NORBISRATH, JAN HENRIK

(Ph.D., Marine Geology and Geophysics)

Complex Resistivity Spectra in
Relation to Multiscale Pore Geometry
in Carbonates and Mixed-Siliciclastic Rocks

(May 2016)

Abstract of a dissertation at the University of Miami.

Dissertation supervised by Professor Gregor P. Eberli.

No. of pages in text. (186)

Carbonate rocks are known to have complex and heterogeneous pore structures, which result from their biogenic origin and strong affinity for diagenetic processes that change their pore structure after burial. The combination of sheer endless variations of precursor biogenic material, depositional environments, and diagenetic effects results in rocks that are interesting to study but intricate to understand.

Many schemes to categorize the diversity of carbonate rocks are in use today; most are based on the macropore structure and qualitative thin-section analysis. Many studies, however, acknowledge that micropores have a significant influence on the macroscopic petrophysical rock properties, which are essential to determine reservoir quality. Micropores are, by definition, smaller than the thickness of a thin-section ($< 30 \mu\text{m}$) and hence cannot be quantified with conventional methods. For their analysis, scanning electron microscopy (SEM) is the logical next step. The challenge is that mechanical polishing methods produce excessive surface roughness at micron scale; the resulting surfaces are not suited for quantification of micropores. Advances in broad-ion-beam (BIB) milling enable preparation of nanometer-precision 2D sections that are suited for quantitative analysis with the SEM. To accomplish the objective of accurate quantification

of carbonate micropores, part one of this dissertation employs the BIB-SEM technique on a variety of carbonate rock samples and finds four major carbonate microporosity types: (1) small intercrystalline, (2) large inter-crystalline, (3) intercement, and (4) micromoldic. Each microporosity type shows a distinct capacity to conduct electrical charge, which largely controls the magnitude and range of cementation factors (m) in rocks with such microporosity type. The BIB-SEM method is also used on a dataset of mixed carbonate-siliciclastic (mudrock) samples with high kerogen and pyrite content. Results show that the nanopore geometry here has little influence on cementation factors, and instead porosity is the main control on m in mudrocks.

Cementation factors are crucial for estimates of oil-in-place and water saturation in a wireline application, and a slight change of (assumed) cementation factor can change the interpreter's evaluation from dry hole to discovery. Therefore, accurate determination of cementation factors is a critical task in formation evaluation, similar to accurate estimates of permeability. To achieve this goal, this dissertation utilizes a new approach of using complex resistivity spectra (CRS) to assess the pore geometry and its resulting electrical and fluid flow properties. Specifically, frequency dispersion of complex resistivity in the kHz range is used as input for a new model to predict cementation factor and permeability in a wide variety of core plug samples. The underlying concept that relates CRS to flow properties is that both are related to pore geometry. CRS are linked to pore geometry by interfacial polarization effects at the fluid-rock boundary that control the phase and amplitude shift of an applied alternating current. Larger interfacial area results in higher phase shifts, but also indicates a more intricate pore structure that often results in lower permeability and higher cementation factors.

The findings from this dissertation imply that (1) the CRS prediction method greatly improves estimates of cementation factors and permeability in carbonate, dolomite, and mixed siliciclastic rocks, (2) there are at least four distinct microporosity types in carbonate rocks, which have great impact on cementation factors and permeability, (3) nanopore geometry has a small impact on electrical flow properties in mudrocks where the main control on cementation factors is porosity, and (4) all sedimentary limestone and mixed carbonate-siliciclastic rocks have power law pore size distributions.

TABLE OF CONTENTS

	Page
LIST OF FIGURES	vii
LIST OF TABLES	xv
Chapter	
1 INTRODUCTION	1
Rationale	1
Previous Work	1
<i>Digital Image Analysis (DIA)</i>	3
<i>Micro-Computed Tomography (μ-CT)</i>	3
Broad-Ion-Beam Scanning Electron Microscopy (BIB-SEM).....	3
<i>Mudrock Nanoporosity</i>	5
<i>Carbonate Microporosity types</i>	5
<i>Multiscale Digital Image Analysis (MsDIA)</i>	6
Electrical Resistivity	7
<i>Mode of Conduction</i>	8
<i>Archie's Equations and Cementation Factor m</i>	8
<i>Calculations of Water Saturations</i>	9
Complex Electrical Resistivity	11
<i>Complex Resistivity Spectra (CRS)</i>	12
Working Hypotheses.....	13
2 ELECTRICAL AND FLUID FLOW PROPERTIES OF CARBONATE MICROPOROSITY TYPES FROM MULTISCALE DIGITAL IMAGE ANALYSIS AND MERCURY INJECTION.....	17
Summary	17
Introductory Remarks	18
<i>Data Set</i>	21
Methods.....	22
<i>Porosity, Permeability Measurements</i>	22
<i>Electrical Resistivity</i>	22
<i>Broad-Ion-Beam Milling with Subsequent Scanning Electron Microscopy Image Mosaic Acquisition</i>	23
<i>Multiscale Digital Image Analysis</i>	25
<i>Dominant Pore Size</i>	26
<i>Perimeter over Area</i>	27
<i>Normalized Pore Density</i>	27
<i>Pore Body-to-Throat Ratio</i>	28
<i>Pore-Size Distribution and Fractal Dimension D</i>	28
<i>Mercury Injection Capillary Pressure: Critical Pore-Throat Diameter</i>	29

Results.....	30
<i>BIB-SEM Mosaics</i>	30
<i>Types of Microporosity</i>	30
<i>Microstructure in the Various Samples</i>	31
<i>Multiscale Digital Image Analysis: Quantified Pore Geometric Parameters</i>	34
<i>Power Law Pore-Size Distributions and Fractal Dimension D</i>	37
<i>Mercury Injection Capillary Pressure: Critical Pore-Throat Diameter</i>	38
Discussion.....	40
<i>Multiscale Pore Geometries</i>	40
<i>Types of Microporosity</i>	41
<i>Fractal Pore Space</i>	43
<i>Mercury Injection Capillary Pressure: Critical Pore-Throat Diameter</i>	46
<i>Pore Body-to-Throat Ratio</i>	47
<i>Permeability versus Conductivity</i>	49
Conclusion and Implications.....	51
3 FRACTAL PORE STRUCTURE AND COMPLEX RESISTIVITY SPECTRA (CRS) FOR ESTIMATING PERMEABILITY IN DOLOMITES FROM THE MISSISSIPPIAN MADISON FORMATION, WYOMING.....	54
Summary.....	54
Introductory Remarks	55
<i>Complex electrical properties of porous media</i>	56
<i>Complex resistivity spectra (CRS)</i>	58
Methods.....	58
<i>General Methods</i>	58
<i>Spectral analysis of complex resistivity</i>	59
Dataset.....	61
Results.....	62
<i>Pore Structure</i>	62
<i>Crystal size</i>	62
<i>DOMsize and PoA</i>	63
<i>Power law pore size distribution</i>	64
<i>Porosity-permeability</i>	66
<i>Acoustic velocity</i>	66
<i>Cementation factor m</i>	68
<i>Pressure dependency of resistivity</i>	68
<i>Complex resistivity spectra (CRS)</i>	70
Discussion.....	73
<i>Crystal size and Pore Structure</i>	73
<i>Cementation factor m and pressure dependency</i>	74
<i>Complex resistivity spectra (CRS)</i>	75
<i>Well-logging applications</i>	76
Conclusions and Implications.....	78
4 COMPLEX RESISTIVITY SPECTRA AND PORE GEOMETRY FOR PREDICTIONS OF RESERVOIR PROPERTIES IN CARBONATE ROCKS	80

Summary	80
Introductory Remarks	81
<i>Complex electrical resistivity and dielectric dispersion</i>	82
Methods.....	84
<i>Porosity and permeability</i>	84
<i>Pore geometry (PoA, DOMsize, Slope D)</i>	84
<i>Complex resistivity spectra</i>	85
<i>Parameter predictions</i>	87
Dataset.....	88
Results.....	89
<i>Porosity, permeability, and cementation factor m</i>	89
<i>PoA and DOMsize</i>	91
<i>Slope D</i>	93
<i>Predictions from DIA</i>	95
<i>Complex Resistivity Spectrum</i>	98
<i>CRS vs. DIA</i>	99
<i>Predictions from CRS</i>	100
Discussion.....	103
<i>Pore geometry</i>	103
<i>Fractal pore area distributions</i>	104
<i>Predictions from pore geometry</i>	105
<i>Complex resistivity spectra</i>	105
<i>Predictions from CRS</i>	107
<i>CRS frequency range</i>	108
<i>Challenges</i>	109
<i>Technology for wireline applications</i>	110
<i>Future work: temperature, salinity, and water saturation effects on dielectric properties</i>	111
Conclusion.	112
5 NANOPORE IMAGING IN VACA MUERTA MUDROCKS TO EVALUATE CONTROLS ON COMPLEX RESISTIVITY SPECTRA IN UNCONVENTIONAL RESERVOIRS.....	115
Summary.....	115
Introductory Remarks	116
Electrical charges in mudrocks	117
Dataset.....	119
Methods.....	119
<i>Acid washing, elemental analysis, and humidity drying</i>	119
<i>BIB-SEM and pore geometries</i>	120
<i>Image processing</i>	122
<i>DOMsize and PoA</i>	122
<i>Interfacial Surface Area (2D)</i>	123
<i>Slope D</i>	123
<i>Cementation factors</i>	124
<i>Complex resistivity spectra (CRS)</i>	125

<i>Predictions of reservoir properties</i>	125
Results	126
<i>TOC and CO₃ content</i>	126
<i>Cementation factor <i>m</i> and porosity</i>	126
<i>Pressure dependency of <i>m</i></i>	129
<i>Irreducible water saturation (<i>S_w_{irr}</i>)</i>	133
<i>BIB-SEM</i>	133
<i>Pore structure analysis</i>	134
<i>Pore geometry parameters</i>	135
<i>2-dimensional Interfacial Surface Area (ISA2D)</i>	136
<i>Fractal analysis</i>	138
Discussion of cementation factors, mineralogy, and pore geometry	140
<i>Cementation factors</i>	140
<i>TOC & CO₃</i>	140
<i>Porosity</i>	141
<i>Cementation factors and pyrite</i>	142
<i>Pressure dependency of cementation factors</i>	142
<i>Micropores and <i>S_w_{irr}</i></i>	143
<i><i>S_w_{irr}</i> and CRS</i>	144
<i>BIB-SEM</i>	145
<i>Nanopore geometry</i>	144
<i>Fractals</i>	146
<i>Mudrock vs carbonate nanoporosity</i>	145
<i>Limitations in the pore geometry analysis on BIB-SEM images</i>	149
Complex resistivity spectra (CRS).....	150
<i>Frequency range and slopes</i>	150
<i>CRS slopes vs porosity and Formation Factor</i>	152
<i>CRS slopes vs ISA2D, DOMsize, and PoA</i>	153
<i>CRS slopes vs TOC, CO₃, and <i>S_w_{irr}</i></i>	155
<i>Predictions of TOC, CO₃, <i>S_w_{irr}</i></i>	156
<i>Predictions of porosity and ISA2D</i>	157
<i>Predictions of cementation factors</i>	159
Discussion of CRS	162
<i>Pore geometry and porosity</i>	162
<i>Formation Factor & Cementation factor <i>m</i></i>	163
<i>Wireline application</i>	165
Conclusion	165
6 SUMMARY	167
Rationale	167
Outcome	168
Implications.....	168
Conclusion	169
REFERENCES.....	172

LIST OF FIGURES

	Page
Figure 1.1: Plot from Verwer (2011), showing that small and complex pores (low DOMsize and high PoA) result in lower cementation factors.....	2
Figure 1.2: Comparison of surface roughness from mechanical polishing (top and left) and broad-ion-beam milling (right).....	4
Figure 1.3: Schematic of image acquisition for Multiscale Digital Image Analysis (MsDIA).....	7
Figure 2.1: Zoom into the pore structure of stromatolitic ooid bindstone.....	19
Figure 2.2: Stromatolitic ooid bindstone with segmented microporosity in red.....	21
Figure 2.3: Overviews of the broad ion beam (BIB) cross-sectioned areas in four carbonate rock types with distinct types of microporosity, showing their different macropore structures.....	32
Figure 2.4: Four types of microporosity at 15,000× magnification from broad-ion-beam milling coupled with scanning electron micro- scope (BIB-SEM) mosaics, showing their distinct microstructures at nanometer scales.....	33
Figure 2.5: Quantified pore structure parameters plotted against cementation factor, color-coded with permeability.....	36
Figure 2.6: Pore-size distributions (PSD) of the 12 carbonate rocks. Logarithm of normalized pore frequencies (y-axis) as function of logarithm of pore-size bin (x-axis), using nonlinear binning (subsequent bin sizes doubling in size).	37
Figure 2.7: Fractal dimension D of pore-size distribution plotted against cementation factors, color coded with permeability.....	38

Figure 2.8: Normalized mercury injection capillary pressure intrusion curves, color coded with cementation factors.....	39
Figure 2.9: Zoom into pore structure of ooid bindstone, demonstrating the self-similarity of the pore space at different scales.....	44
Figure 2.10: Concept of tortuosity (a) as in deviation from a straight line without tortuosity (top: a = 1.0).....	48
Figure 3.1: Stitched photomicrographs of two blue epoxy impregnated dolomite samples from the Madison Formation with significantly different crystal sizes but similar petrophysical properties.....	61
Figure 3.2: Three dolomite samples with different crystal sizes.....	63
Figure 3.3: Plot of PoA vs DOMsize for samples with more than 10% porosity, color-coded with cementation factors.....	64
Figure 3.4: Pore size distributions of 54 dolomite samples acquired with digital image analysis on thin-sections, plotted on log-log scale using non-linear binning (subsequent bin sizes doubling in size).....	65
Figure 3.5: Two plots, both color-coded with slope D of power law PSD.....	65
Figure 3.6: Left: Porosity-permeability cross-plot for 54 dolomite samples from the Madison Fm, showing good correlation of porosity with permeability ($R^2 = 0.60$).....	66
Figure 3.7: Porosity-Vp/Vs ratio cross-plot for 54 dolomite samples from the Madison Formation, color-coded with dominant pore size.....	67
Figure 3.8: Porosity-permeability cross-plot.....	68
Figure 3.9: Plot of confining pressure vs cementation factor m demonstrates the minor	

effect of increasing pressure and overburden on electrical properties and pore structure.....	69
Figure 3.10: Top: Amplitude of resistivity as function of frequency of 54 dolomite samples at 20 MPa effective pressure, color-coded with porosity.....	70
Figure 3.11: Top: Amplitude of resistivity as function of frequency of 54 dolomite samples at 20 MPa effective pressure, color-coded with permeability.....	71
Figure 3.12: Cross-plot of measured permeability vs. estimated permeability from the model (Eq. 3.2).....	73
Figure 4.1: Polarization effects at different frequency ranges and length scales (modified from Ellis & Singer, 2007).....	83
Figure 4.2: Example of amplitude and phase shift curves of complex resistivity for a single sample.....	87
Figure 4.3: Cross-plots of porosity vs flow properties for 330 carbonate core plug samples that are color-coded according to individual datasets.....	90
Figure 4.4: Scatterplot of Perimeter over Area (PoA) versus Dominant Pore Size (DOMsize) for the individual datasets that have been combined for this study.....	92
Figure 4.5: Cross-plots of Perimeter over Area (PoA) vs. Dominant Pore Size (DOMsize), color-coded with permeability (left) and cementation factor m (right).....	93
Figure 4.6: Pore size distributions of 330 carbonate samples acquired with digital image analysis on thin-sections, plotted on log-log scale using non-linear binning in order of their Slope D.....	94

Figure 4.7: Permeability predictions from resistivity and DIA (Eq. 4.5) for entire dataset with constants abcd defined for individual sub-datasets (left) and with constants abcd defined for entire dataset (right).....	96
Figure 4.8: Cementation factor m predictions from porosity and DIA (Eq. 4.6) for entire dataset with constants abcd defined for individual sub-datasets (left) and with constants abcd defined for entire dataset (right).....	97
Figure 4.9: Complex resistivity amplitude (top) and phase spectra (bottom) of 330 carbonate plug samples, color-coded with permeability (left) and formation factors (right).....	98
Figure 4.10: Cross-plots of Perimeter over Area (PoA) vs. Dominant Pore Size (DOMsize), color-coded with β amplitude (left) and β phase (right), illustrating link of CRS parameters to pore geometry.....	100
Figure 4.11 Permeability predictions from resistivity and CRS (Eq. 4.7) for entire dataset with constants abcd defined for individual subsets (left) and with constants abcd defined for entire dataset (right).....	101
Figure 4.12: Cementation factor m predictions from porosity and CRS (Eq. 4.8) for entire dataset with constants abcd defined for individual sub-sets (left) and with constants abcd defined for entire dataset (right).....	102
Figure 5.1: Span of polarization mechanisms in the frequency domain after Hizem et al. (2008).....	118
Figure 5.2: Example of un-cropped broad-ion-beam milling scanning electron microscopy (BIB-SEM) mosaic of sample P27_2a at 15,000x magnification, consisting of 50 SEM images.....	121

Figure 5.3: Broad-ion-beam (BIB) milled area with scanning electron microscopy images at increasing magnification from left to right, illustrating low surface roughness and quantifiable mudrock pore structure.....	122
Figure 5.4: Cross-plot of TOC and CO ₃ of 56 mudrock samples from the Vaca Muerta Formation, indicating trend of lower organic carbon at higher levels of carbonate content.....	126
Figure 5.5: Cementation factors of 56 Vaca Muerta mudrocks vs. porosity (top), total organic carbon (TOC; middle), and carbonate content (CO ₃ ; bottom).....	127
Figure 5.6: Cross-plot of cementation factors m measured at 5 MPa vs 53 MPa confining pressure, grayscale indicates porosity.....	130
Figure 5.7: Plot of confining pressure vs cementation factor m	131
Figure 5.8: Effective pressure (EP) vs cementation factor for increasing and decreasing pressure leg (2 Mpa - 50 Mpa - 2 MPa), color-coded with percental increase in cementation factor (top) and amount of hysteresis after pressure cycle (bottom).....	132
Figure 5.9: Left: Cross-plot of irreducible water saturation ($S_{w_{irr}}$) and carbonate content (CO ₃), color-coded with percentage of porosity.....	133
Figure 5.10: Examples of minerals and organic matter (OM) in Vaca Muerta mudrocks in broad-ion-beam milling scanning electron microscopy (BIB-SEM) images at 50,000x magnification.....	134
Figure 5.11: Two broad-ion-beam milling SEM mosaics consisting of 50 images each at 15,000x magnification and 9.6 nm pixel side length.....	135

Figure 5.12: Cross-plot of Perimeter over Area (PoA) and Dominant pore size (DOMsize), color-coded with cementation exponent m	136
Figure 5.13: Cross-plot of cementation factor m vs pore geometry on y-axis, color-coded with porosity.....	137
Figure 5.14: Double-logarithmic plot of pore size bin centers vs normalized pore density per bin, indicating a power-law pore size distribution.....	138
Figure 5.15: Cross-plot of optical porosity (Phi _{opt}) from BIB-SEM mosaics vs 2-dimensional Specific Surface Area (SSA2D) demonstrates many times higher complexity of nanoporosity in mudrocks as compared to carbonates.....	147
Figure 5.16: Cross-plot of Perimeter over Area (PoA) vs Dominant pore size (DOMsize) for both carbonates and mudrocks with color-coded m	148
Figure 5.17: Comparison of pore geometry in a (a) mudrock and (b) carbonate sample with equal helium porosity of ~3.6 %, illustrating the increased nanopore complexity of a typical mudrock.....	149
Figure 5.18: Plot of frequency vs resistivity amplitude (resistance R; top) and resistivity phase (reactance iX ; bottom).....	151
Figure 5.19: Correlation between the slope of phase and amplitude frequency dispersion of 56 mudrock samples in 10 – 100 kHz range ($\beta_{\text{amplitude}}$ and β_{phase}).....	152
Figure 5.20: Complex resistivity spectra (top: resistance R; bottom: reactance iX) in the 10 – 100 kHz range, color-coded with porosity (left) and Formation Factor (right).....	153

Figure 5.21: Complex resistivity spectra (top: resistance R; bottom: reactance iX) in the 10 – 100 kHz range, color-coded with amount of Specific Surface Area (SSA2D; left), Dominant pore size (DOMsize; middle), and Perimeter over Area (PoA; right).....	154
Figure 5.22: Complex resistivity spectra (top: resistance R; bottom: reactance iX) in the 10 – 100 kHz range, color-coded with amount of total organic carbon (TOC; left), carbonate content (CO ₃ ; middle), and irreducible water saturation on a subset of 13 samples (S _w _{irr} ; right).....	155
Figure 5.23: Predictions of total organic carbon (TOC; top), carbonate content (CO ₃ ; middle), and irreducible water saturation (S _w _{irr} ; bottom) from CRS parameters β amplitude and β phase alone using Equation 5.6 (left) and including porosity using Equation 5.7 (right).....	157
Figure 5.24: Predictions of 2-dimensional Interfacial Surface Area (SSA2D; left) and porosity (right) from resistivity alone using Equation 5.8 (top) and including CRS parameters β amplitude and β phase using Equation 5.9 (bottom).....	159
Figure 5.25: Predictions of cementation factor m from porosity using Equation 5.10 (left), porosity and DIA parameters using Equation 5.11 (middle), and from porosity and CRS slopes using Equation 5.12 (right).....	160
Figure 5.26: Predictions of cementation factor <i>m</i> in 56 mudrock core plug samples from porosity using Equation 5.10 (left), from porosity and CRS slopes using Equation 5.12 (middle), and using Equation 5.15 that was defined on a smaller subset of 23 BIB-SEM samples (right).....	120
Figure 5.27: Cross-plots of porosity and Formation Factor, grayscale-coded with real	

slope of CRS (β amplitude; left) and imaginary slope of CRS (β phase; right) at
50 MPa effective pressure..... 163

Figure 5.28: Predictions of cementation factor m on the entire mudrock dataset, using
constants defined on smaller subset of 23 BIB-SEM samples (circles) and on a
very heterogeneous carbonate dataset from a previous study (filled diamonds;
Norbisrath et al., in press)..... 164

LIST OF TABLES

Page	
Table 1.1.....	10
Table 2.1.....	31
Table 2.2.....	43
Table 4.1.....	95
Table 5.1.....	128
Table 5.2.....	139

Chapter 1: Introduction

Rationale

Carbonate rocks host more than half of the world's remaining conventional oil reserves, yet they often have highly complex pore structures frequently linked to abundant microporosity. This strongly influences their sonic, hydraulic, and electrical properties (Eberli et al., 2003; Weger et al., 2009; Skalinski & Kenter, 2015). Microporosity in particular has shown to have a strong effect on electrical resistivity, often significantly lowering cementation factors (Verwer et al, 2011). On the other hand, predominantly microporous rocks typically are impermeable and hydrocarbon extraction requires flow stimulation methods like fracking. Ever rising energy demands, however, will give more and more significance to production from these microporous 'tight oil' and source rock unconventional plays in the future (Jackson & Smith, 2014). Formation evaluation in these tight intervals requires a profound understanding of how microporosity affects petrophysical properties in order to find producible zones in carbonates and 'frackable sweet spots' in unconventional reservoirs. For these reasons, the main goal of this dissertation is to accurately quantify and assess the influence of carbonate and mudrock microporosity for petrophysical applications.

Previous Work

Previous studies have documented the importance of macropore geometric parameters in influencing the electrical behavior of rocks (Figure 1.1; Verwer, 2011). Quantitative image parameters derived using Digital Image Analysis (DIA) on thin-sections suggest that pore network size (Dominant pore size - DOMsize) and complexity of the pore system

(Perimeter over Area - PoA) are the main controlling factors influencing cementation exponents.

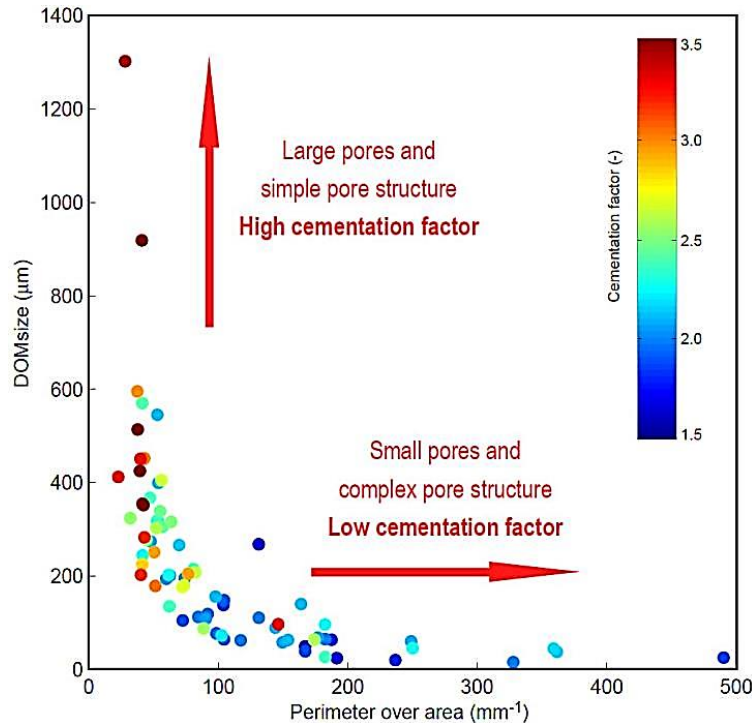


Figure 1.1: Plot from Verwer (2011), showing that small and complex pores (low DOMsize and high PoA) result in lower cementation factors. Data acquired with digital image analysis (DIA) on thin-sections (limited resolution: $\sim 20 \mu\text{m} / \text{pixel}$).

However, these studies also suggest that microporosity creates favorable conditions for electrical flow. Verwer (2011) hypothesized that a high number of small pores create a high number of electrically conductive pathways with a large combined cross-sectional area that increases conductivity. This theory sparked the interest in microporosity and highlighted the need for a method to accurately quantify it. Previously used and newly implemented imaging methods are described below.

Digital Image Analysis (DIA)

Conventional thin-section analysis is an important tool to study aspects of the macroporosity, but is not suitable to study microporosity. The resolution of standard thin-section DIA as described in Weger (2006) is mainly limited by the thickness of the thin-section itself; only pores with diameters exceeding the thickness of the thin-section (usually 10-30 μm) can be observed. This limitation explicitly excludes microporosity, commonly defined as pores $< 2 \mu\text{m}$ (Hulea & Nicholls, 2012) or simply as pores significantly smaller than those contributing to the rock's permeability (Swanson, 1985). This fact makes thin-section DIA insufficient to study microporosity in carbonates or the even more intricate mixed carbonate-siliciclastic rocks.

Micro-Computed Tomography (μ -CT)

Attempts to study microporosity with 3D μ -CT (computed tomography) methods have demonstrated that the method is also insufficient to accurately quantify microporosity. This is due to a lack of resolution, as the lower voxel size threshold usually is around 1 μm , but also due to lack of computational and storage capabilities of today's cluster computing facilities (Norbisrath et al., 2011). The latter primarily affects the amount of samples that can be analyzed, which conflicts with the intention to find common pore geometric parameters in various carbonate rock types.

Broad-Ion-Beam Scanning Electron Microscopy (BIB-SEM)

Recent adaptation of broad-ion-beam milling (BIB) for flat surface preparation enables accurate 2D quantification of microporosity with scanning electron microscopy (SEM) (Desbois et al, 2011; Laurich et al., 2014). Micropore quantification with the SEM requires surfaces to be smooth at the scale of investigation, which conventional mechanical methods

cannot achieve as they leave excessive surface topography. The BIB-milling step achieves nanometer-precision flat surfaces (Figure 1.2).

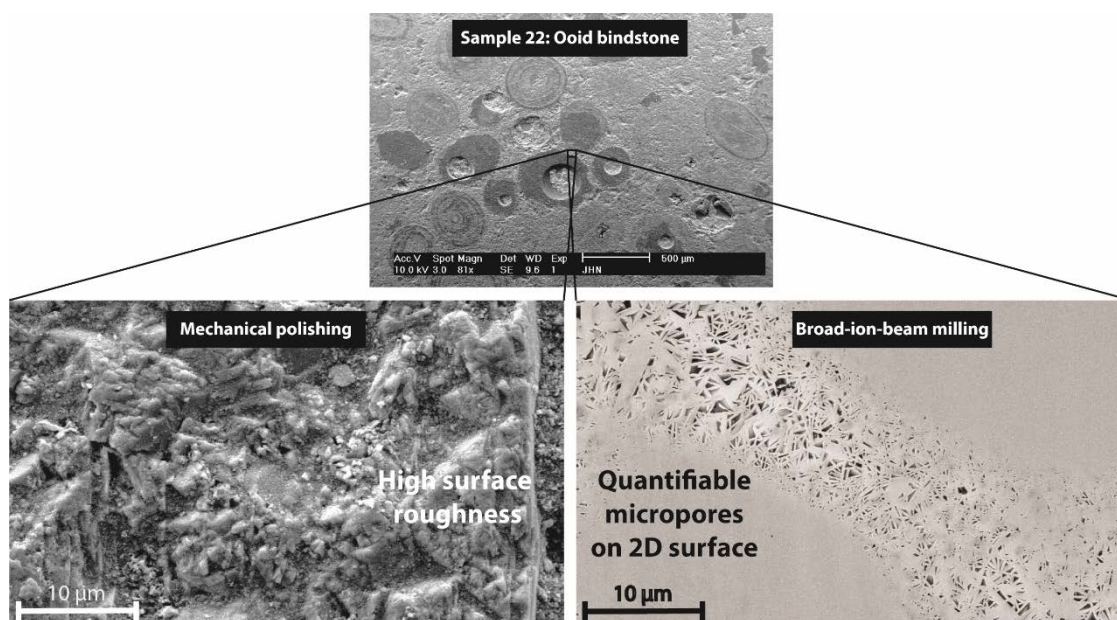


Figure 1.2. Comparison of surface roughness from mechanical polishing (top and left) and broad-ion-beam milling (right). At higher magnifications (bottom images), excessive surface roughness (high “topography”) becomes visible in mechanically polished surfaces (top and left). BIB-milling produces true 2D surfaces with clearly outlined pores, making micropores quantifiable (right).

The pre-polished surface is milled down with an argon ion-beam to a roughness of ± 5 nm. The resulting 2-dimensional surfaces are then imaged with the SEM. Large image rasters of several tens or hundreds of images are acquired with a modern Field Emission FE-SEM, stitched into mosaics, and then segmented into pore phase and solid phase. To reduce the SEM’s characteristic large depth of field and prevent occlusion of the smallest pores, low accelerating voltages (5kV) and short sputtering times (20 seconds Au/Pd coating) have to be implemented.

The BIB-SEM method was successfully applied to both a limestone and a mudrock dataset, and enabled the assessment of the influence of microporosity types on electrical behavior which improves the understanding of the relationship between resistivity and pore structure. This technique is not as computational intensive as 3D methods like micro-CT, yet several 2D sections are still able to give an accurate representation of the 3D pore system (Weger et al., 2009).

Mudrock Nanoporosity

Results from mudrock BIB-SEM analyses suggest that flow properties in mixed carbonate-siliciclastic rocks are governed by their absolute porosity. Higher porosity samples have higher cementation factors. Nanopore geometries generally show little influence on cementation exponents. On the other hand, kerogen (total organic carbon – TOC) and carbonate content (CO₃) show correlation with cementation factors. Higher TOC samples show higher cementation factors. This can be explained by the tendency of kerogen to develop unconnected nano-vugs when maturity increases. Higher carbonate content, on the other hand, results in lower cementation factors in mudrocks. This, however, could also be explained by frequently found lower porosities in samples with higher CO₃ content. High Pyrite content and elevated surface conductivity of the constituent clay minerals keeps cementation factors low in the mudrocks, especially at very low porosities as they retain some matrix conductivity.

Carbonate Microporosity types

Insights into the carbonate micropore structure with the BIB-SEM method suggests that microporosity types have a strong influence on electrical rock properties in carbonates (Norbisrath et al, 2015). Results further demonstrate that microporosity in carbonates often

is of crystalline nature, which would explain their often low electrical resistivity. Crystalline pore networks tend to have higher coordination numbers as compared to non-crystalline rocks, which results in better connectivity and hence also better conductivity (Kharusi, 2008). This would also explain why, at low porosities, carbonate rocks often show lower cementation factors than sandstones. Here, carbonates still retain their well-connected crystalline micropore network whereas sandstones usually show increasingly cemented and obstructed inter-granular flow paths (Abousrafa, 2009). This leads to a decrease in coordination numbers and increase in resistivity in low porosity sandstones. Consequently, the term “cementation factor” is also more suitable for sandstones than for carbonate rocks. Some carbonate rock types, however, contain types of microporosity with poor flow characteristics. Carbonates affiliated with anorganic and bacterial precipitation often have un-connected fenestral micro- or nanopores (Chafetz, 2013), leading to extremely low coordination numbers and high resistivity in these carbonates. Nevertheless, microporosity can always only be partially responsible for the electric rock response in heterogeneous carbonate rocks that contain pores of all size classes. Therefore, micro- and macropore analyses have to be combined, employing results from different analytical methods at different scales.

Multiscale Digital Image Analysis (MsDIA)

MsDIA builds upon the conventional thin-section DIA established by Weger (2006), which is used to quantify macropore geometry. Representative areas which appear solid (non-porous) in thin-section are investigated with high-resolution BIB-SEM analysis (Figure 1.3). Resulting micropore-properties from the investigated subsections are assigned to the entire solid area of the associated thin-section. This simplification has to be

made as the BIB-SEM method is resource-intensive and the amount of sampled area is limited. To capture the multiscale heterogeneity of the carbonate pore space it is especially important to combine thin-section and BIB-section imagery, which enables quantification of pores that span 6 orders of magnitude in size, ranging from nanometer to millimeter scales.

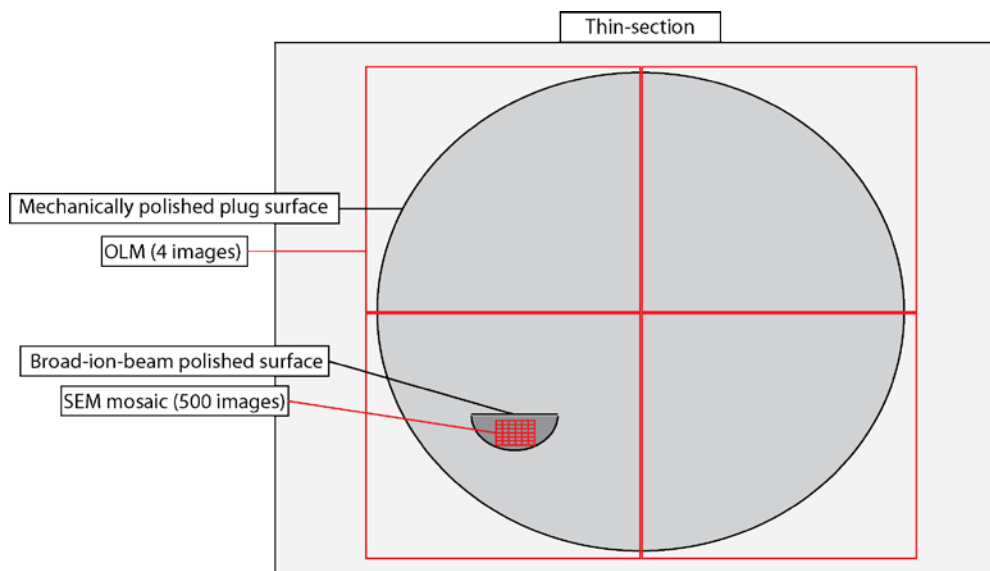


Figure 1.3: Schematic of image acquisition for Multiscale Digital Image Analysis (MsDIA). Combination of four optical light microscope images from mechanically polished thin-sections (DIA sections at micrometer resolution) and several tens or hundreds of scanning electron microscopy images from broad-ion-beam polished surfaces (BIB-SEM mosaics at nanometer resolution).

Electrical Resistivity

The main focus of this dissertation are electrical rock properties and their relation to the pore geometry. Electrical behavior of rocks is an integral tool during formation evaluation from wireline logs, as it is commonly utilized to estimate flow and storage properties along with water saturations using Archie's equations. Electrical resistivity (ρ)

is an intrinsic rock property that specifies how strongly the rock opposes the flow of electric current. For a uniform specimen like a core plug with parallel end sides, resistivity can be defined as:

$$\rho = R \frac{A}{l} \quad \text{Eq. 1.1}$$

With:

R = Resistance (measured in Ω)

A = Cross-sectional area of plug end

l = Length of plug

Mode of Conduction

Carbonate minerals themselves, e.g. calcite, aragonite, dolomite, and also anhydrite, are non-conductive. The normal mode of conduction is electrolytic conductivity, as the pore spaces of natural carbonate rock are more or less filled with saline water in the subsurface (Verwer et al., 2011). Therefore, the conductivity of carbonate rocks is highly dependent on the geometry and connectivity of the brine-filled pore space. In contrast, mudrocks, i.e. mixed carbonate-siliciclastic rocks are often rich in organic material (OM), pyrite, and clay minerals (Lasswell, 2006; Denicol & Jing, 1998). Here, the solid phase of the rock can significantly contribute to conductivity. This can, on the one hand, exacerbate estimates of their water saturation but, on the other hand, enable the use of dielectric logs for estimates of the constituents of the solid phase (Seleznev et al., 2011).

Archie's Equations and Cementation Factor *m*

Archie's empirical formula relates the porosity of a rock to its electrical response. Archie realized that in order to calculate the amount of hydrocarbons in a formation from its resistivity, it is first necessary to recognize the formation resistivity when all pores are filled with connate water ($S_w = 100\%$). The empirically developed relationship between

porosity, electrical resistivity, and the brine saturation of the pore structure is the foundation for modern well-log interpretation and calculation of water and hydrocarbon saturations:

$$FF = \frac{R_f}{R_w} = \Phi^{-m} \quad \text{Eq. 1.2}$$

With:

FF = Formation factor

R_f = Resistivity of formation at 100% water saturation (S_w)

R_w = Resistivity of formation water

Φ = Porosity

m = Cementation factor

The cementation exponent m hereby is the slope of the log-log plot of formation factor vs. porosity and reflects the influence of pore geometry on resistivity. In siliciclastic reservoirs, calculations of water and oil saturation with Archie's (1942) equation can be reliably performed from porosity and resistivity, as cementation and saturation exponents can be assumed to be around $m = n = 2.0$ (or $m = 1.6$ in clean sandstones). Such rocks are referred to as "Archie rocks". In carbonates, on the other hand, relations between resistivity and pore structure are complicated due to heterogeneity and complex pore structures with abundant microporosity. Hence, these exponents vary drastically in carbonate rocks.

Calculations of Water Saturations

Cementation exponents varying between $m = 1.0 - 5.5$ are often observed in carbonate rocks. This variation drastically deviates from the commonly used value of around $m = 2$ (Verwer et al., 2011; Norbistrath et al., 2015). These fluctuations impair predictions of permeability and water saturations from well logs in carbonates when using Archie's equation:

$$S_w = \left[\frac{a}{\Phi^m} \times \frac{R_w}{R_t} \right]^{\frac{1}{n}} \quad \text{Eq. 1.3}$$

With:

a = Tortuosity factor (usually = 1)

Φ = Porosity

m = Cementation factor (varies in carbonates)

n = Saturation exponent (usually = 2)

R_w = Resistivity of formation fluid

R_t = Observed bulk resistivity of formation

It can be argued that rocks with similar pore structures will have a similar cementation factors; hence the type of their porosity can be estimated from their resistivity. High values of m are usually associated with vuggy porosity, and low m -values with microporosity. However, m cannot directly be measured down-hole yet. Thus, if an interval is not identified as being vuggy or microporous, it will lead to underestimation of water saturation in vuggy sections and overestimation of water saturation in microporous sections (Table 1.1). This can result in production of water from seemingly oil-bearing intervals, or failure to recognize prolific hydrocarbon intervals in microporous formations.

Phi (frac)	R_t [Ωm]	R_w [Ωm]	n	m	S_w	Rock type
0.15	400	1.3	2	1.5	24%	Microporous
0.15	400	1.3	2	2	38%	“Archie”-type
0.15	400	1.3	2	3	98%	Vuggy

Table 1.1: Changes in calculated water saturations [S_w] for varying cementation

factors m . S_w values calculated according to Equation 1.3. Using a standard cementation factor of $m = 2$ in a vuggy interval makes it appear to be 62% charged with hydrocarbons ($1-S_w$), although in reality it is 98% water saturated.

Furthermore, permeability is similarly low in both vuggy and microporous intervals, yet they have opposing cementation factors. This leads to ambiguity in permeability predictions from resistivity logs, but can possibly be overcome by combination with velocity deviation logs (Anselmetti and Eberli, 1998). In theory, fast rocks with low cementation factors (no vugs) and slow rocks with high cementation factors (no microporosity) should have high permeability. Thus, accurate estimates of cementation exponents could also provide a quantitative measure to identify porosity that does not contribute to fluid flow (vugs and micropores) and significantly improve permeability predictions.

Complex Electrical Resistivity

Cementation factors are calculated from the amplitude change between induced and measured absolute resistivity values. However, electrical resistivity in a brine-saturated porous medium is a complex entity, as dielectric effects of the pore fluid and the fluid-rock interface cause phase shifts between induced and measured signal. The phase shift is the imaginary part of complex resistivity, and the change in amplitude is the real part. These can be referred to in terms of complex impedance Z , where R is the resistance (real part) and iX is the reactance (imaginary part) (Knight and Nur, 1987):

$$Z = R + iX \qquad \text{Eq. 1.4}$$

All resistivity measurements for this dissertation are performed in a true 4-electrode setup in log sweeps from 0.1 – 100,000 Hz on fully 35 ppt NaCl brine saturated core plugs. This allows not only for calculations of cementation factors from resistivity attenuation at 720 Hz, but also for analysis of the dispersive behavior of complex resistivity at different

frequencies, which can be attributed to pore structural properties of the rock. Various authors have found correlations between the low-frequency phase shifts of complex resistivity and permeability in siliciclastic rocks (Weller & Börner, 1996; Denicol & Jing, 1998; Cerepi, 2004; Tong & Tao, 2008). More recently there have been major advances in the use of high-frequency dielectric tools for formation evaluation (Seleznev, 2005; Weller et al., 2010; Zisser et al., 2010; Wang & Poppit, 2013). Above reasons gave incentive to study low-frequency dielectric rock properties and ultimately lead to the second major goal of this dissertation, to utilize complex resistivity spectra (CRS) for estimates of petrophysical rock properties on core plugs.

Complex Resistivity Spectra (CRS)

Analyses of kHz-range complex resistivity spectra (CRS) help to illuminate the interrelation of dielectric dispersion, specific surface area, and other pore geometrical and petrophysical properties. The fundamental idea is that low-frequency dielectric dispersion is related to interfacial polarization effects that depend on the amount of specific surface area of the rock, which is a pore-structure characteristic known to also influence permeability and cementation factors. Consequently, one can use CRS measurements to estimate permeability and cementation factors. This hypothesis is tested in this dissertation by quantification of the dielectric dispersion in the 0.1 – 100,000 Hz range as input for a model to predict several rock properties. Results show that CRS can be used to accurately predict permeability and cementation factors in both carbonates and mudrocks.

The ultimate goal is to establish fundamental petrophysical relationships that could motivate the development of a CRS wireline tool by a wireline company. Such CRS tool

could be used to almost independently estimate permeability and cementation factors down-hole, which would be of high commercial interest in heterogeneous carbonates.

Working Hypotheses

This dissertation employs three main hypotheses:

- 1) Carbonate microporosity is essential for electrical flow properties.
- 2) Low-frequency dielectric dispersion can be used to estimate reservoir properties.
- 3) Carbonate pore size distributions follow a fractal pattern.

These hypotheses are tested in four separate yet adjoined studies that each address a certain dataset or topic but also partially complement each other when they are applied to a different rock type. The specific goals and approaches to reach them are listed below for each chapter:

Chapter 2

Goals:

- Find a method to quantify microporosity.
- Evaluate carbonate micropore geometry in terms of electrical flow properties.
- Assess pore size distributions and analyze for fractal patterns.

Approach:

- Measure cementation exponents on a variety of carbonate core plugs.
- Reach out to other institutions that have BIB-SEM capabilities for a collaboration.
- Utilize broad-ion-beam milling (BIB) to achieve nanometer-precision flat surfaces and acquire SEM mosaics that are large enough to be representative for micropore structure at high resolution.

- Combine BIB-SEM method with thin-section DIA for Multiscale Digital Image Analysis (MsDIA).
- Find pore geometric parameters that control electrical flow.
- Qualitatively analyze the pore structure and group into micropore types according to flow properties.
- Use double-logarithmic plots with increasing bin sizes to find natural fractal patterns in pore size distributions.
- Use MICP methods to assess the pore throats and evaluate their importance for electrical and fluid flow properties.

Chapter 3

Goals:

- Test method from Tong & Tao (2008) that utilizes CRS to estimate permeability on a heterogeneous dolomite dataset.
- Test influence of dolomite crystal size on electrical properties.
- Assess influence of pressure (overburden) on cementation factors.

Approach:

- Gather data from Shen (2008) and measure cementation exponents on recoverable plugs.
- Reach out to NER to get code for extraction of raw measurement data in order to analyze CRS data.
- Measure and plot CRS curves to find controls of CRS on petrophysical properties and vice versa.

- Find frequency range that correlates best with permeability. Quantify identified CRS frequency range by fitting curves in frequency range of interest.
- Use CRS information as input for model to predict permeability and evaluate which parameters or aspects of the frequency dispersion show best correlation coefficients between input and predicted parameters (highest correlation coefficients).
- Compare crystal size data to permeability and cementation factors.
- Find trends for pressure dependency and hysteresis of cementation factors in dolomite rocks.
- Use double-logarithmic plots with increasing bin sizes to find natural fractal patterns in pore size distributions.

Chapter 4

Goals:

- Apply CRS method from chapter 3 on a heterogeneous carbonate dataset, in order to find fundamental relationships and universal parameters that can aid to predict permeability and cementation factors in carbonate reservoirs.
- Evaluate the feasibility of a CRS wireline tool.
- Test if fractal power-law behavior persists in all carbonate rock types.

Approach:

- Locate useable data (pore geometry from DIA, permeability, cementation factors) from previous studies.
- Apply CRS method to each of 12 individual datasets. Find common frequency range that best describes flow properties (highest correlation coefficients).

- Use double-logarithmic plots with increasing bin sizes to find natural fractal patterns in pore size distributions.

Chapter 5

Goals:

- Utilize BIB-SEM method from chapter 2 to quantify mudrock nanoporosity and assess influence on electrical properties.
- Apply CRS method from chapter 3 on a mixed carbonate-siliciclastic dataset.
- Test CRS method for predictions of mineralogy.
- Qualitatively compare mudrock to carbonate nanoporosity.
- Evaluate pressure dependency of cementation factors

Approach:

- Measure CRS on mudrock samples.
- Acquire 10 by 5 SEM image mosaics at same magnification as in chapter 2 and quantify nanopore geometries.
- Apply CRS method to mudrock dataset to predict cementation factors, but also evaluate if correlation to mineralogical parameters exists (TOC, CO₃ content).
- Plot and find trends for pressure dependency and hysteresis of cementation factors in mudrocks.

Chapter 2: Electrical and Fluid Flow Properties of Carbonate Microporosity Types from Multiscale Digital Image Analysis and Mercury Injection

Summary

Electrical and fluid flow properties of porous media are directly related to the morphology of pores and the connectivity of the pore network. Both are closely linked to the amount and type of intrinsic microporosity in carbonate rocks, which is not resolved by conventional techniques. Broad-ion-beam (BIB) milling produces high-quality true-two-dimensional cross sections for scanning electron microscopy (SEM) and enables accurate quantification of carbonate microporosity for the first time. The combination of BIB-SEM mosaics with optical micrographs yields a multiscale digital image analysis (MsDIA) spanning six orders of magnitude. In this paper, the pore structures of 12 different carbonate rock samples from various rock types are quantified using MsDIA. Mercury injection capillary pressure measurements are used to assess pore-throat properties. The quantified pore-structure parameters are correlated with plug measurements of electrical resistivity and permeability.

Results indicate that petrophysical properties are closely linked to the type of microporosity, which is distinctive for a certain rock type. Rock types with crystalline microporosity, such as mudstone and dolomite, generally show good connectivity, in which the size of the pore-network determines if the rock favors either hydraulic or electric flow. Rock types with intercement or micromoldic microporosity, such as bindstone and travertine, show variations in connectivity due to layering and moldic micro-pores of biological origin. Furthermore, pore-size distributions (PSD) follow a power law in all samples, despite their depositional and diagenetic differences. The slope of the PSD

correlates with the electric properties, in which samples with a steeper slope show lower cementation factors. The linearity of the power law distribution enables predictions of pore populations outside the investigated length scales.

Introductory Remarks

Carbonate rocks often have very heterogeneous pore structures with large variations in pore size and abundant microporosity (Anselmetti et al., 1998; Arns et al., 2005; Sok et al., 2010; Curtis et al., 2012). Describing this heterogeneity requires a multiscale approach, and imaging the microporosity requires a high-resolution technique. This is particularly important when trying to understand electrical flow properties because they are heavily influenced by increased pore density and connectivity of microporous regions (Sen et al., 1997; Cerepi et al., 2002; Wang et al., 2005; Verwer et al., 2011; Garing et al., 2014). Broad-ion-beam (BIB) milling coupled with scanning electron microscope (SEM) imaging has recently been introduced to determine pore structures of manufactured materials (Smith et al., 2009) and fine-grained rock samples (Desbois et al., 2009). The BIB-SEM technique has since been applied to shale and tight sandstone reservoir rocks, where it has brought about major improvements in imaging of nanoporosity (Curtis et al., 2010; Ambrose, 2011; Desbois et al., 2011; Hemes et al., 2013; Klaver et al., 2012; Houben et al., 2013, 2014). The ion-milling technique is now used to investigate microporosity types and geometries in carbonate rocks, attempting to understand their controls on electrical flow properties.

This paper takes a multiscale imaging approach, combining conventional thin-section microscopy with BIB-SEM image mosaic acquisition. The result is a pore-structural investigation from plug to nanopore scale (Figure 2.1). The high resolution of the BIB-SEM method enables accurate quantification of the two-dimensional (2-D) micropore

structure (Desbois et al., 2011; Hemes et al., 2013; Klaver et al., 2012; Houben et al., 2013, 2014).

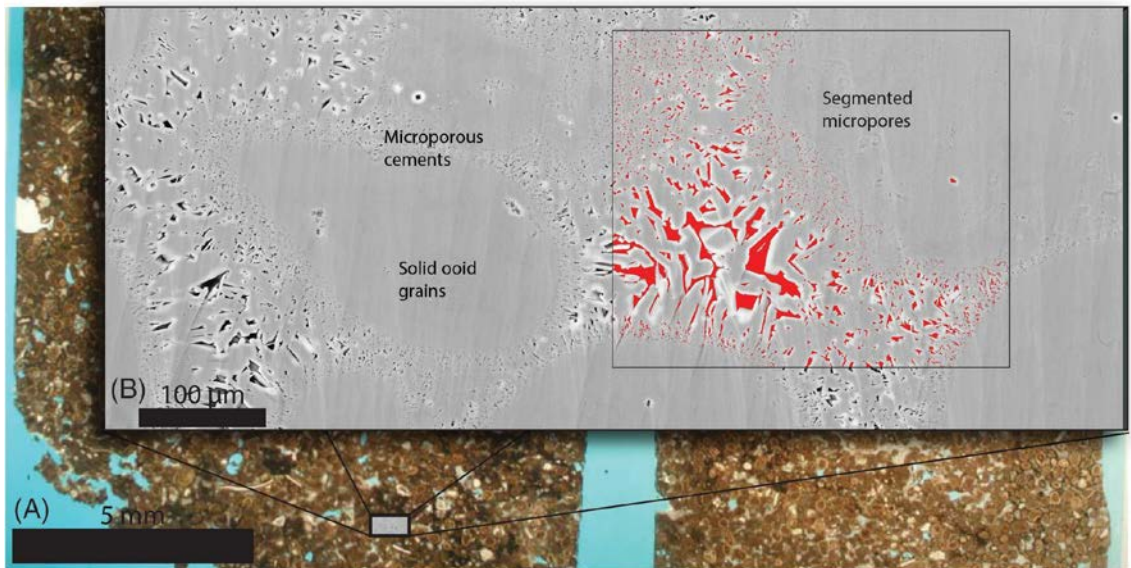


Figure 2.1: Zoom into the pore structure of stromatolitic ooid bindstone. Combination of (A) thin-section image and (B) scanning electron microscope mosaic acquired on broad-ion-beam polished surface illustrates the variability of pore structure and pore sizes at different magnifications. Box overlay shows segmented micropores in red. These serve, together with segmented macropores from blue-dyed thin sections, as input for multiscale digital image analysis.

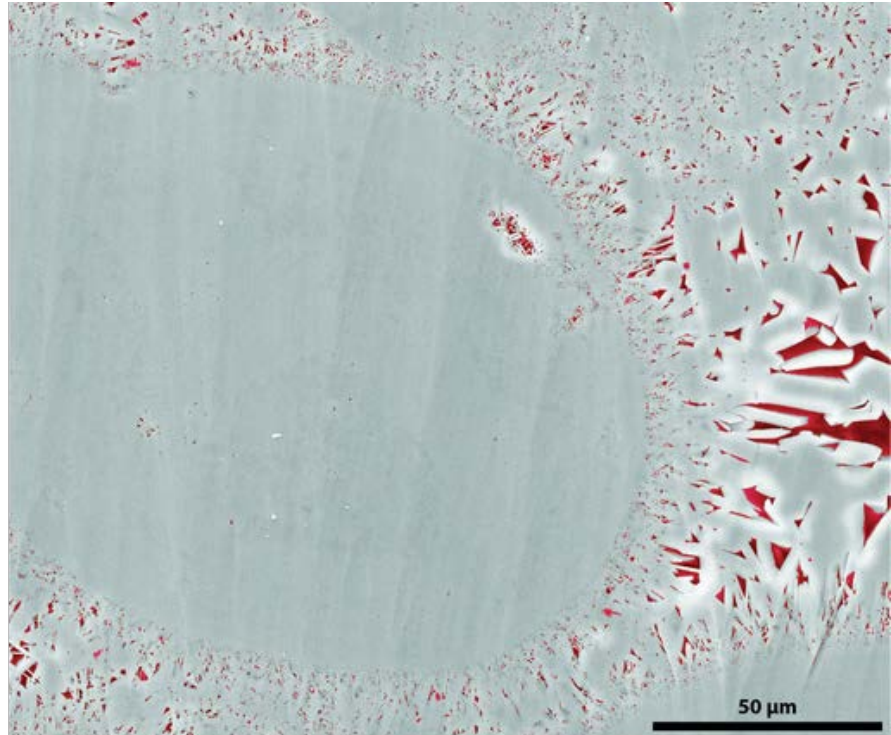
The goal of this study is to find and quantify the 2-D pore-geometric parameters that are most influential for the conduction of electrical charge in order to improve interpretations of resistivity logs in carbonates. Log interpretations and reservoir calculations are based on Archie's (1952) empirical formula:

$$F = \frac{R_f}{R_w} = \Phi^{-m} \quad \text{Eq. 2.1}$$

where F (formation factor) relates the ratio of resistivity of the formation (R_f) to the resistivity of the pore fluids (R_w) the porosity (Φ), and the exponent m . Archie (1952) postulated that the exponent m is related to the degree of consolidation or cementation of the rock. Calculations of water saturation work well in clean sandstones with simple pore

structures because their cementation exponent m is generally approximately 2. In carbonates, however, the cementation factor m is known to fluctuate due to the large variety of textures and pore sizes (e.g., Folk, 1959; Dunham, 1962) and pore types (e.g., Choquette and Pray, 1970; Lucia, 1995; Ahr et al., 2005; Lønøy, 2006). In particular, microporosity complicates correlations of resistivity to pore structure. On the one hand, brine-saturated micropores in an oil reservoir promote electrical flow but prevent effective fluid flow. This can lead to an overestimation of permeability. On the other hand, micropores often remain brine saturated after the formation has been charged with hydrocarbons. This can lead to an overestimation of water saturation, masking possible pay zones with easily producible hydrocarbons stored in the macropores (Sen et al., 1997). The focus of this study, therefore, lies on the analysis and quantification of the microporosity. Bulk methods such as nuclear magnetic resonance and mercury injection capillary pressure (MICP) can only indirectly quantify micropores. Direct three-dimensional (3-D) methods such as micro-CT or focused ion beam (FIB) SEM (FIB-SEM) lack either resolution or analyzed volume to be representative for the pore structure of heterogeneous carbonates. Recently, direct 2-D quantification of micro- and nanopores with the SEM was impeded by excessive surface roughness from conventional mechanical polishing methods (Anselmetti et al., 1998). The BIB cross sectioning now produces large, flat, damage-free surfaces, which are suited for quantification of nanometer-scale pores (Figure 2.2).

Figure 2.2:
Stromatolitic
oid bindstone
with segmented
microporosity in
red. *Bladed,*
isopachous
cements around
oid grains form
well-connected
intercement
microporosity



Data Set

A total of 12 carbonate core plug samples are chosen from contrasting depositional and diagenetic environments to capture the range in microstructures of different carbonate rock types. The data set consists of the following rock types: oolitic bindstone (Holocene stromatolite, Bahamas), wackestone (Lower Cretaceous Quintuco Formation, Argentina), packstone (Carboniferous, Kazakhstan), travertine (Italy), tufa (United States lakes), reefal packstone (Pleistocene–Pliocene, Dominican Republic), and crystalline dolomite rocks (Mississippian Madison Formation, United States) (Table 2.1). Porosity ranges from 3% to 27% and permeability from 0.01 to 320 md. Cementation factors range from $m = 1.6$ to 3.4.

Methods

Porosity, Permeability Measurements

Porosity was measured with a Micromeritics AccuPyc 1330 Helium pycnometer using Boyle's law, that is by determining the difference between caliper volume of the plug and its grain volume. Standard gas permeability measurements were performed by Terratek.

Electrical Resistivity

Laboratory electrical resistivity measurements on brine-saturated core plugs are performed in a four-electrode setup. Full brine saturation is achieved by submerging the core plugs in 35 g/L (1.2 oz/gal) NaCl brine (35,000 ppm NaCl; conductivity: 53–56 mS) and repeatedly pulling vacuum over the submerged plugs during a 24–48-hr period. Saturated samples are fit into rubber jacketing and mounted between the core holders, which house the electrodes and pore-pressure system. The voltage contacts on the core holders are recessed and isolated with polyester felt from the conductive porous silver membrane filters that cover the current electrodes. This setup avoids erroneous contact resistivity and minimizes electrode impedance, which can cause measurement bias. The pore-pressure lines are made of nonconductive plastic to electrically isolate the measurement setup from the rest of the apparatus. The complete core holder setup with the plug sample is placed into the oil-filled pressure vessel and locked into place with cloverleaf closures. At varying pressure steps, measurements of complex resistivity are taken in a log sweep from 0.1 to 100,000 Hz. Reported cementation factors are calculated from temperature-corrected resistivity amplitude values at 10 MPa (1450 psi) effective pressure for a frequency of 720 Hz (Arps, 1953).

Broad-Ion-Beam Milling with Subsequent Scanning Electron Microscopy Image

Mosaic Acquisition

The BIB-milling step is essential for the quantification of nanometer-scale pores because accurate pore segmentation requires surfaces to be smooth at the scale of investigation. Conventional mechanical polishing induces surface damage, leaves behind milling residue, and generally produces surfaces with high topography when viewed at high magnifications, rendering porosity segmentation impossible. BIB-milling removes this surface damage and sections the rock sample in a true 2-D plane with typical remaining topography in the range of ± 5 nm (Klaver et al., 2012). In our samples, artifacts induced by BIB-milling are generally minor. Slight curtaining artifacts are induced by the inside walls of larger pores being more exposed to the ion beam, causing it to mill deeper into the surface. The curtaining grooves are identified and filtered out during segmentation. Edge and low-angle topography effects require slight manual cleaning of the BIB-SEM mosaics (Hemes et al., 2013). Redeposition of milled material inside pores is not observed in our samples.

The BIB milling with argon ions has the advantage of producing smoother and much larger surfaces than FIB techniques, where high-energy gallium ions are used. The FIB volume dimensions are typically only about $10 \times 10 \times 10 \mu\text{m}^3$. The comparatively large BIB surfaces (up to 2 mm^2) are more suitable for the quantitative study of microporosity because, in combination with thin-section imagery, the investigated areas are large enough to be representative for petrophysical core plug measurements. Recent improvements in milling technique might even enable polishing of entire 1 inch plug surfaces, which would further improve the possibilities for multiscale image analyses.

The areas for investigation with the new technique are selected from 3200-dpi flatbed scans of core-plug surfaces. To focus on microporosity and avoid overlap in pore sizes, areas with the least amount of visible macropores are chosen. Subsamples ($0.5 \times 0.5 \times 0.5$ mm³) containing the target areas are cut dry with a hand-held saw blade. The subsamples are mounted on stubs and prepolished to approximately ± 10 μ m roughness using silicon carbide paper. The samples are then placed in the BIB; milling time is approximately 7.5 hours at 6 kV and 150 μ A. The cross sections are prepared in the same plane as the accompanying optical thin section. Polished surfaces are then sputtered with gold to prevent surface charging during SEM imaging. The sample surface structure is imaged with the secondary electron detector (SE2). The secondary electrons have a shallow interaction volume well suited to focus on the 2-D quantification of the pores, especially at low accelerating voltages. Automated acquisition of image grids containing hundreds of images streamlines investigation of large areas. Grids are acquired at 5000 \times and 15,000 \times magnifications with 20%–30% overlap. Stitching of the image grids into coherent mosaics is done with a bicubic interpolation algorithm, preserving the pixel resolution (Klaver et al., 2012) using Autopano software. Pores are detected based on pixel gray-scale values in secondary electron images. The porosity is segmented with a combination of thresholding and sobel-edge-detection algorithms (Houben et al., 2013). Thresholds are chosen on a subset and then applied to the entire mosaic. The shallow depth of field of the secondary electron images combined with the nanometer-precision flat surfaces allows for very accurate differentiation between pore and solid (Figure 2.2). The resulting binarized mosaics are manually inspected and cleaned from remaining artifacts with standard image processing software (Hemes et al., 2013).

Multiscale Digital Image Analysis

Multiscale digital image analysis (MsDIA) combines thin-section image analysis with the analysis of BIB-SEM mosaics to extract geometric parameters of pores across six orders of magnitude. Pore sizes identified from thin-section images range from plug-scale (several mm) down to the thickness of the thin section (approximately 30 μm). Pores in BIB-sections range from approximately 200 μm down to the practical resolution (Klaver et al., 2012) of 19.5 nm at 30,000 \times magnification. The overlap from 200 to 30 μm ensures a continuous analysis of the pore space, with the thin-section analysis covering the macropores and the BIB-section analysis covering the micropores.

The outcome of the MsDIA is quantified pore-geometric parameters that can be related to the measured petrophysical flow properties of the sample in order to identify controlling factors. The main purpose is to advance the understanding of how the internal geometry of microporosity affects electrical resistivity and permeability. Correlation of petrophysical with quantified pore-space parameters from digital image analysis (DIA) has the advantage of not relying on qualitative interpretations of pore types or texture; hence, it is well suited to compare larger data sets or to define attributes of certain rock or pore types.

The macropore structure is analyzed using DIA on blue epoxy-impregnated thin-sections imaged with optical light microscopes using the methodology of Weger et al. (2009), where four or more thin-section images are stitched, segmented, and quantified with ImageJ in an automated MATLAB environment. The micropore structure assessed with the binarized BIB-SEM mosaics is also parameterized with ImageJ. The amount of micropores observed at the high resolution is then scaled up to thin-section dimensions by multiplying the micropores with a scaling factor depending on the size ratio of the BIB-

SEM mosaic compared to the thin section. This can be seen as “populating” solid areas on thin sections with pores identified on BIB-SEM mosaics at a higher resolution. The scaling factors are calculated for each sample as follows:

$$\text{Scaling factor} = \frac{\text{Area}_{\text{TS}}(1 - \text{Porosity}_{\text{TS}})}{\text{Area}_{\text{BIB}}} \quad \text{Eq. 2.2}$$

where Area_{TS} is the analyzed thin-section area, $\text{Porosity}_{\text{TS}}$ is the area identified as porosity on the thin section, and Area_{BIB} is the area analyzed with BIB-SEM. This generalization has to be made due to constraints on the amount of area that can be analyzed with BIB-SEM. However, care has been taken to select areas for BIB-SEM analysis that are representative of the heterogeneous microstructure, both from flatbed scans and subsequently SEM overview images.

Dominant Pore Size

Dominant pore size (DOMsize) is the upper boundary of pore sizes making up 50% of the porosity on a thin-section (Weger et al., 2009). The parameter describes the size of the pores of the sample with a single characteristic value and gives a good indication of the effective size of a pore network. To calculate DOMsize, pores from thin-section and BIB-section analysis are combined in a cumulative curve by sequential summation of pore areas of increasing size. The pore size on the cumulative curve at 50% is the DOMsize. Pore sizes are measured in area (amount of pixels) and converted to size-equivalent diameter (d_{eq}). Equivalent diameter is the diameter of a circle with the same areal extent as the identified pore:

$$d_{\text{eq}} = 2 \sqrt{\frac{A}{\pi}} \quad \text{Eq. 2.3}$$

Perimeter over Area

Perimeter over area (PoA) is the ratio of the sum of the perimeter of all pores identified on a cross section and the sum of the area of these pores. It can be understood as a 2-D equivalent to specific surface that is defined as the ratio between pore volume and pore surface (Weger et al., 2009). To avoid bias in this shape parameter analysis, pores close in size to the limits of resolution are omitted (Weger, 2006). Hence, only pores that are composed of at least 100 pixels are incorporated. The PoA is calculated separately for each of the three acquired mosaics (TS = thin section; BIB5K and BIB15K = BIB-SEM mosaics at 5000× and 15,000× magnification, respectively) and then averaged for each plug:

$$PoA = \frac{1}{3} \left(\frac{\sum Perimeter_{TS}}{\sum Area_{TS}} + \frac{\sum Perimeter_{BIB5K}}{\sum Area_{BIB5K}} + \frac{\sum Perimeter_{BIB15K}}{\sum Area_{BIB15K}} \right) \quad \text{Eq. 2.4}$$

The parameter describes the complexity of the pore structure. It is independent of the total amount of porosity but dependent on the size of the pores: A smaller pore will have a higher PoA value than a larger pore with the same shape.

Normalized Pore Density

Normalized pore density (Pdnorm) is the combined amount of pores per area, which are identified at different magnifications (TS, BIB5K, and BIB15K), normalized by the total analyzed area (AreaTS) and plug porosity (Phi):

$$Pd_{norm} = \frac{Pores_{TS} + Pores_{BIB5K} + Pores_{BIB15K}}{Area_{TS}(\text{Phi} [\%])} \quad \text{Eq. 2.5}$$

Duplicate results from overlapping pore size classes from the different image magnifications are omitted by using pore size cutoffs selected based on the most reliable detection method for that size class. The PoresTS include only pores larger than 100 μm,

PoresBIB5K all pores between 100 and 1 μm , and PoresBIB15K the smallest pores below 1 μm .

Pore Body-to-Throat Ratio

The pore body-to-throat ratio (BTR) is estimated by relating pore-body sizes extracted from the 2-D imagery to pore-throat sizes from MICP measurements. The BTR (sometimes referred to as aspect ratio) is interpreted to correlate well with the effectiveness of electrical flow in porous media (Jackson et al., 1993). It is the ratio of the DOMsize and critical pore-throat size (D_c):

$$\text{BTR} = \frac{\text{DOMsize}}{D_c} \quad \text{Eq. 2.6}$$

A large BTR value indicates that pore throats are small compared to the pore body, and a small BTR value implies that the throats are comparatively large.

Pore-Size Distribution and Fractal Dimension D

Pore-size distributions (PSDs) are analyzed by distributing all pores identified on the individual mosaics into nonlinear bins (always doubling bin width) according to their pore size (pore area). Pore-size frequencies are then normalized by total area (area of thin-section image) and bin width (pore-size range), and results plotted against bin centers (pore size) on a double logarithmic scale (Hemes et al., 2013; Klaver et al., 2012; Houben et al., 2013, 2014). This process is done for each of the three acquired mosaics of a sample (TS, BIB5K, and BIB15K). The smallest bin centers (pore sizes) of the individual BIB-SEM mosaics are omitted because they are close to the resolution limit where pore segmentation becomes problematic due to edge and low-angle topography effects resulting in undetected pores (Hemes et al., 2013). This means that pores below 256 and 64 nm equivalent side length are omitted in the 5000 \times and 15,000 \times mosaics, respectively.

Least-squares linear regression analysis is used to quantify the slope (power law exponent) of the PSDs of all recognized pores:

$$D = -\frac{\log\left(\frac{\text{Pore size frequency}}{\text{Total area} * \text{Bin width}}\right)}{\log(\text{Pore size})} \quad \text{Eq. 2.7}$$

The absolute value or inverse of the slopes ($D = -\text{slope}$) thereby represents the fractal dimension D of the pore space (Mandelbrot, 1967).

Mercury Injection Capillary Pressure: Critical Pore-Throat Diameter

Mercury injection porosimetry is used to assess the pore network and pore throats. A variety of methods can be used to represent the pore-throat size distribution in a sample (Nelson, 2009). The D_c describes the pore throats and characterizes the connected pore space of a bulk sample with a single parameter. The D_c is the throat diameter at critical pressure when mercury first spans the sample and percolation begins (Katz and Thompson, 1987). Pressures up to 413 MPa (60,000 psi) are applied to force mercury into pore throats down to 3-nm diameter. The pressure (P) is converted to pore-throat diameter (D) with Washburn's equation (Washburn, 1921), assuming a tube model for the pore structure:

$$D = -4\gamma\cos\frac{\theta}{P} \quad \text{Eq. 2.8}$$

where the contact angle θ is 130° and the surface tension $\gamma = 485$ dynes/cm. D_c is calculated from the injection pressure at the inflection point in the rapidly rising range of the cumulative intrusion curve (Swanson, 1985; Urai et al., 2008). The inflection point is derived from a third-order polynomial model fitted to the curve.

Results

BIB-SEM Mosaics

From each of the 12 samples, two high-resolution BIB-SEM image mosaics are acquired; one overview at 5000× magnification and a zoom into the overview area at 15,000× magnification (58.6 and 19.5 nm pixel side length, respectively). The mosaics each consist of 250 to 550 SEM images with up to 0.23 gigapixels in total. The high-resolution mosaics reveal the diverse submicron pore structures of the different carbonate rock types (Figure 2.3), which can be classified into distinctive types of microporosity according to their geometry and flow properties.

Types of Microporosity

We distinguish four types of microporosity in our samples: (1) small intercrystalline, (2) large inter- crystalline, (3) intercement, and (4) micromoldic. Type I microporosity occurs in wackestones, pack- stones, and tufa; type II in dolomites; type III in the ooid bindstone; and type IV in travertines (Table 2.1). The flow properties of the rock are strongly influenced by the type of microporosity. For example, all rocks with type I microporosity show low permeabilities and low to intermediate cementation factors. Samples with type II micro- porosity have intermediate cementation factors and high permeability. Samples with type III or IV microporosity have high cementation factors and high permeability (Table 2.1).

Rock Type	Sample ID	Microporosity Type	m	Permeability (md)	Φ (%)	Pd_{norm}	DOMsize (μm)	D_c (μm)	BTR	PoA (mm^2)	D
Packstone	523	1 small intercrystalline	1.6	0.01	3.0	24,646	1.9	0.18	11.0	5147.5	2.15
Wackestone	49b	1 small intercrystalline	1.7	0.09	15.9	11,531	0.8	0.38	2.1	5896.3	2.08
Packstone	431	1 small intercrystalline	1.7	0.04	3.6	16,147	3.4	0.18	18.9	4108.3	2.00
Travertine	ST12B	4 micromoldic	1.9	55.10	3.0	33,905	42.8	0.04	1216.6	1603.2	1.90
Packstone	1221	1 small intercrystalline	2.1	0.98	7.3	6625	3.9	2.1	1.8	2719.0	1.99
Dolomite	WR75.9	2 large intercrystalline	2.1	195.20	26.8	1410	9.9	7.2	1.4	925.7	1.76
Packstone	BC2V49	1 small intercrystalline	2.1	1.11	23.5	4637	7.9	0.88	9.1	2400.6	1.86
Packstone	1385	1 small intercrystalline	2.1	0.03	3.6	12,687	1.2	0.17	7.4	4058.3	2.18
Dolomite	WR56.15	2 large intercrystalline	2.2	319.25	16.8	1267	26.4	5.9	4.4	474.8	1.67
Tufa	GCY1	1 small intercrystalline	2.2	0.26	14.6	18,483	1.1	0.15	7.6	6036.3	2.00
Bindstone	22	3 intercement	2.6	267.73	16.2	7674	57.8	113.2	0.5	1138.1	1.82
Travertine	ST36A	4 micromoldic	3.4	79.10	14.0	6405	90.6	158.4	0.6	911.7	1.84

Table 2.1: Qualitative and Quantitative Petrophysical and Pore-Structural Parameters of 12 Analyzed Carbonate Plug Samples, in Order of Ascending Cementation Factor m . * Pd_{norm} = normalized pore density; DOMsize = dominant pore size; D_c = critical pore-throat diameter; BTR = body-to-throat ratio; PoA = perimeter over area; D = slope of pore power-law pore size distribution.

Microstructure in the Various Samples

The Lower Cretaceous wackestone (sample 49b) is almost entirely composed of a matrix of homogeneous crystalline microspar, which is either a diagenetic product of recrystallized micrite (Loucks et al., 2013; Lucia and Loucks, 2013) or a primary cement (Melim et al., 2002). The microspar crystals measure between 1 and 4 μm in diameter and partially show edge roundness and anhedral crystal faces. The wackestone contains only a few dispersed shell fragments with intraclastic or vuggy pores where they are completely dissolved. The small microspar crystals form a very well-connected pore network with low tortuosity and high pore density (type I microporosity).

The packstones (samples 523, 431, 1221, BC2V49, 1385) have similar well-connected and low-tortuous matrix microporosity as the wackestones (type I small intercrystalline microporosity). Microspar crystals are slightly larger at 2–8 μm in diameter. They contain more grains than the wackestones but the grains are heavily micritized and often entirely recrystallized to microspar. In the samples with low porosity, the microspar fabric often is

not visible due to extremely tight packing. These tight packstones also show microfractures. The dolomites (WR75.9, WR56.15) are characterized by a wide and angular intercrystalline micro- pore network (type II large intercrystalline microporosity). It is similar in structure to the type I microporosity, but at a larger scale, as the dolomite rhombs are ten to hundredfold larger than the microspar crystals. The dolomite rhombs measure between 10 and 150 μm across, which also result in larger pores and lower pore densities, increasing tortuosity.

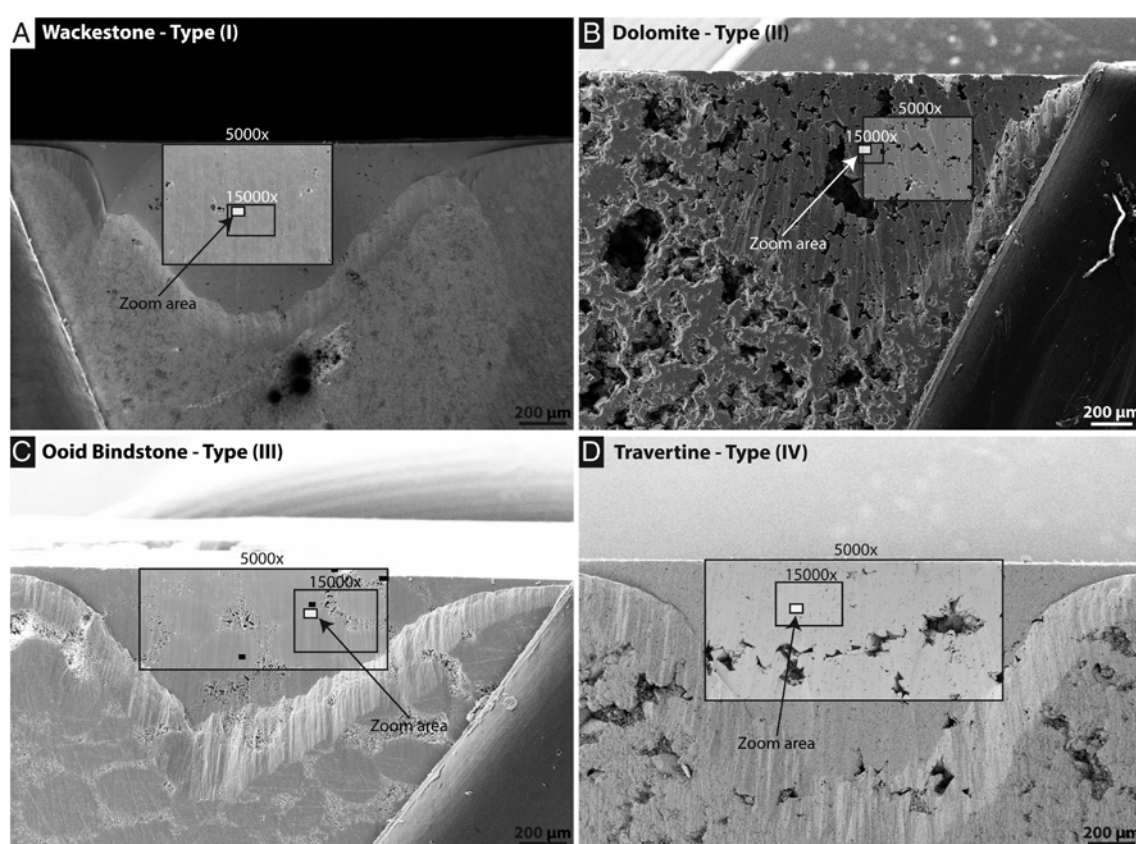


Figure 2.3: Overviews of the broad ion beam (BIB) cross-sectioned areas in four carbonate rock types with distinct types of microporosity, showing their different macropore structures. Areas of BIB-SEM (scanning electron microscopy) mosaics for micropore investigations (5000 \times and 15,000 \times magnification) shown as overlays. (A) Wackestone: dense matrix with few visible pores. (B) Dolomite: large and angular pores. (C) Ooid Bindstone: round and dense ooids bound by microporous cements. (D) Travertine: large and vuggy pores, partially following a horizontal trend. Curtaining artifacts from ion-milling below larger pores (radial, near-vertical surface grooves) visible in the dolomite sample (B). Arrows indicating zoom areas shown in Figure 2.4.

The ooid bindstone (sample 22) has a well-connected micropore network between isopachous, bladed, and fibrous cement around the ooid grains (type III intercement microporosity). This micropore network is well connected, but tortuosity is increased by the dense ooid grains blocking direct flow pathways and relatively low pore density. The ooids contain only a few patches of nanoporosity, which appear largely unconnected. The lack of microporosity inside the ooid grains is somewhat surprising but is due to the young Holocene age, which means that the ooids have never been exposed to freshwater and thus only experienced early marine diagenesis.

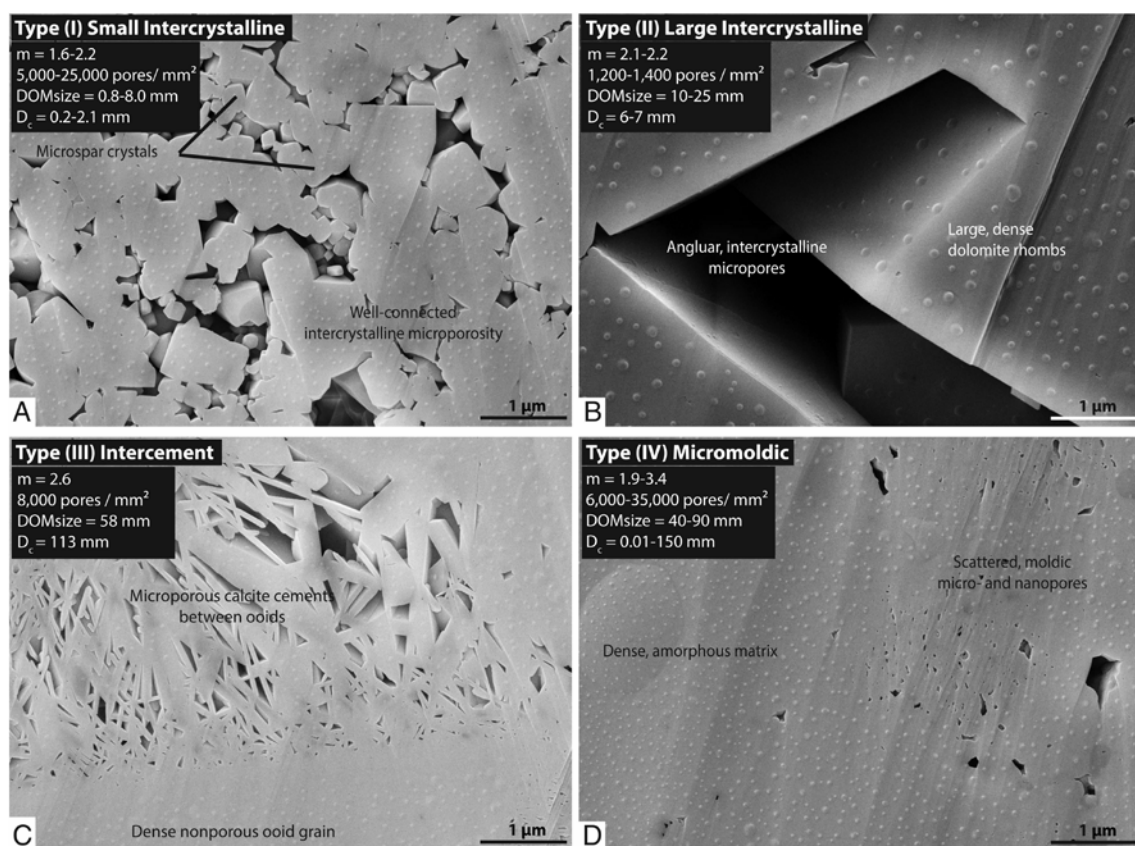


Figure 2.4: Four types of microporosity at 15,000 \times magnification from broad-ion-beam milling coupled with scanning electron microscope (BIB-SEM) mosaics, showing their distinct microstructures at nanometer scales. (A) Type I small intercrystalline (wackestone): well-connected intercrystalline micropore network between microspar crystals (<1 μm). (B) Type II large intercrystalline (dolomite): comparatively large, angular micropores, forming well-connected intercrystalline pore network between dolomite rhombs (~ 100 μm) at scales above this magnification. (C)

Type III intercement (oid bindstone): well-connected micropore network between bladed to fibrous calcite cements around dense oid grains. (D) Type IV micromoldic (travertine): unconnected and scattered fenestral micropores and nanopores in dense matrix. Images annotated with sample cementation factors, pore density, dominant pore size, and critical pore-throat diameter. Note near-vertical curtaining artifacts below larger pores. m = sample cementation factor; $DOMsize$ = dominant pore size; D_c = critical pore-throat diameter.

The travertines (samples ST12B and ST36A) have mostly scattered and moldic micropores (type IV microporosity). In these travertines, dense areas without visible porosity, even at the highest magnification, surround and isolate porous patches. The pores within the porous patches also are unconnected in 2-D. Most pores are fenestral-shaped microvugs, likely associated with the biological origin of the rock (Chafetz, 2013).

The tufa (GCY1) is a meteogene travertine formed from ambient temperature lake water as opposed to the thermogene travertines (ST12B, ST36A) formed in hot springs. The micropore structure, however, is very different from the thermogene travertine. The tufa sample has a crystalline matrix microporosity that is similar to the pack-stones and wackestones (type I microporosity). It is partially dolomitized around the macropores, with type II microporosity between the larger dolomite rhombs.

Multiscale Digital Image Analysis: Quantified Pore Geometric Parameters

The output of the MsDIA consists of a range of statistical and geometrical parameters of pores ranging from around 20 nm up to 20 mm in size (Table 2.1). The most important parameters for this study are the $DOMsize$, PoA , $Pdnorm$, and characteristics of the PSD (fractal dimension D).

The $DOMsize$ s range from 0.8 to 90.6 μm in the samples. Samples with smaller $DOMsize$ show lower electrical resistivity, but also lower permeability (Figure 2.5A). The travertines show the largest $DOMsize$ in the data set but not the highest permeability

because they contain unconnected type IV micro- porosity of microbial origin. The dolomites and ooid bindstone with types II or III microporosity also have large DOM sizes, but a higher permeability due to better connectivity of their micropore network. Type I microporosities in the wackestone and packstone textures have the smallest DOM size with good electrical flow properties but with negligible permeability.

The PoA values range from 474.8 to 6036.3 mm^{-1} . The values are generally high because the factor is size dependent, and MsDIA incorporates much smaller pores than conventional thin-section analysis (Weger et al., 2009). Intricate pore networks with high PoA are favorable for electrical flow, and simple pore networks are favorable for fluid flow (Figure 2.5B). The value of PoA is the lowest (simple pore structure) in the dolomites with type II micro- porosity, but also low in the ooid bindstone and travertine with types III and IV microporosity, respectively. The wackestone and packstone textures with small intercrystalline type I microporosity show the highest values for PoA.

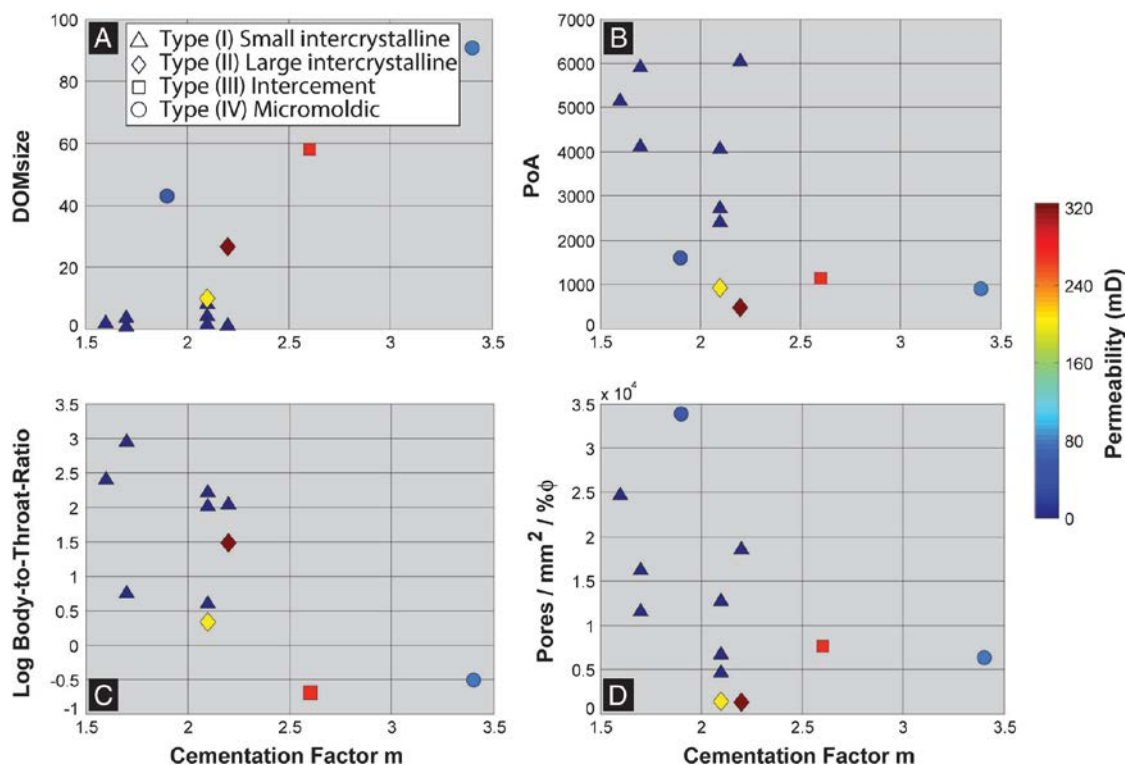


Figure 2.5: Quantified pore structure parameters plotted against cementation factor, color-coded with permeability. Marker shape represents type of microporosity. Samples with many small and complex pores show lower cementation factors and lower permeability. (A) DOMsize = dominant pore size; (B) PoA = Perimeter over area; (C) Log of pore body to throat ratio; (D) Pore density normalized by porosity. Pores per square millimeter per percent porosity.

Body-to-throat-ratios range from 0.5 to 1217. Large BTR values indicate small pore throats (D_c) compared to pore bodies (DOMsize). The BTRs show an inverse correlation with electrical resistivity. Samples with type I microporosity have high BTR values, low electrical resistivity, and low permeability (Table 2.1; Figure 2.5C). Samples with low BTR values like the dolomite and ooid bindstone rocks with types II and III microporosity have high permeability. The travertines with type IV microporosity can have very low and very high BTR values, but the sample with the low BTR has the high permeability.

Normalized pore densities range from 1267 to 33; 905 pores/mm². The Pd_{norm} is the lowest in the dolomites with type II large intercrystalline microporosity and can be very

high in the travertine with their micromoldic type IV microporosity (Figure 2.5D). Generally, samples with many small and complex pores have lower values for cementation factors, i.e., good conductivity for a given porosity. Conversely, these are less favorable for fluid flow and show lower values for permeability.

Power Law Pore-Size Distributions and Fractal Dimension D

The multiscale pore-structure investigation reveals a power law behavior in the PSD in all samples across the entire range of investigation (six orders of magnitude) (Figure 2.6). The linear trend on a double- logarithmic plot is the characteristic signature of a power law distribution of pore size, indicating fractal scaling and self-similarity of the pore structure at different scales. The fractal dimension D is hereby given by the absolute or inverse value of the negative slope of the best linear fit (regression line) of the distribution. The fractal dimension D can be interpreted as a measure of the complexity of a system, similar to the PoA parameter.

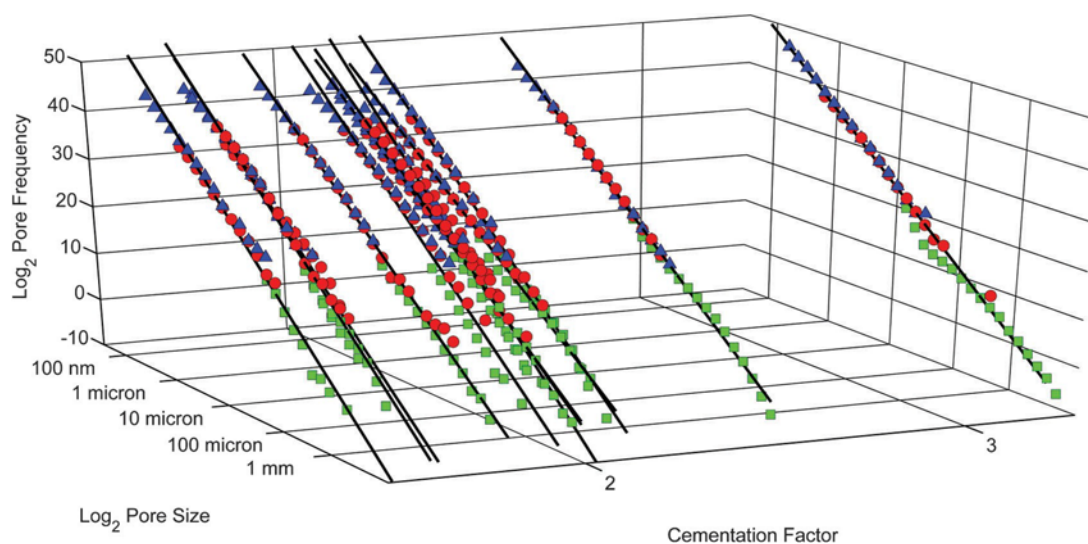


Figure 2.6: Pore-size distributions (PSD) of the 12 carbonate rocks. Logarithm of normalized pore frequencies (y-axis) as function of logarithm of pore-size bin (x-axis), using nonlinear binning (subsequent bin sizes doubling in size). Pore areas are expressed in size equivalent diameters (d_{eq}). The z-axis represents values for cementation factors of the sample. Different markers represent the used imaging

technique or resolution; PSD in all samples exhibit a linear behavior with high R^2 values, i.e., self-similarity of the pore space and predictability of distributions from subsets. The slope of the regression line represents the power law exponent and fractal dimension D of the PSD, which is a measure of the complexity of the pore system. Regression line slopes are steeper for the more microporous (more complex) samples to the left, which have lower cementation factors.

Values for D range from 1.67 in samples with type II large intercrystalline microporosity to 2.15 in samples with type I small intercrystalline microporosity (Table 2.1). The fractal dimension D also correlates with the flow properties of the rock. Samples with steeper slope (higher complexity) show lower cementation factors and lower permeability (Figure 2.7). The parameter D also describes how fast measurements increase or decrease in a sample; hence, it is a good measure of how macro- and micropores are distributed. Samples with many small pores (types I and IV microporosity; wackestone, packstone, and travertine) have steep slopes, whereas samples with few large pores (types II and III microporosity; dolomite, ooid bindstone) have gentle slopes.

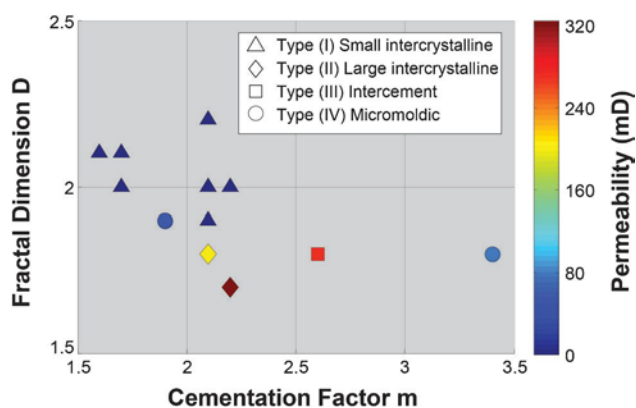


Figure 2.7: Fractal dimension D of pore-size distribution plotted against cementation factors, color coded with permeability. Marker shape represents type of microporosity. Samples with higher fractal dimension (steeper slope and higher complexity) show lower cementation factors and lower permeability.

Mercury Injection Capillary Pressure: Critical Pore-Throat Diameter

The D_c range from 0.01 to 160 μm in the analyzed samples where D_c shows an inverse correlation with electrical flow and positive correlation with permeability. A smaller critical diameter implies that the pore structure is interconnected with pore throats of a smaller diameter. Samples with small D_c have low cementation factors and low

permeability (Table 2.1; Figure 2.8), documenting the differences between electrical and fluid flow. Samples with small intercrystalline type I microporosity show the smallest critical diameters, and type II microporous samples show slightly larger values because of their larger crystal sizes; D_c is the second largest in the ooid bindstone with type III microporosity, which also shows the second largest cementation exponent. Travertine rocks with type IV microporosity can have small and large D_c values, in which the travertine with the smaller D_c has the lower cementation factor but also less permeability. The travertine with the large D_c has the highest cementation factor among the tested samples. The results corroborate earlier findings that an intricate micropore network with its inherent abundance of small pore throats has a positive impact on electrical flow properties (Swanson, 1985; Wang et al., 2005; Verwer et al., 2011).

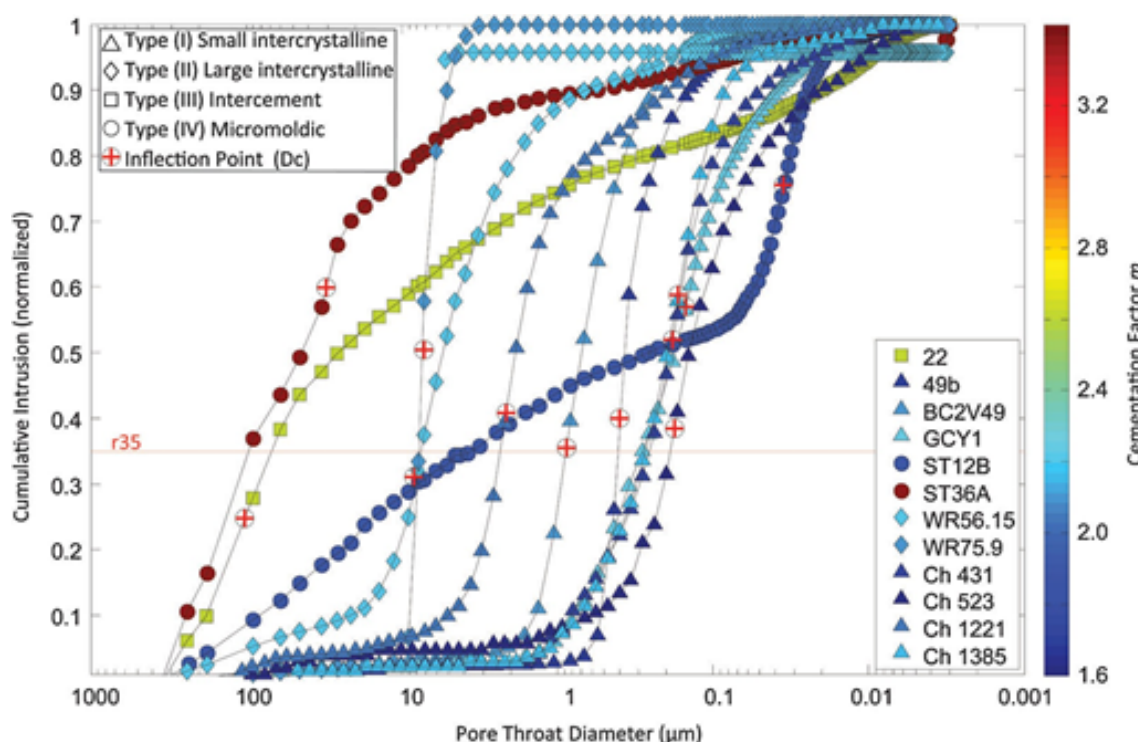


Figure 2.8: Normalized mercury injection capillary pressure intrusion curves, color coded with cementation factors. Marker shape represents type of microporosity. Red crosses mark critical diameters (D_c) at inflection points in rising part of curve where mercury spans the sample and percolation begins. Samples with larger critical diameters D_c (to the left) have higher cementation factors (warmer colors).

Discussion

Multiscale Pore Geometries

Heterogeneity across several length scales has been the central point for many petrophysical studies of carbonate rocks in the past (Eberli et al., 2003; Smith et al., 2003; Ahr et al., 2005; Rezende et al., 2013; Garing et al., 2014). These studies mostly focused on macroporosity. However, the relevant pore sizes for electrical conduction span from macro- pores down to nanopores because electrical flow is heavily influenced by microporosity (Verwer et al., 2011). To encompass the heterogeneity, this study uses imaging techniques with different resolutions for a MsDIA of the pore network. Conventional thin-section DIA is used to analyze the macropores, and the BIB-SEM method is used to analyze micro- and nanopores. More than 99% of the pores resolved in the BIB-SEM mosaics are below the resolution of conventional thin-section DIA. Inclusion of micro- porosity is essential as any pore large enough to accommodate a fluid or gas molecule is able to contribute to electrical or even fluid flow (water molecule size: 0.3 nm; methane: 0.4 nm; Bustin et al., 2009). Because the resolution of the BIB-SEM method (18.5 nm) is just slightly larger than these molecules, the extracted pore geometries from the MsDIA are considered to be representative for all pores that are accommodating electrical and fluid flow in a plug sample.

The size (DOMsize) and complexity (PoA) as well as the total amount of pores (Pdnorm) are important parameters for both electrical and fluid flow. We see clear trends of small and intricate pore systems with many pores being favorable for electrical flow, independent of rock type. Samples with small DOMsize, high PoA, and high Pdnorm show

good conductivity but low permeability (Figure 2.5A, B, D). This holds true especially for samples with the same type of microporosity.

Outliers exist in the travertines and tufas. These microbialites can have strong anisotropic properties due to extensive layering. The layering can drastically increase or decrease the connectivity of the pore network in a given direction. The layers can contain large, aligned pores, which act as a fracture-type porosity with excellent flow properties along the alignment. Furthermore, the travertines contain type IV microporosity (Figure 2.4D) of bacterial origin (Chafetz, 2013). This type of microporosity is unconnected and inaccessible for transport of charge or fluids.

The 2-D analysis presents certain limitations for correlations with 3-D plug properties. Heterogeneity of a sample can greatly reduce the representativeness of a single slice with respect to the whole plug. This is especially true for layered and vuggy rocks. However, previous experiments with micro-CT (computed tomography) volumes suggest that 2-D images are representative for the 3-D plug volume (Weger et al., 2009). Pore properties and porosity, calculated on all slices of a tomographic image series, do not deviate considerably from slice to slice. Each slice gives a good representation of the 2-D pore areas. Bloecher and Zimmermann (2008) also found from numerical modeling of isometric porous media that 2-D sections through modeled pore networks sufficiently represent their 3-D geometry. The 2-D analysis cannot, however, describe the topology and connectivity of the pore network in 3-D.

Types of Microporosity

Classification into micropore types according to pore-geometric parameters and petrophysical properties enables the assessment of flow properties based on qualitative

analysis of the micropore structure, possibly simplifying evaluation of reservoir properties. The different types of microporosity reflect the heterogeneity of carbonate samples with their distinctive genetic and diagenetic variances (Figure 2.4). Despite the strong variability, we see a correlation of rock type with a certain type of microporosity. This implies that conventional rock typing and qualitative rock descriptions can be used to assess the type of the micropore structure, which would help to predict the inherent flow characteristics. Conventional rock typing definitions could be improved by incorporating information about their microporosity types.

The type of microporosity strongly influences both electrical and fluid flow properties (Table 2.2). Samples with type I microporosity show good conductivity (low cementation factors) but low permeability. The low permeability is due to the complexity and tightness of the pore network between the small microspar crystals, which does not allow for effective fluid flow. The good conductivity originates from the low tortuosity of the very homogeneous and dense pore distribution of the crystalline microspar network. Strong diagenetic alteration of primary constituents into crystalline microspar leads to absence of solid areas within the sample, which could act as obstacles in the flow path (e.g., the ooids in the ooid bindstone). The result is a homogeneous, microcrystalline rock with many small and straight electrical connections and low electrical resistivity.

Samples with type II microporosity show average conductivity (cementation factors approximately 2.0) but good permeability because their intercrystalline network between the large dolomite crystals is wide enough to allow for fluid flow. The increased crystal size and lower pore density increase tortuosity, resulting in lower conductivity than in small intercrystalline type I pore networks.

The sample with type III microporosity shows good permeability but low conductivity. The good permeability is a result of the larger pore sizes and the relatively simple pores. The micropore network in this sample is also well connected in itself; however, it only forms around the dense ooid grains. The ooid grains hereby act as obstacles in the flow path. This drastically reduces the homogeneity of the conducting network, increasing its tortuosity and lowering its conductivity.

The samples with type IV microporosity show low conductivity and moderate permeability. Conductivity is low due to the microporosity being moldic and unconnected. Conductivity and permeability are mostly attributed to the macroporosity. As a result, the flow path through solely the macro-pore network is highly tortuous; this impedes electrical flow but still allows for fluid flow. However, the petrophysical properties are often anisotropic because the type IV microporosity is inherent to microbial rocks (travertines), which show extensive layering at macropore scales.

Type of Microporosity	PoA	DOMsize	Pore Density	Tortuosity	Conductivity	Permeability	
Type I	Small intercrystalline	High	Low	High	Low	High	Low
Type II	Large intercrystalline	Low	Medium	Low	Medium	Medium	High
Type III	Intercement	Medium	High	Medium	High	Low	High
Type IV	Micromoldic	Medium	High	High	High	Low	Medium

Table 2.2: Types of Microporosity and Attributes of their Pore Geometries in Relation to their Flow Properties (Electrical Conductivity and Gas Permeability) *PoA = perimeter over area; DOMsize = dominant pore size.

Fractal Pore Space

All samples show a power-law behavior in PSD across the investigated length scales. The power-law distribution indicates self-similarity of the pore space. Self-similarity implies that any part of the pore system, appropriately enlarged, looks like the whole (Mandelbrot, 1967; Purkis et al., 2005). It also implies that relative pore densities outside

the scale of investigation can be predicted, possibly up to core scale or the size of karstic features (Turcotte, 1993).

This is unexpected given that carbonates usually have very heterogeneous pore structures, e.g., the wackestone with its dual-porosity network of leached bioclasts in a matrix of crystalline microspar. This would generally point towards a multifractal behavior, where the system cannot be described by a single power-law exponent. Nevertheless, self-similarity is given in all samples of this study. It is also visually prominent, particularly in the ooid bindstone (Figure 2.9).

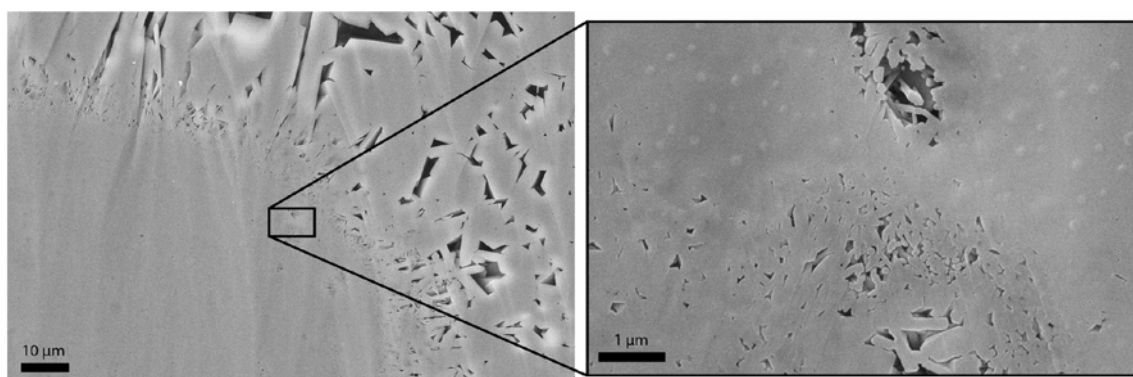


Figure 2.9: *Zoom into pore structure of ooid bindstone, demonstrating the self-similarity of the pore space at different scales. Microporous calcite cements around ooid grain (left: 2500× magnification) show similar shape and distribution as nanopores inside the ooid (right: 35,000× magnification).*

Self-similarity is deemed to be the result of a single or similar physical process on all scales. However, there is no general model yet that would explain the occurrence of fractal properties in natural porous media. Katz and Thompson (1985) claim that steady-state crystal growth is likely to create self-similar pore geometries. Webb (2001) states that the physical processes that form the rock determine if it will have a fractal pore structure. Generally, carbonate rocks can be seen as a result of different physical processes. Carbonate grains are mostly produced by organisms whereas the cement is produced by

abiotic crystal growth. However, one could argue that the carbonate grains are formed by biotic crystal growth. This would make the entire genesis of carbonate rocks a crystalline process and explain their self-similarity. Furthermore, diagenesis is another physical process that affects carbonates across all length scales, hence could also be used to explain their self-similarity.

Several other authors find similar fractal PSD in noncarbonate rocks that are not or are only partially of crystalline origin (Curtis et al., 2010, 2012; Ambrose, 2011; Hemes et al., 2013; Klaver et al., 2012; Houben et al., 2013, 2014). Hemes et al. (2013) determine a power-law distribution of clay pore sizes over three orders of magnitude, which they interpret as self-similarity of the pore space. Curtis et al. (2012) and Ambrose (2011) use 3-D imaging techniques for their investigations, underlining the validity and relevance of our 2-D measurements. The authors further postulate that their observations indicate the possibility to up-scale their results, which our present study corroborates with power-law PSD from BIB-SEM up to thin-section scale. Radlinski et al. (2004) find fractal distributions of pore sizes between 2 nm up to 50 μm , in which the results for pore sizes larger than 50 μm show Euclidean distribution. Krohn (1988) observes fractal distributions in the part of the porosity that is affected by diagenesis. She suggests that the relative amount of fractal porosity could be used to quantify the amount of diagenesis in sandstones. This is remarkable as carbonates are usually affected by diagenesis across all length scales, which would explain the fact that we see a uniform fractal PSD in the entire investigated pore-size range.

If the scale-invariant PSD holds up in future studies, it would help to predict micro- and macro-pores from DIA by reducing the necessary analytical procedures. Micropore

distributions could be modeled with results from simple and cost-effective DIA on thin sections. On the other hand, drill cuttings could be used for BIB-SEM analysis and estimates of the hydraulically important macro-pore distribution. The consistency of the logarithmic behavior of the PSD across different rock types still requires more verification. Yet, fractal scaling appears to be a re-occurring theme in nature, which takes place at all scales and in various rock types and geological settings. Sahimi (2011) states that fractals have to be taken into account for any realistic modeling of transport properties and displacement processes in porous and fractured media. The predictability of PSD could prove very useful for petrophysical and reservoir modeling applications, where direct methods of observation may be limited and modeling of the pore space is inevitable.

Mercury Injection Capillary Pressure: Critical Pore-Throat Diameter

The pore-throat diameter has a large effect on permeability of a sample (Webb, 2001). Due to the small sampling size, MICP measurements often cannot account for the macroscopic heterogeneities in carbonate rocks. In addition, a recent paper by Klaver et al. (2015) using Wood's metal injection has shown that in some rocks, the mercury does not enter the pore space, and the results are erroneously interpreted as injection. Consequently, the MICP method does not reliably describe the porosity, which is exemplified in relatively low total intrusion values as compared to helium porosity in some samples. However, the excellent correlation of D_c with flow properties suggests that, at least in this data set, measurement errors are negligible and the matrix with the micro-porosity is the dominant control on both electrical and fluid flow (Figure 2.8).

The results from throat-size analyses corroborate Verwer et al.'s (2011) assumptions that smaller individual pore throats (small D_c) facilitate electrical flow as the sum of the

many pore connections in microporous rocks add up to a large apparent cross-sectional area. Samples with D_c less than 2 μm mostly have very low permeabilities, similar to what has been proposed by Hulea and Nicholls (2012). This again highlights the differences in how pore geometries influence electrical and fluid flow.

Pore Body-to-Throat Ratio

The concept of “electrical efficiency” implies that most of the current is passing through the pore on a narrow path (“throat tube”) with a cross section similar to that of the pore throat (Herrick and Kennedy, 1994). The BTR gives an indication of how much of the pore space can effectively be used to transport electrical charge. High BTR indicates high amounts of unusable pore volume. Pore volume is considered unusable for conduction of electrical charge if it is not part of a direct connection between the “entrance” and “exit” pore throats of a pore. A higher BTR means that throats are small compared to the pore cavities, which results in large parts of the pore volume not contributing to conduction of electrical charge and as a consequence impedes electrical flow and increases the resistivity (Adisoemarta et al., 2001; Kazemzadeh et al., 2007; Abousrafa et al., 2009).

Our results show the opposite trend: larger BTR, e.g., in the samples with type I small intercrystalline microporosity, result in lower resistivity (Figure 2.5C). It is the large quantity of small pores and pore throats, which combined have a large apparent cross-sectional area, facilitating electrical flow. A dense pore network with many small pores also has more linear flow paths, effectively reducing its tortuosity and resistivity (Figure 2.10).

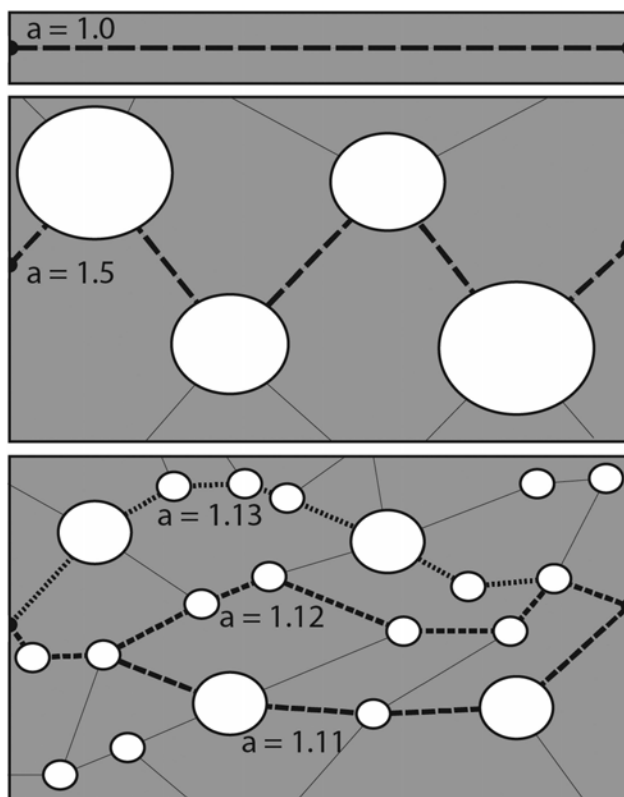


Figure 2.10: Concept of tortuosity (a) as in deviation from a straight line without tortuosity (top: $a = 1.0$). Example with same porosity but larger pores (middle: high tortuosity) has less and more sinuous connections than sample with small pores (bottom: low tortuosity).

Micropore networks are also often of crystalline nature such as in types I and II microporosity. Total recrystallization with destruction of original constituents and fabrics would lead to a more homogenous pore network without obstacles (e.g., in type III microporosity) and dead-end pores (type IV microporosity), reducing tortuosity. Crystalline pore networks generally have high coordination numbers. More connections then lead to multiple flow paths through a single pore body, effectively compensating for effects of higher BTR values. However, type I small intercrystalline microporosity and its many small connections are counterproductive for permeability and reservoir performance, as recovery efficiency decreases due to earlier “snap-off” effects where the continuity of the nonwetting phase is disrupted (Wardlaw and Cassan, 1978; McCreesh et al., 1991). Dolomitization, on the other hand, is known to enhance carbonate reservoir properties also

due to the creation of a crystalline pore structure (type II microporosity) with flow paths large enough for effective permeability (type II large intercrystalline microporosity).

Janssen et al. (2011) found high BTRs in clay-bearing samples and low ratios for clay-free samples, as inferred from MICP drainage and imbibition curves, because increased clay content increases conductivity in a sample. This finding is in conformance with our results, in which high BTR values go along with high conductivity. However, inferring BTR from a bulk method such as MICP remains questionable, and MICP does not directly relate the size of the individual pore to the size of the throat it has been filled through; it only relates the fraction of filled porosity to the pore sizes that control this state during intrusion and extrusion (Webb, 2001). In this study, we use a combination of directly imaged pore-size parameters (DOMsize) and a statistical pore-throat parameter (D_c), both having demonstrated their significance for bulk flow properties of rocks or porous media. It has to be emphasized that this method does not compare the pore size of an individual pore to the individual throat, but only the averaged pore-network parameters. Additionally, pore sizes derived from 2-D images are statistically underestimating the real pore sizes. The 2-D sections cut the pores at various angles, rarely sectioning directly through the center of a pore. Advances in 3-D x-ray microscopy might enable direct assessment of BTRs in micro-pore networks in the near future (Merkle and Gelb, 2013).

Permeability versus Conductivity

The producibility of a formation is largely controlled by the permeability and water saturation of the rock. Permeability, similar to electrical resistivity, is mainly a function of pore geometry and connectivity. Hence, electrical resistivity logs are used to estimate permeability and calculate water saturations (Suman and Knight, 1997). The challenge in

using electrical logs for permeability estimation and reservoir flow is the disparity between fluid and electrical flow (Figure 2.5). This disparity is due to their different flow mechanisms. Permeability is dependent on the physical transport of molecules through the pore network, whereas ionic charge can still be conducted only along brine-wetted surfaces and through the smallest pore throats. As a result, electrical charge can still be transported in microporous rocks with low total porosity and low water saturation. This can lead to an overestimation of permeability or water saturation.

Verwer et al. (2011) postulate that the main factor contributing to high conductivity in microporous rocks is the larger apparent cross-sectional area, which is a result of the increased pore density and co-ordination numbers of the intricate pore system, independent of the individual size of the conducting element (pore throat). Permeability, on the other hand, is strongly influenced by the effective pore- network size and scales well with the amount of pore network that is accessible through pore throats larger than 2 μm in diameter (Dixon and Marek, 1990; Hulea and Nicholls, 2012). In addition, the shape of the pore opening has little influence on the flow of electrical current, i.e., pores can have very narrow slit shapes. This is in contrast to permeability, which is influenced by capillary forces and the absolute size of a pore throat, which is the shortest axis of the throat opening (Beaumont and Foster, 1999).

Also, electrical resistivity is directly related to the length of the conducting element. Hence, it is much more dependent on tortuosity than permeability. Electrical current always follows the least tortuous path, and samples are less tortuous at microscopic scales (Ehrlich et al., 1991). By adding microporosity between larger macropores, the flow paths become less sinuous and also more numerous (Figure 2.10). The more narrow nature of the flow

path hereby plays an insignificant role for the conduction of electrical charge, as opposed to permeability. As a result, microporous rocks often have excellent electrical flow properties but low permeabilities.

Furthermore, flow mechanisms in micropores and nanopores are most likely different from mechanisms controlling flow in macropores. Darcy's law is probably not sufficient to describe fluid flow at nanometer scales, where atomic bonds and other factors come into play (Curtis et al., 2010). High irreducible water saturations in carbonate micropores and increased double-layer conductivity are known to enhance electrical flow, but not permeability. In fact, numerical methods suggest that double-layer conductivity creates an electric force in reverse direction to fluid flow, further lowering permeability in micro-channels (Gong and Wu, 2006). All of these parameters will have to be considered to effectively predict electrical properties of rocks in further studies.

Conclusion and Implications

The microstructures of 12 carbonate rock samples of different rock types have been imaged in very high detail and range. Image analyses of nanometer- resolution BIB-SEM mosaics and micrometer- resolution thin-section images have been combined to effectively quantify pores from nanometers to millimeters in size to include all length scales relevant to petrophysical plug measurements of electrical resistivity and permeability.

Results show that the amount and type of micro- porosity has a strong influence on electrical flow properties. The BIB-SEM mosaics reveal four types of microporosity in the analyzed samples: small intercrystalline (type I) in the packstones, wacke- stones, and tufa; large intercrystalline (type II) in the dolomites; intercement (type III) in the ooid bind- stone; and micromoldic (type IV) in the travertines. Crystalline types of microporosity

(types I, II, III) increase pore network connectivity whereas microbial type IV microporosity is micromoldic and unconnected. However, only the larger types II and III microporosity contribute to permeability because pore connections in type I micropore networks are too narrow to allow fluid flow. Information about the micropore geometry of the rock will improve the assessment of its reservoir properties.

Quantified pore geometric parameters derived from MsDIA indicate that electrical and fluid flows behave in exactly opposite ways with regard to pore structure. Samples with a tight pore network, consisting of many small and complex pores with small throats, show better conductivity but lower permeability than samples with a large pore network, consisting of fewer large and simple pores with large pore throats. This behavior is attributed to the higher number of pore connections and lower tortuosity of most micropore networks that allow for effective transport of ionic charge but are too narrow for fluid flow.

Furthermore, PSDs in all samples follow a power law, implying fractal scaling of pore sizes. The fractal dimension D of the power law distribution thereby is a measure of the complexity of a system and has been shown to correlate with flow properties. More complex samples with higher fractal dimension (steeper slope) show higher conductivity but lower permeability. The power law also enables modeling of PSD outside the range of observation. It allows us to predict the amount of micro- or macropores in data- scarce scenarios and hence enhances estimates of reservoir properties. Additionally, the power law could be used to develop scaling rules in reservoir models. However, uniform scaling rules seem to be applicable only to carbonate reservoirs because siliciclastic rocks often show multifractal and Euclidean PSD. This is possibly related to the dissimilar genesis of their constituents (transported grains versus in situ cements). The monofractal scaling in

carbonates, on the other hand, could be attributed to the crystalline, in situ origin of both their grains and cements, or to the consistent diagenetic overprint that affects all length scales of carbonate porosity.

Chapter 3: Fractal Pore Structure and Complex Resistivity Spectra (CRS) for Estimating Permeability in Dolomites from the Mississippian Madison Formation, Wyoming

Summary

Dolomite rocks constitute many important reservoirs units due to the porosity-preserving and connectivity-enhancing effects of dolomitization. This study explores the correlation between resistivity and pore structure in dolomite rocks from the Mississippian Madison Formation in Wyoming and proposes a novel approach of predicting permeability from complex resistivity spectra (CRS).

Digital image analysis (DIA) on thin-sections is used to quantify the pore structure and obtain pore size distributions of 54 sucrosic dolomite samples. The non-linear binning and plotting on log-log scale reveals a power law in the pore size distribution in all samples, indicating fractal scaling of pore geometries in these dolomite rocks. Pore-structure parameters derived from DIA are correlated to resistivity values of each plug and show that larger and simpler pore networks result in higher cementation factors. Crystal size, on the other hand, appears to have a minor impact on the flow properties in these sucrosic dolomites.

Analyzes of complex resistivity spectra (CRS) are performed on brine-saturated core plugs in a log sweep from 0.1 – 100,000 Hz with a four-electrode setup at varying confining pressures. Results show that the frequency dispersion of CRS between 100 – 100,000 Hz is directly related to the porosity in these dolomites. The phase shift of CRS shows high variance in both low and high porosity samples with a characteristic slope β for frequencies between 100 – 2,000 Hz. Modifying an empirical model of Tong & Tao (2008) to include

the slope β together with porosity and cementation factor m can predict permeability with a correlation coefficient of $R^2 = 0.82$.

Introductory Remarks

Previous studies on electrical properties in carbonate rocks (Verwer et al., 2011; Norbistrath et al., in press) demonstrate the favorability of intricate pore networks for electrical flow. Microporous rocks with many small pores generally showed lower cementation exponents than samples with large and simple pores. The data sets used in these earlier studies are all containing a wide spectrum of carbonates, both limestones and dolomites, with highly variable pore sizes and shapes. This data set is concentrating on dolomites that are known to be good reservoirs to great depth. Dolomitization has increased the ability of the rock to retain porosity with depth and reduced the occurring pore types to intercrystalline and moldic pores.

In this paper dolomite samples from the Mississippian Madison Formation in Wyoming are used for two investigations. First the correlations between pore geometries and petrophysical properties (permeability, resistivity, and acoustic) are assessed. Second, we expand the assessment of the electrical properties from the cementation exponents to the analysis of complex resistivity at varying frequencies. Commonly, the cementation exponent is calculated from the amplitude of resistivity at a single frequency around 1 kHz. Analysis of complex resistivity spectra (CRS), however, includes measurements of both amplitude and phase shift of resistivity in a frequency range from 0.1 – 100,000 Hz. The benefit of CRS analysis of brine-saturated core plugs is the assessment of the low-frequency interfacial polarization effects that are believed to be controlled by the geometry of the fluid-filled pore structure, which enables to relate resistivity to flow properties.

The motivation for the analysis of CRS in the sucrosic dolomites is previous work by Tong & Tao (2008), who found a strong correlation of the slope of the phase shift of complex resistivity in the 100 – 2,000 Hz range with permeability in shaly sandstone samples. The goal is to improve the understanding of the connection between the frequency dependency of resistivity and the dolomite pore structure. The outcome is intended to improve inversion of dolomite reservoir properties like porosity and permeability from resistivity data.

Complex electrical properties of porous media

Resistivity in brine-saturated rocks is a complex entity as the current signal that is measured to calculate the resistivity is shifted in phase compared to the applied voltage/input signal. Hence, resistivity cannot be described solely by the change in amplitude, but has to include information about the phase shift. This description can only be achieved with a complex number, consisting of a real part (amplitude), and an imaginary part. The imaginary part can be described by the phase shift, dielectric constant, or relative permittivity of the sample, which are different measures for the same effect. Relative permittivity (or dielectric constant) relates to a rock's ability to transmit or permit an electric field between two charges; it is the factor by which the electric field is decreased or increased relative to vacuum. However, only the phase shifts can be measured directly and do not have to be derived (Anderson et al., 2008). The phase shift is caused by polarization effects that cause the rock to store energy between alternating cycles. Inherent polarizability is the characteristic feature of a dielectric material.

This dielectric effect is frequency dependent, as it is controlled by different effects, namely electronic polarization, orientational polarization, and interfacial polarization (Bean et

al., 2013; Fig. 1). As these effects work at different scales, namely atomic, molecular, and ionic (inter-molecular), their relative influence changes in significance for different frequency ranges. It takes much longer for an ion to shift its physical position within a pore than for an atom to shift the charge center of its electron cloud. Hence, the amount of phase shift of a current signal traveling through the rock is strongly frequency dependent.

Numerous studies have been conducted to study and utilize the complex electrical properties of sedimentary rocks in the past. Many studies focus on the dielectric constant at low frequencies, where rocks with high values of dielectric constant are linked to high clay content and its strong interfacial polarizability (Sen, 1981; Garrouch & Sharma, 1992). Other authors have linked dielectric properties to grain size distributions (De Lima & Sharma, 1991; Raythatha & Sen, 1986).

Zisser et al. (2010) report strong correlations between the relaxation time of spectral induced polarization (SIP) core-plug measurements and the effective hydraulic length scale, enabling assessment of permeability with low frequency (0.01 – 100 Hz) SIP methods. Slater et al. (2006) found similar correlations between interfacial polarization and specific surface area for measurements between 0.1 – 10,000 Hz on synthetic samples. They also cite other authors who found similar relationships at higher frequency measurements (Knight and Nur, 1987), and suggest that common mechanisms may control electrical properties across a wide frequency range. However, complex electrical properties in sedimentary rocks (name it relaxation times, phase shifts, dielectric constants, or relative permittivity) show high variability at different frequency ranges, which is also referred to as ‘electromagnetic dispersion’ (Wang & Poppit, 2013). This variability is due to the above

mentioned different polarization effects, working at different scales and hence “resonating” at different wavelengths (frequencies).

Complex resistivity spectra (CRS)

Rock petrophysical properties, such as specific surface area and permeability, can be estimated from phase shifts in the low-frequency range (Weller & Börner, 1996; Denicol & Jing, 1998; Cerepi, 2004). The relationship between pore structural and electrical properties is a result of the low-frequency phase shifts being directly correlated to the amount of electrical double layer (EDL), which increases with increasing surface area of the sample. Typically, electrical double layer effects are mainly associated with clays that are postulated to form this polarizable layer at the interface with an electrolytic solution due to their excess surface charge, resulting in phase shifts of an applied alternating current. However, studies of carbonate rocks also suggest that these rocks carry excess surface charges that are mostly associated with crystal defects, either because of structural defects or adsorption of foreign ions (Moulin & Roques, 2003). Moreover, results from the study presented here show that dolomite rocks exhibit distinct phase shifts in the low-frequency range where interfacial polarization is the main control on phase shifts. Hence, it can be assumed that dolomites also form an electrical double layer at the grain-brine interface.

Methods

General methods

Porosity is measured by comparing bulk density to skeletal density from Helium pycnometry utilizing Boyle’s law. Fluid permeability is determined from Klinkenberg-corrected gas permeability measurements by an external service provider. The average

crystal size is determined through point counting on thin-sections by measuring 50 crystals in a sample and averaging the length of their longest axis.

Digital image analysis (DIA) of accompanying thin-sections, following the methodology described by Weger et al. (2009), is used to extract pore geometry parameters DOMsize (dominant pore size) and PoA (perimeter over area). DOMsize is the minimum size of pores needed to occupy half of the porosity on a given thin-section and is a good indicator of the effective pore size in a sample. PoA is the perimeter of all pores over the area of all pores that are identified on a thin-section. It is a good indicator of the complexity of a pore network. To analyze pore size distributions, all identified pores from DIA are plotted on a histogram in log-log scale using non-linear binning, i.e. subsequent pore bins doubling in size.

The DIA method works well for samples with more than 10% porosity. Samples with less than 10 % porosity often have very few pores that can be identified on a thin-section, which makes the quantification of their pore geometries statistically questionable. Higher-resolution imaging techniques would include smaller pores and lower the porosity threshold below 10%, but the importance of the macropores would constrain a multiscale analysis (Desbois et al., 2011; Norbistrath et al., in press).

Spectral analysis of complex resistivity

1-inch core plug samples are saturated with 35 ppt NaCl brine by repeatedly pulling a vacuum over submerged samples during a 24-48 hour period. The dispersive behavior of complex resistivity at different frequencies is measured in the saturated samples. Amplitude and phase shift of complex resistivity are captured in a log sweep of 15 frequency steps from 0.1 – 100,000 Hz. The pore pressure is kept constant at 2 MPa and

the confining pressure of the surrounding oil is varied up to 22 MPa to enable measurements in a range of effective pressures (EP) up to 20 MPa. The purpose of the varying pressures is to simulate reservoir conditions in order to test if the resistivity of the core plug samples varies with increasing overburden (burial depth).

For the study of complex resistivity spectra, only measurements with an effective pressure of 20 MPa are used. For compliance with existing datasets, calculations of cementation exponent m are made from resistivity amplitude measurements at 10 MPa effective pressure for a frequency of 720 MHz (1 kHz requested frequency).

Resistivity measurements are performed with a NER Autolab 1000 system where electrical properties of core plug samples can be analyzed as a function of frequency, stress, and temperature. The system allows for true four electrode resistivity measurements in order to avoid erroneous contact resistance at the voltage contacts. Pore fluid conductivities are corrected for changes in temperature (Arps, 1953). Voltages are measured across a reference resistor and the sample. A digital oscilloscope records the signals, and the amplitude ratio and phase shift between the two signals is used to measure the complex electrical resistivity of the sample.

Complex electrical impedance can be described either in Cartesian or in polar form: In Cartesian form with a real (R-signal; ρ') and imaginary (X-signal; ρ'') part, or in polar form with a magnitude $|\rho| = (\rho'^2 + \rho''^2)^{1/2}$ [ohm meters] and a phase shift or lead $\Phi = \tan^{-1}(\rho''/\rho')$ [milliradians]. In this study, we measure the complex resistivity in Cartesian form but use the terminology of the polar form, as the term “phase shift” is more descriptive than the “imaginary part of electrical resistivity”.

Dataset

This study uses 54 dolomite samples from the Mississippian Madison Formation in Wyoming that have undergone complete dolomitization based on X-ray diffraction (XRD) analysis (>95% dolomite) (Westphal et al. 2004, Smith et al., 2004). Dolomitization is known to preserve and enhance reservoir properties because the re-crystallization often homogenizes the pore structure and the crystalline rock also better withstands compaction

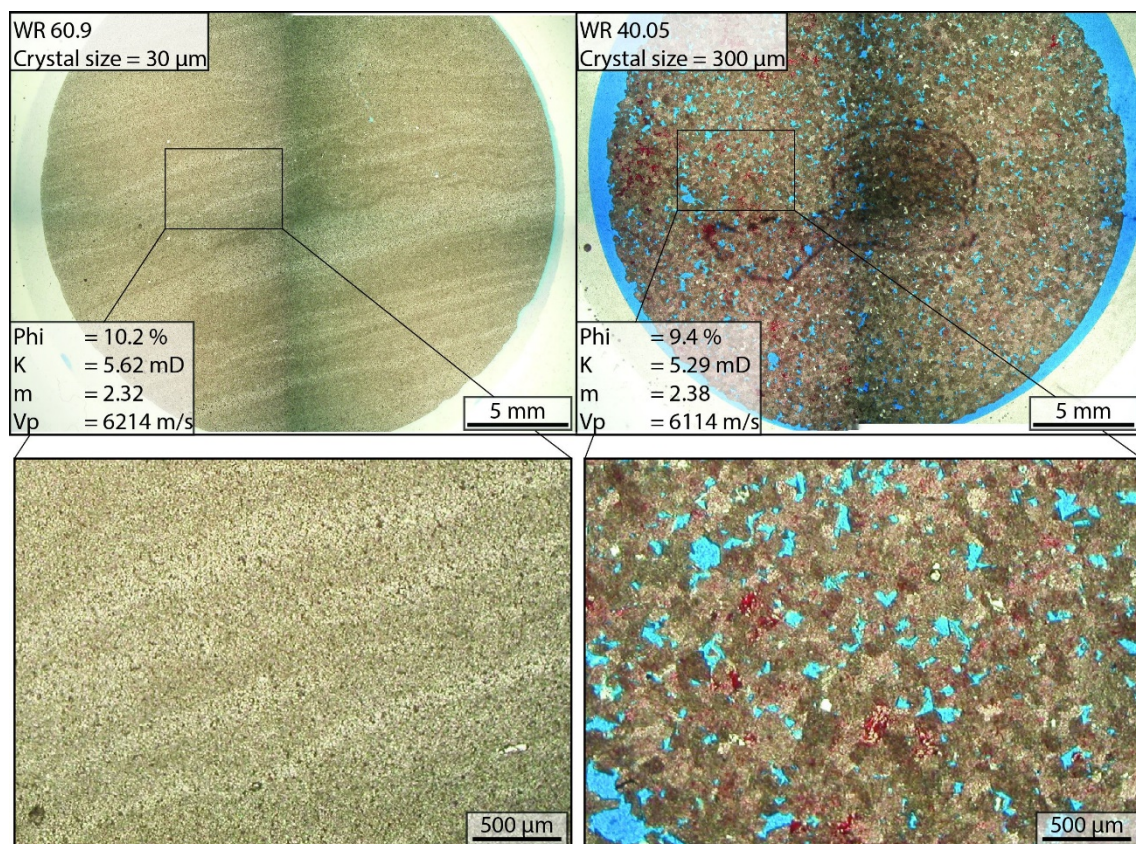


Figure 3.1: Stitched photomicrographs of two blue epoxy impregnated dolomite samples from the Madison Formation with significantly different crystal sizes but similar petrophysical properties. Left: Laminated fine-crystalline dolostone with intercrystalline microporosity. Right: Coarse-crystalline dolostone with mixed intercrystalline and connected moldic porosity. Bottom images show close up of the pore structure of both samples. The intercrystalline pores in the fine-crystalline sample on the left are invisible at 1x magnification. Intercrystalline and moldic pores visible in coarse-crystalline sample on the right.

to retain porosity with depth (Lucia, 1995). The dolomitization mostly destroyed the original fabric with remaining pore types being intercrystalline and moldic pores (Figure 3.1).

Results

Pore Structure

This part will show the pore structure properties of the samples gathered from thin-section analysis. These properties include crystal size from point counting and DOMsize, PoA, and pore size distribution from digital image analysis (DIA).

Crystal size

Average crystal (grain) sizes of the individual samples range from 28 – 298 μm in this dataset. Results show that the crystal size of a sample has little influence on its petrophysical properties (Figure 3.2). Samples with small crystal sizes can have high permeabilities, high velocities, and high resistivities. In contrast, samples with large crystal sizes can have low permeabilities and low resistivities, however they do not have low velocities.

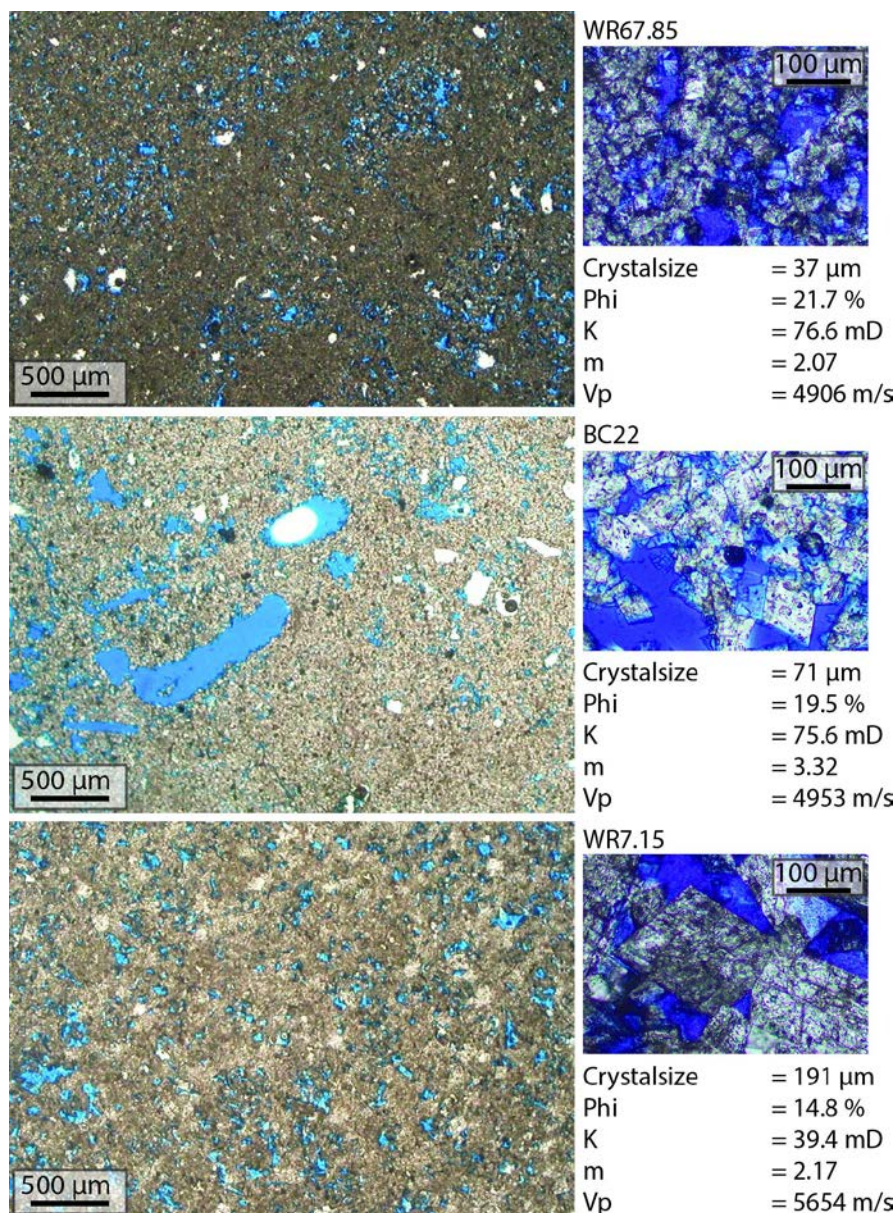


Figure 3.2: Three dolomite samples with different crystal sizes. Zoom at 10x magnification shows individual dolomite crystals. Petrophysical properties appear unrelated to crystal size.

DOMsize and PoA

DOMsize (dominant pore size) ranges from 18 – 622 μm and PoA (perimeter over area) from 28 – 240 mm⁻¹ in the dolomite samples. Out of the samples with more than 10% porosity, those with large and simple pores generally show higher cementation factors

(Figure 3.3). Large and simple pore structures are characterized by high DOMsizes and low PoA that are identified by DIA of thin-section images.

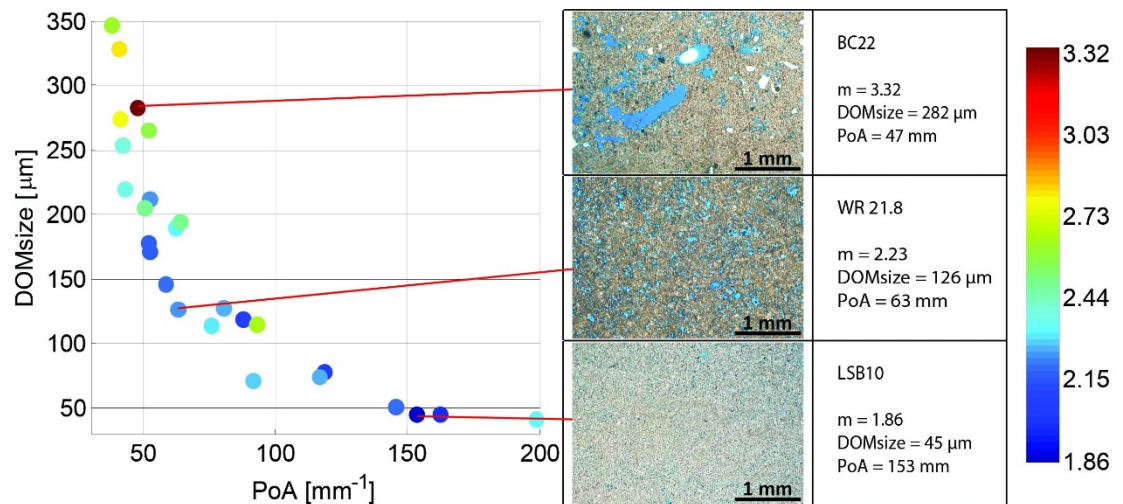


Figure 3.3: Plot of PoA vs DOMsize for samples with more than 10% porosity, color-coded with cementation factors. Samples with more intricate (higher PoA) and smaller pores (lower DOMsize) show lower cementation factors (blue color). Three representative samples illustrated on the right.

Power law pore size distribution

All samples show power law distributions of pore sizes across the investigated length scales (6 μm resolution limit up to thin-section size ~ 2.54 cm) as indicated by the good fit (average $R^2 = 0.95$) of a log-log linear regression curve to the data points (Figure 3.4).

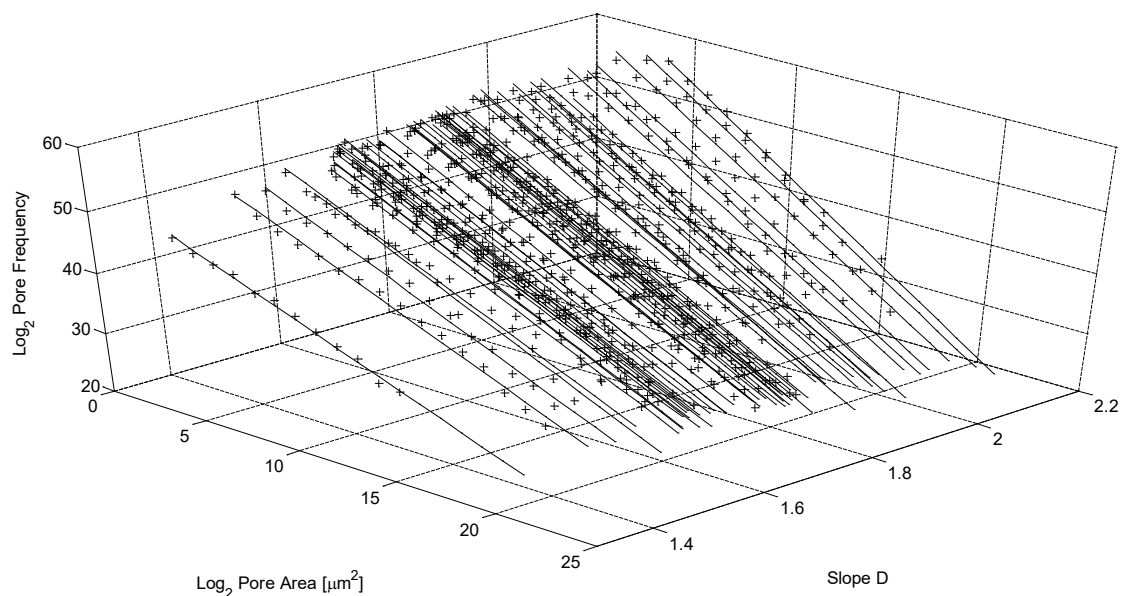


Figure 3.4: Pore size distributions of 54 dolomite samples acquired with digital image analysis on thin-sections, plotted on log-log scale using non-linear binning (subsequent bin sizes doubling in size). Z-axis: Slope D, or fractal dimension, varies between 1.35 and 2.2 in this dolomite dataset.

The slope D of the power law distribution is the fractal dimension of the sample (Pape et al., 1999). Values for the slope range from 1.35 to 2.2. A steeper slope D, similar to higher PoA, is indicative of a more intricate pore structure with lower cementation factors (Figure 3.5; left) and permeabilities (Figure 3.5; right), although the permeability trend is much weaker.

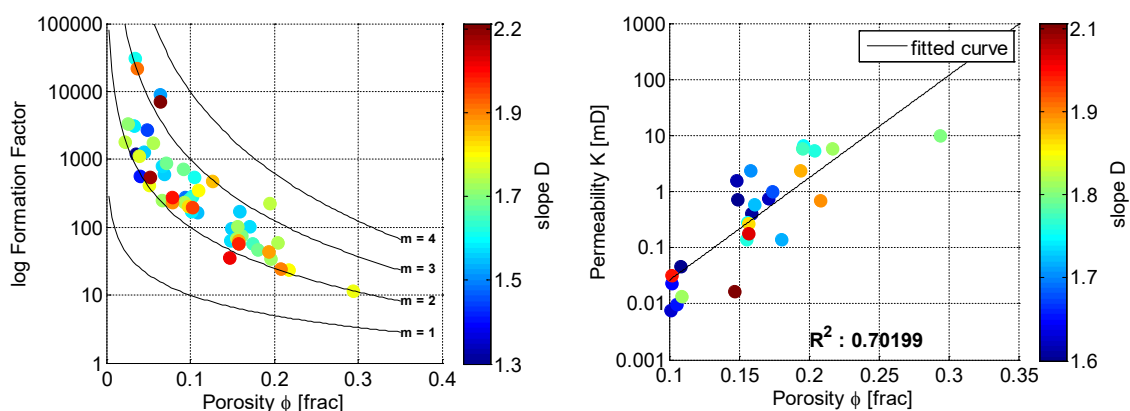


Figure 3.5: Two plots, both color-coded with slope D of power law PSD. Left: Porosity-formation factor cross-plot. Solid curves indicate lines of equal cementation factors from

1 to 4. In samples with more than 10% porosity steeper slope D results in a lower cementation factor around $m = 2$. Right: Porosity-permeability cross-plot for samples with more than 10 % porosity. Slight trend of higher permeability with lower slope D .

Porosity-permeability

Porosities in the samples range from 2 - 29% and permeabilities from 0.002 – 100 mD. Thin-section analysis identifies the samples as mostly sucrosic dolomites with well-connected intercrystalline pores and few vuggy pores (Westphal et al., 2004). As a result, the 54 dolomite samples have a strong correlation of porosity with permeability (correlation coefficient: $R^2 = 0.60$; Figure 3.6; left). The strong porosity-permeability relationship is not correlated to crystal size. There are no trends of larger crystal size resulting in higher permeability, as other studies have postulated for purely crystalline dolomites (Lucia, 1995). In contrast, samples with the smallest crystal sizes have the highest porosities and permeabilities (Figure 3.6; left).

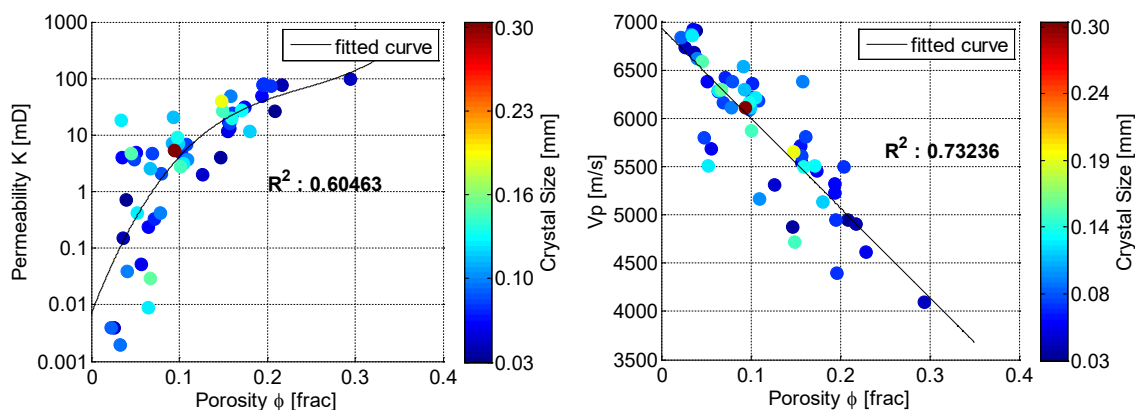


Figure 3.6: Left: Porosity-permeability cross-plot for 54 dolomite samples from the Madison Fm, showing good correlation of porosity with permeability ($R^2 = 0.60$). Right: Porosity-velocity cross-plot demonstrating strong correlation of porosity with velocity ($R^2 = 0.73$). Color-coding with crystal size reveals that crystal size has little influence on permeability or sonic velocities for a given porosity.

Acoustic velocity

Acoustic velocities in the samples are highly variable and range from 4,100 – 6,900 m/s. Acoustic velocity is strongly controlled by the total porosity of the sample. In general,

the measured velocities show an inverse correlation with porosity, but departures from the general trends of correlation can be as high as 1500m/s. These deviations can be explained by the occurrence of different pore types, crystal shapes, and rock types. The crystal size does not explain variations in velocity for a given porosity (Figure 3.6; right), except that samples with large crystal sizes do not show low velocities, instead pore type and crystal shape influence acoustic velocity. Rocks with texture combinations of moldic and anhedral crystals have relatively high, whereas rocks with intercrystalline pore types and mostly euhedral crystal shapes have relative low velocities. In addition, rock texture influence velocity. Generally, grainstones have relative high velocities, whereas mudstones have relative low velocities. Breccias have the lowest velocities as a result of micro-fractures and fracture fillings of calcite and quartz (Shen et al., 2000). V_p/V_s ratios vary between about 1.61 and 1.97. There is a very weak correlation between the V_p/V_s ratio and the porosity as the ratio decreases with increasing porosity but some rules are seen. Rocks with combination of intercrystalline porosity and euhedral crystal shape have a relative low V_p/V_s ratio, whereas the breccias and rocks with moldic porosity (higher DOMsize) and anhedral crystal shape have a relative high ratio (Figure 3.7).

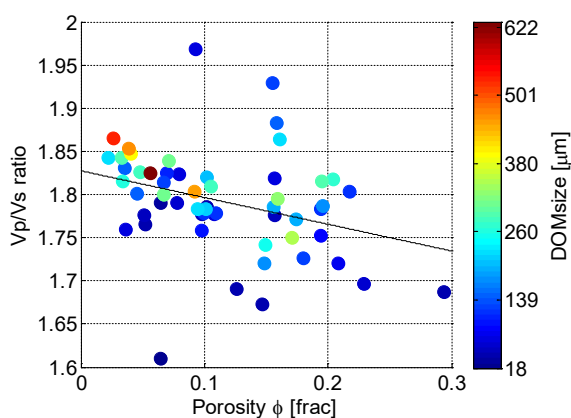


Figure 3.7: Porosity- V_p/V_s ratio cross-plot for 54 dolomite samples from the Madison Formation, color-coded with dominant pore size. Samples with larger DOMsize and more moldic porosity show higher ratios.

Cementation factor m

The cementation factors of the measured dolomites range from 1.8 to 3.3 (average: 2.4). This range is smaller than reported from other carbonate data sets that include limestones of variable textures (Lucia, 1983, Verwer et al., 2011). The measured cementation factors do not correlate to the permeability variations at a given porosity (Figure 3.8). This is in contrast to the carbonate data set measured by Verwer et al. (2011) that displayed a trend of higher permeability with higher cementation factors.

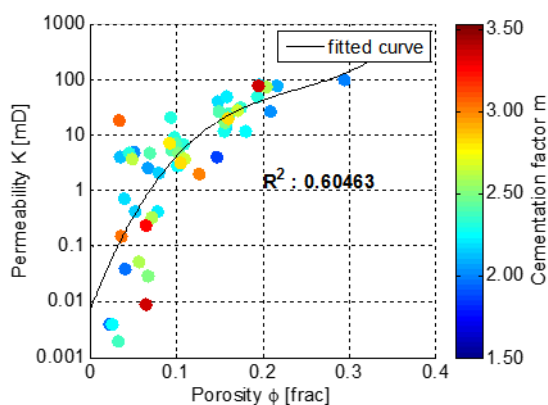


Figure 3.8: Porosity-permeability cross-plot. Color-coding with cementation factors shows no link between permeability to cementation factor.

Pressure dependency of resistivity

Resistivity only increases minimally with increasing pressure (Figure 3.9). The mean increase in cementation factor for measurements at 5 and at 20 MPA effective pressure is $3.2\% \pm 2.2\%$. The lack of pressure dependence of resistivity in these rocks documents how pressure resistant these dolomites are and how they can retain their porosity and permeability to great depths.

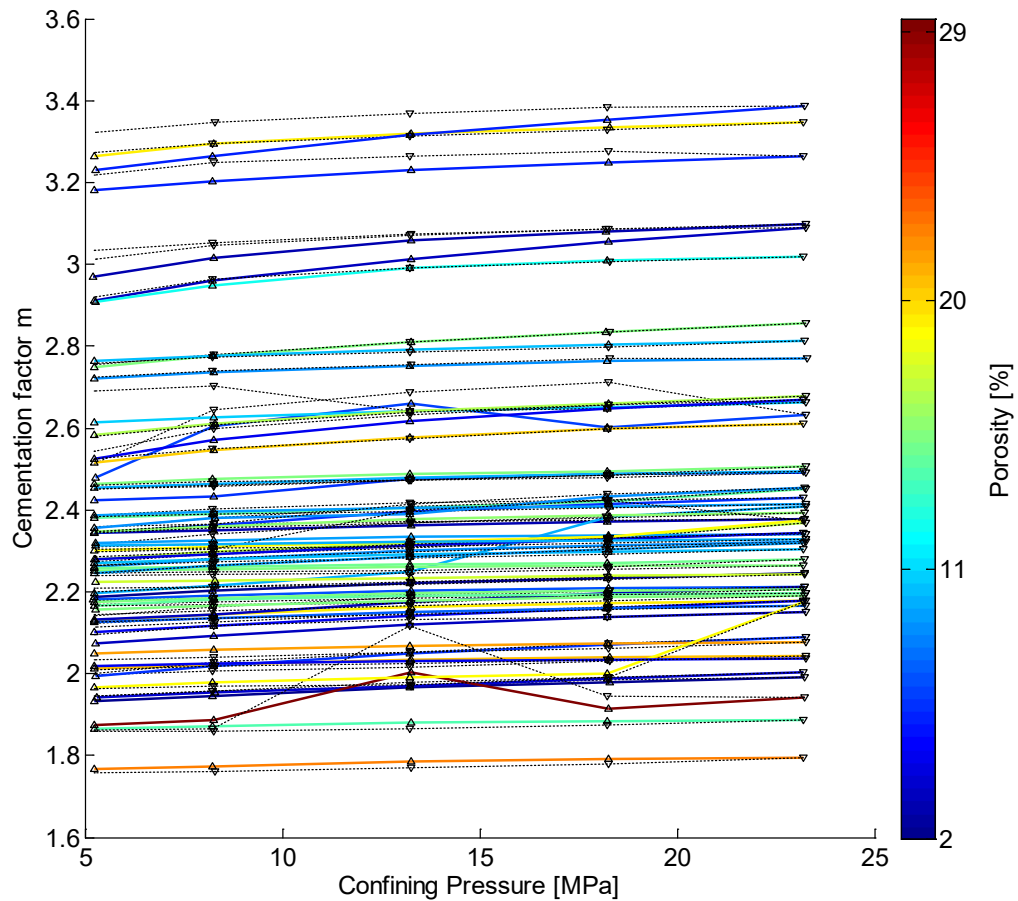


Figure 3.9: Plot of confining pressure vs cementation factor m demonstrates the minor effect of increasing pressure and overburden on electrical properties and pore structure. Increasing pressure leg color-coded with porosity. Decreasing pressure leg shown as black, dashed line.

Furthermore, the measured samples show little hysteresis effects when pressure is lowered. The average change in cementation factor at 5 MPa before and after being pressurized to 20 MPa is $+0.52\% \pm 1.1\%$. The small hysteresis effect also implies that the micropore structure of the plug samples can remain intact after being retrieved from great depths, and that measurements of cementation exponents in the lab can be representative for subsurface formations.

Complex resistivity spectra (CRS)

Analysis of complex resistivity spectra shows that the dispersive behavior of resistivity between 100 – 100,000 Hz is directly related to the porosity and also the permeability in sucrosic dolomites. The amplitude of resistivity stays relatively constant across the frequency spectrum for the samples with high porosity, which have generally low resistivities. For low-porosity samples the amplitude is generally high but drops at frequencies above 1,000 Hz (Figure 3.10; top). The phase shift shows more variance in both low and high porosity samples with a characteristic slope between 100 – 2,000 Hz (Figure 3.10; bottom). Similar to the amplitude, phase shifts are generally larger in low-porosity samples. Phase shifts peak at a certain frequency directly related to the porosity of the sample. This peak in resistivity phase shift appears to coincide with a decline in resistivity amplitudes, and occurs at a lower frequency in the lower porosity samples. The peak in the high porosity samples is actually not recorded as the measurement setup only allows for frequencies up to 100,000 Hz, but can be inferred to occur below the MHz range from the shape of the other phase shift curves.

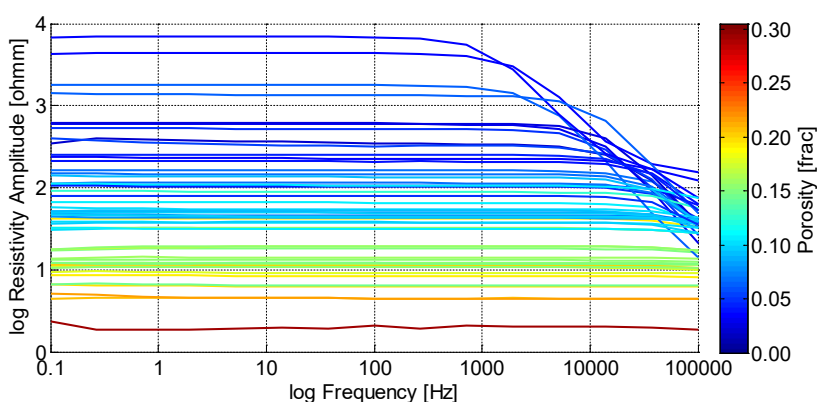
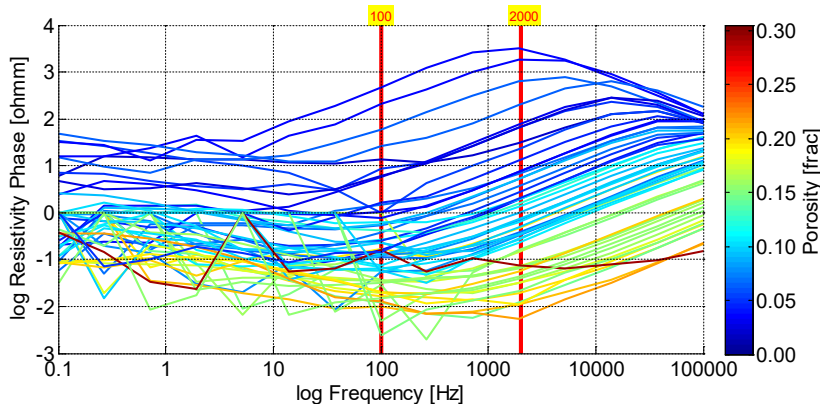


Figure 3.10: Top: Amplitude of resistivity as function of frequency of 54 dolomite samples at 20 MPa effective pressure, color-coded with porosity. Higher porosity samples show lower amplitudes. Bottom:



Phase shift of resistivity as function of frequency. Higher porosity samples show lower phase shifts. The characteristic dispersion of resistivity phase shift occurs between 100 – 2,000 Hz (frequency range indicated by vertical red lines).

The variations in the phase shift measurements is generally large at low frequencies <10 Hz. This could either be a real effect of the pore structure, or, more likely, due to effects of electrode polarization and other parasitic impedances from the measurement setup.

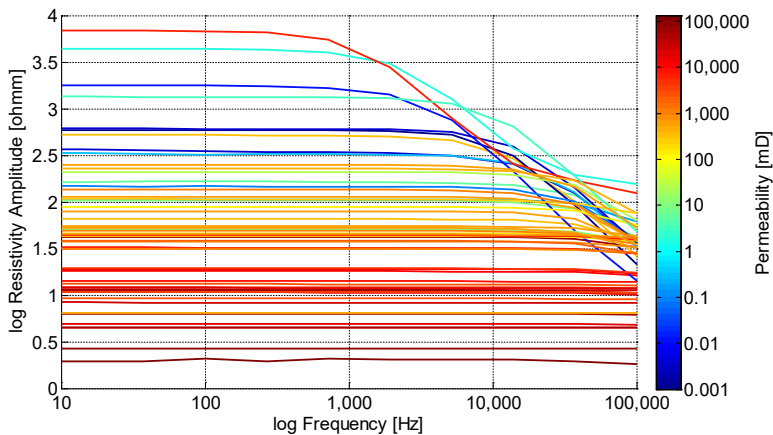
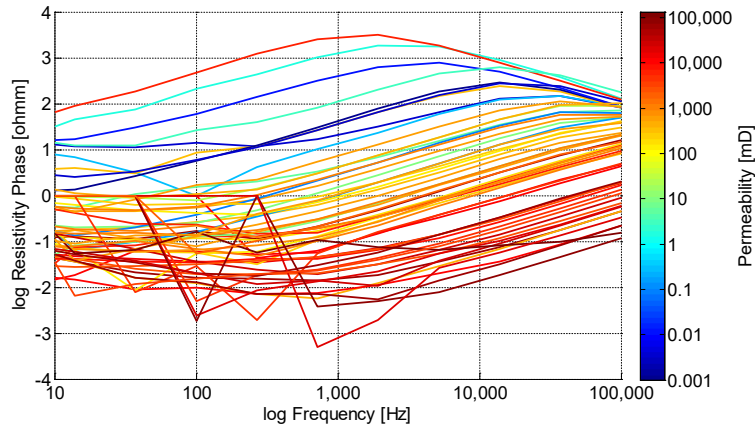


Figure 3.11: Top: *Amplitude of resistivity as function of frequency of 54 dolomite samples at 20 MPa effective pressure, color-coded with permeability. Higher permeability samples show lower*



*amplitudes. Bottom:
Phase shift of
resistivity as
function of
frequency. Higher
permeability
samples show lower
phase shifts.
Frequency range
<10 Hz omitted.*

The 100 – 2,000 Hz range of the phase shift produces a reliable record of the dispersion and thus is hitherto used for the correlation between resistivity and other physical properties (Figure 3.10; bottom). In this frequency range there is a strong correlation of the mean slope β of the phase shift dispersion with the porosity and also permeability of the sample (Figure 3.11; bottom).

Tong and Tao (2008) found a similar trend for shaly sandstones and used the phase shift to estimate permeability. Here, their empirical model is modified to include the slope β together with porosity and cementation factor m for permeability predictions:

$$K_{\text{estimated}} = a\Phi^b\beta_{\text{phase}}^c m^d \quad \text{Eq. 3.1}$$

Unconstrained nonlinear optimization for constants a , b , c , and d of (Eq. 3.1) yields:

$$K_{\text{estimated}} = 436\Phi^{2.45}\beta_{\text{phase}}^{-0.63}m^{2.05} \quad \text{Eq. 3.2}$$

We use above equation (Eq. 3.2) to estimate plug permeability with a correlation coefficient of $R^2 = 0.82$ between plug-measured and predicted permeability (Figure 3.12). The high correlation coefficient positively emphasizes the strong correlation between low-frequency phase shift phenomena and the effective hydraulic length scale of the sample (Zisser et al., 2010).

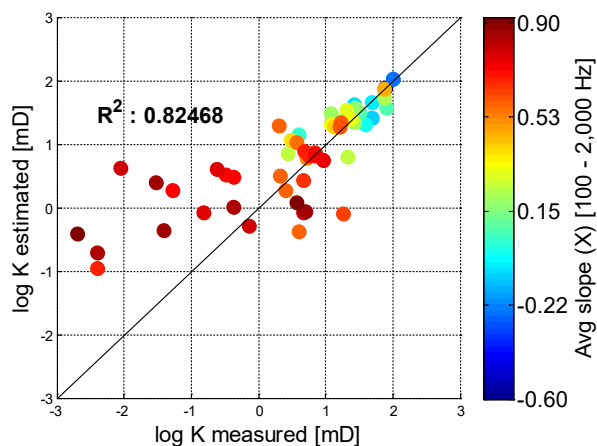


Figure 3.12: Cross-plot of measured permeability vs. estimated permeability from the model (Eq. 3.2). Slope of phase shift dispersion β in color. Lower slope β observed in higher permeability samples. The solid line is the identity function $K_{measured} = K_{estimated}$.

Discussion

Crystal size and Pore Structure

Previous authors (Lucia, 1995; Braithwaite et al., 2004) often assumed that crystal size controls petrophysical properties in dolomites, similar to grain size does in siliciclastics. Our dataset however shows no such trends. Neither permeability nor acoustic properties of the samples correlate with crystal size, but are mostly controlled by the total porosity (Figure 3.6). The exception being that samples with large crystal sizes do not show low velocities. The general lack of influence of crystal size on sonic properties can be explained by the anhedral crystal shapes in many samples. Partial dissolution and re-precipitation forms strong connections between crystals, making the rock stiffer and faster without increasing the crystal size. Often the crystals even decrease in size and show rounded edges. The lack of correlation of crystal size with permeability in this data set is most likely the result of the dolomitization mostly affecting the rock matrix microporosity without altering the larger scale macropore structure that controls permeability. Hence, permeability is still mostly controlled by the heterogeneous, pre-dolomitization carbonate pore structure.

However, the weak link of pore geometries to flow properties in low-porosity samples suggests a cut-off for the thin-section DIA method at 10% porosity. This also emphasizes

that future pore structural analyses in tight samples have to incorporate higher resolution imaging techniques.

Cementation factor m and pressure dependency

In carbonates, higher cementation factors are related to larger and simpler pore structures with higher permeability (Verwer et al., 2011). In siliciclastics, cementation factors truly are a measure of cementation of the pore structure, and higher cementation means lower permeability. In our dataset, cementation factors do not show a correlation with permeability (Figure 3.7). This sets them apart from both, other carbonates and siliciclastics, and makes the electrical resistivity behavior of these dolomites quite unique. This behavior could be the result of the dolomites having a hybrid pore structure with traits from both carbonates and siliciclastics. They mostly consist of grains (crystals) like siliciclastics, and pore structures are generally simpler than in carbonates due to the crystalline overprint. However, they are prone to diagenetic effects, altering and occluding the pore space like in heterogeneous carbonates.

Cementation factors in this dolomite dataset are on average 2.4. Obviously crystalline, dolomite micro-structures are not as favorable for conduction of electrical charge as similarly crystalline mudstones that consist of microspar crystals (Loucks et al., 2013). This is most likely due to the larger crystal size and the more angular crystal shape of the dolomites. The larger size results in less pore connections and more dead-end pore space between impinging dolomite rhombs. The dead-end pore space does not contribute to the transport of electrical charge between entrance- and exit-throat of the pore. Mudstones, on the other hand, consist of smaller microspar crystals that are more equant and cubic. The smaller, more cubic shape of their crystals leaves more of the pore space for effective

electric conduction and also provides more pore connections, resulting in higher apparent cross-sectional area (Adisoemarta et al., 2001) and lower cementation factors.

Furthermore, the dolomitization caused the samples to be very pressure-resistant and retain their micropore network even at high effective pressures up to 20 MPa (approximately equivalent to 1 km overburden). This is the reason why dolomites often are excellent reservoir rocks until great burial depth. It is especially important for this dataset as the Madison Formation reservoirs in Wyoming are incredibly deep – up to 7.5 km (25,000 feet). The small hysteresis effects encountered in this dataset further underline the usability of core plug resistivity measurements for well log calibration in dolomite rocks.

Complex resistivity spectra (CRS)

Frequency dependent complex resistivity measurements are a powerful tool since the measured spectra are sensitive to surface chemical and pore geometrical properties of a medium. Since the analyzed samples are all dolomites, effects of differing surface chemistry can be precluded, leaving the pore geometry as the main influencing factor.

A porous medium exposed to an alternating current acts as a dielectric and will show a phase shift in the voltage signal measured across it when compared to the input current signal that it is exposed to. The magnitude in the phase shift is a result of the magnitude of polarization.

In this dataset it is apparent that the more resistive the medium and the lower its porosity, the greater is the magnitude of polarization. This manifests itself in larger and earlier phase shifts between the induced voltage and resulting current signals (Figure 3.9; bottom). However, the phase shifts peak at a certain frequency, which is dependent on the porosity of the sample, and start declining. This peak in resistivity phase shift appears to

coincide with a decline in resistivity amplitudes, which show little variations at lower frequencies (Figure 3.9; top). It seems that at higher frequencies the increase in conductivity (lower resistivity) goes along with an increase in permittivity (lower phase shifts).

Well-logging applications

The direct link between the spectral behavior of the phase shift of complex resistivity and the porosity of the sample indicates that spectral induced complex resistivity measurements could enhance down-hole porosity and also permeability estimates. Development of a new tool that measures low-frequency phase shift spectra as part of a logging suite could greatly enhance reservoir characterization.

Currently there is a new dielectric logging tool being deployed that measures at multiple frequencies (Hizem et al., 2008). The new dielectric dispersion logging tool improves on older versions by being mounted on an articulating pad that can account for borehole rugosity, which enables more accurate, salinity-independent estimates of formation mineralogy and water salinity, content, and movability (Hizem et al., 2008; Mosse et al., 2009; Seleznev et al., 2011; Bean et al., 2013). However, the tool measures only in the high-frequency range of 20 MHz to 1 GHz, where molecular and electronic polarization effects dominate the dielectric permittivity response, hence the new tool is insensitive to interfacial polarization effects.

In the low-frequency range, where induction logs operate, there is no current logging tool that measures at multiple (more than two) frequencies. Chemali et al. (1995) first report the dispersion phenomenon from logging tools by analyzing differences of resistivity measurements from wireline induction and LWD propagation tools operating at

frequencies of 20 kHz and 2 MHz, respectively. Anderson et al. (2008) show a new method of logging inversion that links high dielectric constants from induction logs at 26 kHz and 52 kHz to elevated pyrite and graphite content in gas shales. Wang & Poppitt (2013) show a combination of existing wireline tools operating at different frequencies to analyze the broadband electromagnetic dispersion in shales.

Given the direct relationship of permeability with CRS from core plug measurements in this and previous studies (e.g. Tong & Tao, 2008; Weller et al., 2010) and the general higher susceptibility of dielectric permittivity on interfacial polarization at low frequencies (Bean et al., 2013, Fig.1), the development of a low-frequency wireline tool that can measure dielectric permittivity spectra (CRS) at frequencies between 100 and 100,000 Hz would permit a better assessment of permeability from resistivity. The development is an engineering challenge as it would require implementation of multiple transmitter-receiver spacings in order to measure resistivity at different frequencies for the same depth of investigation.

Field tests performed in small boreholes demonstrate the general applicability of the low-frequency complex electrical resistivity measurements in a well logging scenario (Weller & Börner, 1996). The general idea is that low permittivity and its dispersion is caused by increased polarization effects resulting from higher specific surface area, which are directly negatively correlated to permeability. Hence, a tool measuring CRS could be used to estimate permeability, which is a major problem in heterogeneous carbonates with their complex relationships of electrical, sonic, and pore structural parameters (Weger et al., 2009; Verwer et al., 2011; Norbistrath et al., 2014).

Conclusions and Implications

A dataset of 54 dolomite core plugs from the Mississippian Madison Formation has been investigated on relationships of their low-frequency complex electrical resistivity spectra with their petrophysical and their pore structural properties, quantified with digital image analysis on thin-sections.

Pore structural parameters PoA and DOMsize and the slope D of the fractal pore size distribution indicate that in dolomites like in other carbonates, smaller and more intricate pore networks enhance electrical flow.

There is a minimal influence of pressure to resistivity. This small pressure dependency and hysteresis effects of measured cementation exponents underlines the applicability of core plug measurements for well log calibration in dolomite rocks.

The fractal scaling of the pore space potentially helps to upscale or populate a reservoir model with pore geometries that have been acquired at different scales, e.g. from core plugs to seismic surveys. It also has to be considered when modeling pore geometries in flow simulations. Future work regarding pore size distributions should include a multiscale analysis, possibly from plug-scale over core-scale to log-scale, in order to establish scaling parameters across different measures. This would also clarify if the pore size distributions could universally be modeled from their fractal dimension measured at a certain scale.

Furthermore, complex electrical resistivity spectra between 0.1 - 100,000 Hz show a strong frequency dispersion. This frequency dispersion, together with porosity, has been used to model permeability with a correlation coefficient of $R^2 = 0.82$. However, porosity alone already shows good correlation with permeability in the investigated dolomite dataset. Nevertheless, the dispersive behavior of resistivity between 100 – 100,000 Hz in

sucrosic dolomites is directly related to the porosity of the sample. If above relationship of permeability with low-frequency complex resistivity dispersion holds true in heterogeneous carbonates (work in progress), it would be logical to use the new insights in a wireline application. As current tools already incorporate multiple receiver and transmitter spacing for invasion profiling, it might even be possible to modify existing wireline resistivity tools. If these tools could be modified to measure resistivity at different frequencies for the same depth of investigation, it could establish an alternative method for down-hole porosity and permeability estimates.

Chapter 4: Complex Resistivity Spectra and Pore Geometry for Predictions of Reservoir Properties in Carbonate Rocks

Summary

Measurements of complex resistivity spectra (CRS) are performed on core plugs from a wide variety of carbonates in a log sweep from 0.1 – 100,000 Hz inside a pressurized chamber at varying effective pressures up to 20 MPa. We quantify the CRS curves by extracting the slope of both real and imaginary part of complex resistivity in the 10,000 – 100,000 Hz range. Pore geometries are quantified with thin-section digital image analysis (DIA) from optical light microscopy. The dataset includes 330 carbonate core plug samples from twelve different study areas and hence includes a highly diverse range of carbonate rock types. This should make our results applicable to most carbonate rocks.

Pore geometry parameters derived from DIA, such as Dominant Pore Size (DOMsize) and Perimeter over Area (PoA), correlate well with petrophysical properties such as cementation factor and permeability. However, when modeling those properties, higher correlation coefficients are achieved with CRS than with DIA parameters. Using CRS and model constants tuned to the sub-datasets, cementation exponents are predicted with $R^2 = 0.91$ and permeability with $R^2 = 0.84$. The correlation coefficient of a universal equation for all 330 samples is still high for cementation factors with $R^2 = 0.80$, but less for permeability with $R^2 = 0.48$.

The results show that CRS in carbonates are directly related to permeability and formation factors, and greatly improve reservoir property estimates. This study also highlights the usability of low-frequency CRS data as a measure of flow and storage properties in carbonate rocks. The transfer of this methodology to wireline applications

would result in more accurate and continuous permeability and cementation factor predictions from well logs.

Introductory Remarks

Carbonate reservoirs contain up to 60 % of conventional oil resources, but the production from these reservoirs is often complicated due to heterogeneity of pore structure and related flow properties (Garing et al., 2014; Skalinski & Kenter, 2015). Classifying the pore structure in conjunction with grain/crystal size or texture is a common approach when relating carbonates to petrophysical properties (Choquette and Pray, 1970; Lucia, 1995; Ahr et al., 2005; Lonoy, 2006). Attempts to relate quantitative pore shape parameters, derived from digital image analysis (DIA), to physical properties produced new insights into how pore structure influences these properties (Anselmetti et al. 1998; Weger, 2006). For example, Weger et al., (2009) show how large pores and simple pore networks result in higher velocities, while Verwer et al. (2011) document how simple and large pores result in higher cementation exponents in carbonates and how a large number of small pores can reduce resistivity. Likewise, microporosity has a large influence on velocity (Baechle et al., 2008) and electrical properties show distinct relationships depending on the amount and type of microporosity (Dixon & Marek, 1990; Ahr et al., 2005; Norbistrath et al., 2015).

Complex electrical resistivity has a long history of use in the mineral exploration industry, but failed to get the attention it deserves in the petroleum industry (Snyder et al., 1977). Worthington & Collar (1984) show the relationship between polarization and permeability and shaliness in reservoir rocks. Chemali et al. (1995) report the frequency dispersion of different frequency measurements of resistivity from wireline and logging-while-drilling (LWD) tools.

This study describes an approach to predict core plug permeability and cementation exponents from either resistivity or porosity and complex resistivity spectra (CRS). For comparison we show predictions where CRS parameters are interchanged with pore geometry parameters DOMsize and PoA from DIA. The new approach to estimate flow and storage properties of core plugs from CRS described in this paper is based on a previous model by Tong & Tao (2008). The approach has proven its application within a rather homogeneous dolomite dataset (Norbisrath et al., in press). Here we are testing it on a wide variety of very heterogeneous carbonate rocks from multiple datasets. To encompass carbonate heterogeneity we investigate samples from twelve independent and highly diverse datasets from both outcrop and subsurface, including several modern microbialites.

When measuring complex resistivity, different polarization effects result in phase and amplitude shifts between input voltage and output current signal. In this study, we measure the low-frequency phase shift and amplitude spectra that are mostly induced by pore structure. Shape parameters of these complex resistivity spectra (CRS) are then used to predict measured petrophysical parameters. The goal is to find fundamental relationships between petrophysical, pore structural, and dielectric properties that can be used in future applications. Since this study contains a large variety of rock types, the results should be universally applicable to most carbonate rocks.

Complex electrical resistivity and dielectric dispersion

Insulators often show dielectric properties, where the application of a voltage separates charge centers and charge is stored in an electric dipole. The insulators in this study are brine-saturated carbonate core plug samples. Carbonate minerals like calcite, aragonite, and dolomite by themselves can be seen as perfect electrical insulators, as they do not

conduct electrical charge. It is the brine in the pore system of natural carbonate rocks that allows for polarization effects to occur. These dielectric phenomena show a strong variation with the frequency of the applied voltage, i.e. a frequency dispersion of the strength of the charge separation based on how fast the AC electric field is reversed (Figure 4.1).


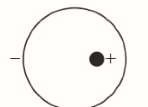
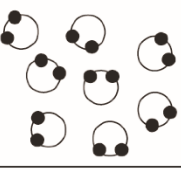
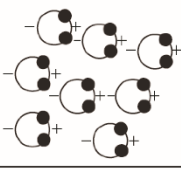

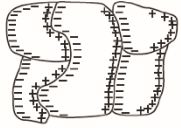
Polarization Type	No field $E = 0$	Applied electric field $E \rightarrow$
Electronic ~ THz Atomic scale		
Molecular ~ GHz - MHz Molecular scale		
Interfacial ~ KHz Pore scale		

Figure 4.1: Polarization effects at different frequency ranges and length scales (modified from Ellis & Singer, 2007). Interfacial polarization controls low-frequency range (kHz) dispersion effects on a pore scale. These effects are exploited in this study.

This frequency-dependency is related to the ability of the polarizing mechanism to keep up with the alternating field direction. All motions, including dipole motions, have a certain inertia. Additionally, different electric dipoles (atomic, molecular, and interfacial) have different relaxation frequencies. Above a certain frequency the oscillatory motion of the dipole in the alternating electric field is damped. It is evident that small-scale movements like the shift of an electron cloud (atomic polarization) require less time than the physical shift of cations from one pore wall to the opposing pore wall within the pore system (interfacial polarization). Hence, the different mechanisms are only effective at certain frequency ranges, where their charge movement can keep up with the change of the applied

electric field. Mechanisms with high inertia (molecular and interfacial) will not be active above a certain frequency threshold.

At high frequencies (THz range), the charge separation is induced by atomic polarization (i.e. preferential orientation of the electron cloud of an atom). At intermediate frequencies (GHz to MHz range), molecular polarization is the driving force (e.g. the orientation of water molecules in the pore system). At low frequencies (kHz range), the charge separation is mostly due to interfacial polarization at the fluid-grain interface that consists of preferential spatial accumulation of charged cations within the confinements of the pore structure. This interfacial polarization is also known as the Maxwell-Wagner effect (Wagner, 1914). It is a strong function of the pore structure of the rock, including texture, connectivity, and clay content in shale (Wang & Poppitt, 2013).

Methods

Porosity and permeability

All measurements are performed on 1-inch or 1.5-inch diameter core plugs. Plug porosity is measured with helium pycnometry utilizing Boyle's law by subtracting the true pycnometer grain volume from the bulk volume determined by caliper measurements of the outside dimensions of the plug. Plug permeability is determined externally with industry-standard Klinkenberg-corrected gas permeability measurements.

Pore geometry (PoA, DOMsize, Slope D)

Analysis and quantification of pore geometry is performed on blue epoxy dyed thin-sections. Thin-section images are stitched, segmented, and parameterized in an automated Matlab environment with the digital image analysis (DIA) methodology from Weger et al. (2006, 2009). Main output variables are Dominant Pore Size (DOMsize) and Perimeter

over Area (PoA). DOMsize is the upper boundary of pore sizes of which 50% of the porosity on a thin section is composed. The parameter gives a good indication of the overall pore network size. PoA is the ratio of the sum of the perimeter of all pores identified on a cross-section and the sum of the area of these pores. The parameter describes the complexity of the pore network. Both parameters describe important aspects of the pore geometry of a sample with a single number, which allows large datasets to be compared and trends to be recognized.

Pore size distributions are analyzed by distributing all pores identified from DIA into non-linear bins according to their pore size. Consequent bins always double in bin width. Pore size frequencies are then normalized by analyzed area and bin width, and results plotted against bin centers on a double logarithmic scale (Klaver et al., 2012; Houben et al., 2013; Hemes et al., 2015). Least square linear regression analysis is used to quantify the power law exponent or slope of the pore size distributions:

$$\text{Slope D} = - \frac{\log\left(\frac{\text{Pore size frequency}}{\text{Analyzed area} * \text{Bin width}}\right)}{\log(\text{Pore size})} \quad \text{Eq. 4.1}$$

The negative value of the slope ($D = - \text{slope}$) thereby represents the fractal dimension of the pore space (Mandelbrot, 1967); it is referred to as Slope D hereafter.

Complex resistivity spectra

Resistivity measurements are performed in a log sweep from 0.1 – 100,000 Hz on 35 ppt NaCl brine-saturated core plugs inside a pressure chamber to simulate subsurface conditions. The pore pressure (PP) is held at a constant 3 MPa while confining pressures (CP) are varied from 5 to 23 MPa for effective pressures (EP) of 2 – 20 MPa ($EP = CP - PP$). Some more fragile samples have only been measured at up to 10 MPa EP or broke at higher EP. For consistency, 10 MPa measurements of pore fluid temperature corrected

(Arps, 1953) resistivity amplitude values at 720 Hz are used for calculations of cementation exponents in all samples with Archie's (1942) empirical formula:

$$FF = \frac{R_f}{R_w} = \Phi^{-m} \quad \text{Eq. 4.2}$$

where FF is the formation factor, R_f is the measured resistivity at 720 Hz and 100% water saturation, R_w is the resistivity of the saturating fluid, Φ is the porosity, and m is the cementation exponent.

Plug-diameter silver membrane filters ensure contact between plug and current electrodes of the core plug holder while still allowing fluid flow. Silver filters are used as they have shown the least electrode impedance. A true 4-electrode setup is achieved by separating the voltage contacts from the current electrode silver filters with polyester felt. This way, voltage measurements can be made without the influence of electrochemical reactions at the current electrodes. The four-electrode measurement technique also has the advantage of eliminating contact impedances due to the small current drawn by the voltmeter (Garrouch & Sharma, 1992). In our measurement setup, the reference resistor is in series with the sample. Two input amplifiers measure the voltage across the reference resistor and across the sample, and a digital oscilloscope records these signals. The phase shift and amplitude ratio between the two signals is used to measure the complex electrical impedance (Z^*) of the sample,

$$Z^* = R - iX \quad \text{Eq. 4.3}$$

where R is the resistance and iX the reactance (Knight & Nur, 1987). To analyze the frequency dispersion of complex resistivity, amplitude and phase shift are measured across the frequency range from 0.1 – 100,000 Hz. The resulting CRS curves show most reliable data and highest variability in amplitude and phase shift between 10,000 – 100,000 Hz.

Therefore, we use this range to define the frequency dispersion of the individual samples by fitting a linear equation to both amplitude and phase shift dispersion curves (Figure 4.2).

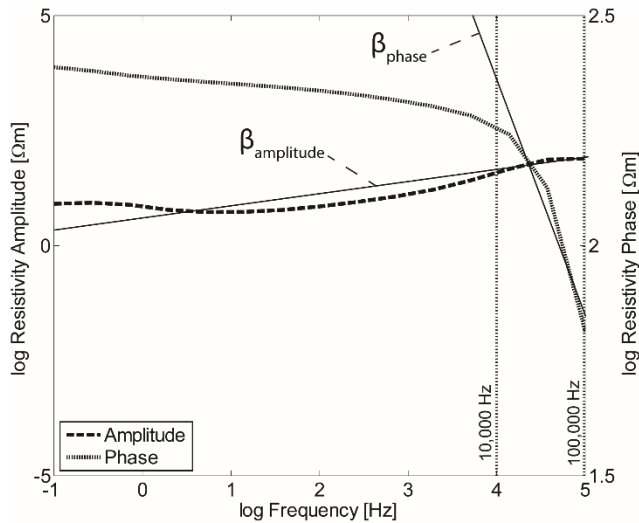


Figure 4.2: Example of amplitude and phase shift curves of complex resistivity for a single sample. Vertical dotted lines at 10,000 and 100,000 Hz indicate fitting range for extraction of slopes $\beta_{\text{amplitude}}$ and β_{phase} .

The fitting is performed for each individual measurement at all pressure steps experienced by a sample. Resulting slopes are subsequently averaged to minimize potential bias of individual measurements. For quality control of CRS, 113 samples with standard deviation of more than 0.1 between slopes at individual pressure steps are excluded (217 samples left). Since slopes can show errors and high variance even when their average is around zero, no quality control approach based on percentages could be chosen. The averaged slopes $\beta_{\text{amplitude}}$ and β_{phase} of the CRS curves are then used as input for predictions of reservoir properties like permeability and cementation exponents.

Parameter predictions

Based on a previous model by Tong & Tao (2008):

$$K = a\Phi^B\beta_{\text{phase}}^c \quad \text{Eq. 4.4}$$

we show a new approach to predict 1) permeability (K) from CRS slopes and resistivity, and 2) cementation exponent (m) from CRS slopes and porosity. For comparison we show predictions where CRS are interchanged with pore geometry parameters from digital image analysis. The constants a , b , c , and d in these new models are determined with unconstrained nonlinear optimization (Nelder & Mead, 1965). In this optimization no boundary conditions are set when trying to minimize the error between input and output value.

The error minimization is first performed on each of the twelve datasets individually, whereby the constants $abcd$ can be tuned to each dataset, and the output is combined afterwards. This involves twelve different sets of $abcd$ parameters. Consequently, a relatively high correlation coefficient between input and estimated output values is expected. In a second step, error minimization is done for the entire dataset, where constants $abcd$ have to account for the heterogeneity of the entire dataset. This involves only one set of $abcd$ parameters. Thus, a lesser correlation is expected. The equations are shown in the individual results sections for predictions from DIA and CRS, respectively. It has to be emphasized that the constants $abcd$ are different for each of these equations and also within each individual dataset. Due to space restrictions we do not show all 52 equations.

Dataset

The dataset includes 330 carbonate core plug samples from the data base of the CSL – Center for Carbonate Research at the University of Miami. Samples are from twelve separate studies and study areas and include a very diverse range of carbonate rock types.

Sample rock types cover the entire Dunham (1962) spectrum in texture (mudstone, wackestone, packstone, grainstone, boundstone, and crystalline dolomite) and pore types (Choquette and Pray, 1970) and include a wide variety of microbialite boundstones like stromatolite, tufa, and travertine. Microbialite reservoirs can often be found at great burial depths and below thick salt layers, which makes development of such fields even more challenging (Machado et al., 2011; Rezende et al., 2013). Consequently, efficient production from these deep formations requires as much information as possible about their reservoir quality, preferably without the need for expensive coring. The large variety of samples encompasses most carbonate pore types and ensures the applicability of the results from this study to a wide range of carbonate rocks.

Results

Porosity, permeability, and cementation factor m

Porosity ranges from 1.1 – 49.2 % and permeability from 0.001 – 47,598 md in our dataset (Figure 4.3; left). This extreme range in both porosity and permeability reflects the wide variety of carbonates in the dataset. The weak correlation between porosity and permeability of $R^2 = 0.39$ illustrates the issues when trying to predict permeability from porosity, and emphasizes the discrepancy between flow and storage properties in carbonate rocks.

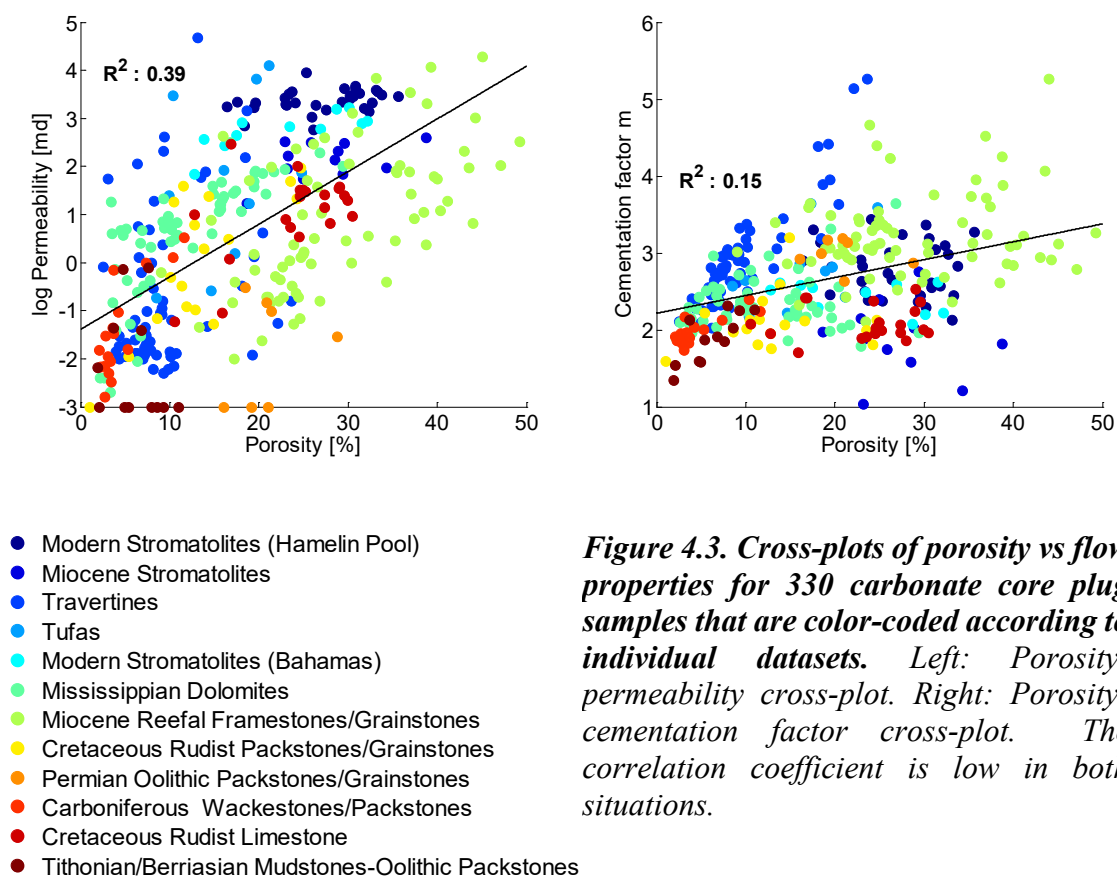


Figure 4.3. Cross-plots of porosity vs flow properties for 330 carbonate core plug samples that are color-coded according to individual datasets. Left: Porosity-permeability cross-plot. Right: Porosity-cementation factor cross-plot. The correlation coefficient is low in both situations.

Cementation factors range from $m = 1.03 - 5.27$ (Figure 4.3; right). This wide range of the cementation exponent m is characteristic for carbonate rocks (Glover, 2009; Verwer et al., 2011). The weak correlation of $R^2 = 0.15$ between porosity and cementation exponents illustrates the difficulty relating porosity alone to other petrophysical properties in carbonates.

There is a large variability in porosity within most sub-datasets. Reefal grainstones and stromatolites show the highest porosity values, mudstones and wackestones the lowest. Travertines, dolomites, and Cretaceous rudist wackestones and grainstones can also show very low porosities.

Permeability values are highest in stromatolites, tufas, and Cretaceous reefal grainstones. While most datasets contain low-permeability samples (< 0.01 md), stromatolite datasets do not contain samples with permeability lower than 17 md (Figure 4.3).

Cementation factors again show high variability within each sub-set. Highest m -values can be found in travertines and reefal grainstones; the lowest in mudstones, wackestones, and, surprisingly, Mallorca stromatolites.

PoA and DOMsize

The pore structure is assessed with DIA following the protocol described by Weger (2006). The quantitative pore structure parameter Perimeter of Area (PoA) is a measure of how complicated/intricate the pore system is, while the Dominant Pore Size (DOMsize) describes the size of the pores (Weger et al., 2009). PoA ranges from 8 - 328 mm^{-1} and the DOMsize from 8 - 3099 μm in the entire dataset. The wide spread of these parameters underlines the variety of pore types in carbonates. The individual sub-sets display less variability of pore structure, as they tend to plot in a certain area of the PoA-DOMsize cross-plot (Figure 4.4). This reduced variability within the individual sub-datasets will be important when modeling reservoir properties.

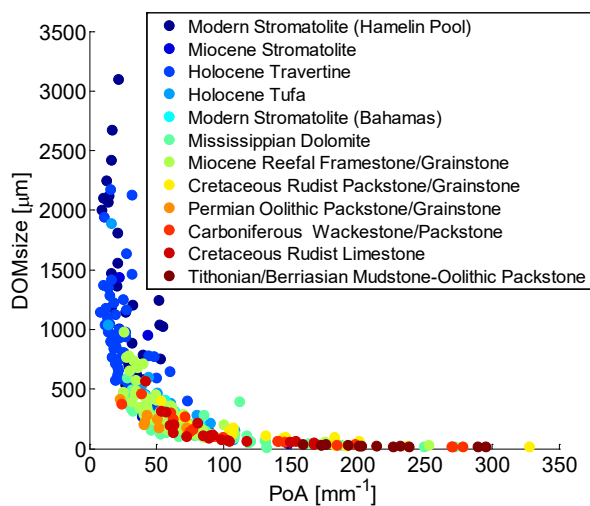


Figure 4.4: Scatterplot of Perimeter over Area (PoA) versus Dominant Pore Size (DOMsize) for the individual datasets that have been combined for this study. Plot illustrates the extreme variability of pore geometry in the combined dataset, with individual datasets being less variable.

Stromatolites, travertines, and tufas show the highest pore sizes and least complex pores (high DOMsize, low PoA), while wackestones, packstones, and mudstones show the smallest pore sizes with highest complexity (low DOMsize, high PoA).

When looking at the dataset as a whole, it is apparent that pore geometry parameters DOMsize and PoA are closely linked to both permeability (Figure 4.5; left) and cementation exponents (Figure 4.5; right).

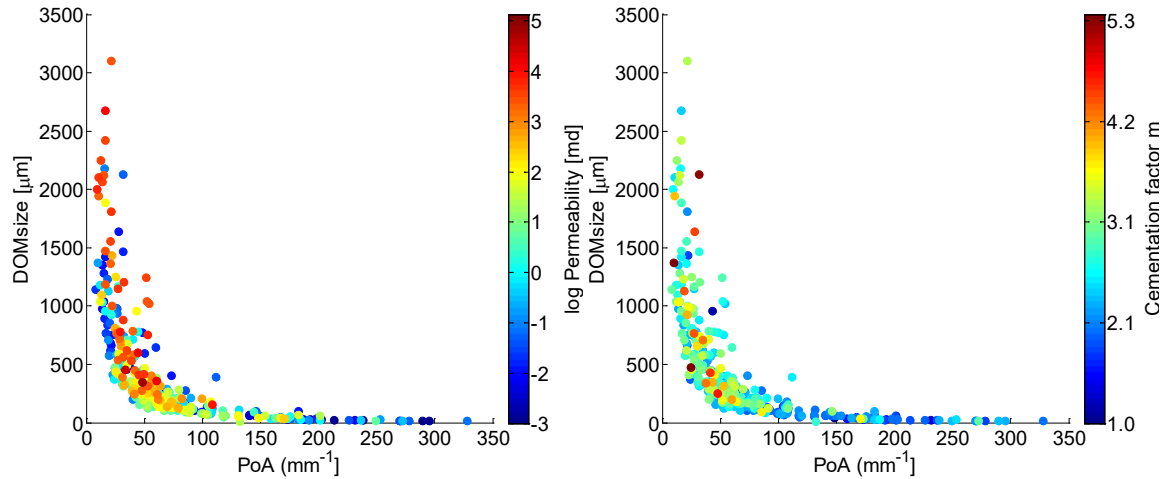


Figure 4.5: Cross-plots of Perimeter over Area (PoA) vs. Dominant Pore Size (DOMsize), color-coded with permeability (left) and cementation factor m (right). Both permeability and cementation exponents are higher in the samples with higher DOMsize and lower PoA (large and simple pores).

As a general trend large and simple pore structures (high DOMsize, low PoA) result in higher values of both permeability and cementation exponents. However, there are significant outliers with low permeability or low cementation factors and large and simple pore structures. This can be attributed to samples with unconnected, vuggy pores (e.g. rudist limestones) or layered pore structures (e.g. travertines and tufas), which are characterized by anisotropy in pore structure and resulting petrophysical properties.

Slope D

All 330 carbonate samples show power law distributions of pore sizes across the investigated length scales (30 μm thin-section thickness up to thin-section size ~ 2.5 cm²) as indicated by the good fit of a log-log linear regression curve to the data points. The fractal dimension of the sample is the Slope D of its power law distribution. A shallow Slope D is produced by simple pore geometries and hence higher permeabilities (Figure 4.6; top). Similar trends can be seen when relating pore size distributions to cementation

factors. Shallower Slope D and less complex pore structure results in higher cementation factors (Figure 4.6; bottom).

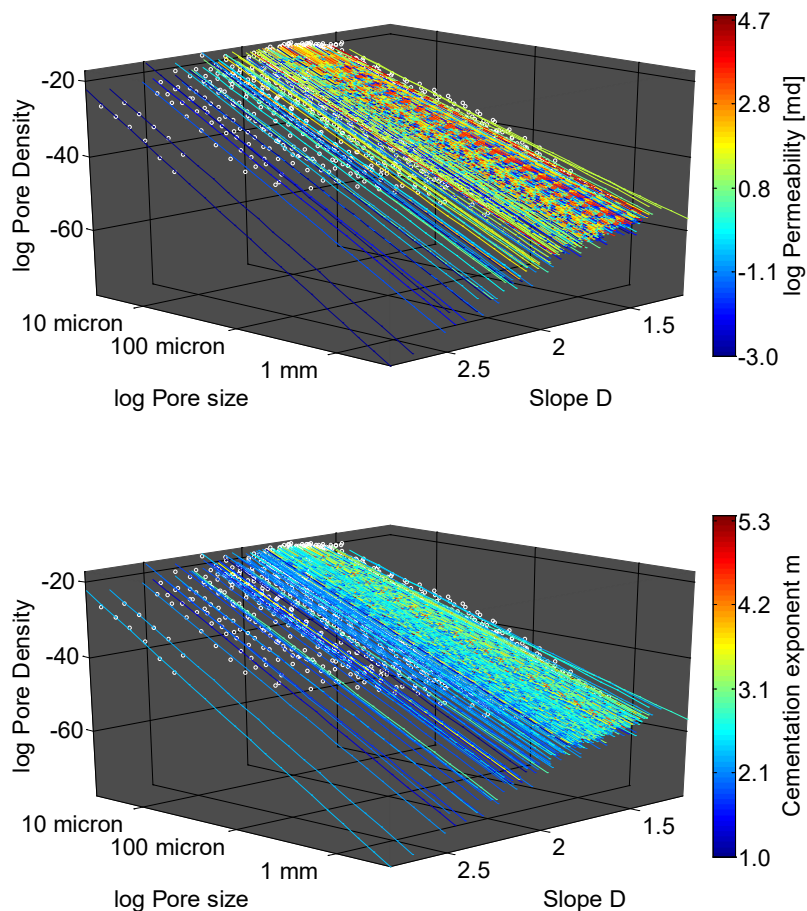


Figure 4.6: Pore size distributions of 330 carbonate samples acquired with digital image analysis on thin-sections, plotted on log-log scale using non-linear binning in order of their Slope D. Log-log linear distribution indicates a power law distribution and fractal scaling. Color-coding displays the correlation between Slope D and permeability (top) and cementation factor (bottom).

Similar to PoA, Slope D values are highest in mudstones and lower in stromatolites, travertines, and tufas. Dolomites show high Slope D values, but also the lowest of the entire dataset, indicating a wide range from very simple to relatively complex pore structures in dolomites, possibly related to the precursor rock and extent of dolomitization.

Table 4.1 gives an overview of the ranges of petrophysical and pore geometry parameters within the individual datasets, as well as general information about locality, age, rock type, and the associated study:

Age	Rock type	Study	Phi [%]	K [md]	Cementation factor m	DOMsize [μm]	PoA [mm^{-1}]	Slope D
Holocene	Stromatolite (Hamelin Pool)	Karaca, 2015	16.4 - 35.7	577.69 - 8990.65	2.13 - 3.43	419.5 - 3099.4	9.3 - 54.3	1.5 - 1.8
Miocene	Stromatolite	Eberli et al., 2014	18.7 - 38.8	17.18 - 396.03	1.03 - 2.75	42.3 - 1435.1	22.3 - 148.1	1.5 - 2.1
Holocene	Travertine	Eberli et al., 2014	2.6 - 23.6	0.005 - 47598.00	1.90 - 5.26	139.1 - 2178.1	8.1 - 89.9	1.4 - 1.9
Holocene	Tufa	Eberli et al., 2014	8.5 - 24.8	0.18 - 12859.46	2.17 - 3.64	76.4 - 1889.4	13.9 - 108.4	1.5 - 1.9
Holocene	Stromatolite (Bahamas)	Eberli et al., 2015	12.8 - 32.2	70.04 - 1694.77	2.08 - 2.62	180.3 - 448.1	32.1 - 82.3	1.5 - 1.9
Mississippian	Crystalline Dolomite	Smith et al. 2004; Westphal et al., 2004; Norbistrath et al, in press	2.2 - 29.4	0.002 - 319.25	1.79 - 3.64	7.9 - 591.5	27.3 - 272.5	1.2 - 2.3
Miocene	Reefal Framestone and Grainstone	Ditya, 2012	9.0 - 49.2	0.01 - 19376.03	2.11 - 5.27	27.6 - 982.1	24.9 - 252.9	1.5 - 2.2
Cretaceous	Rudist Wackestone to Grainstone	Anselmetti et al., 1993	1.1 - 24.7	0.001 - 94.34	1.59 - 3.20	15.5 - 399.4	53.7 - 327.9	1.5 - 2.3
Permian	Oolitic Packstone and Grainstone		16.1 - 28.7	0.001 - 0.31	2.64 - 3.19	177.5 - 412.4	22.7 - 72.5	1.6 - 1.8
Carboniferous	Wackestone / Packstone		2.1 - 11.6	0.002 - 3.27	1.74 - 2.40	14.5 - 458.6	23.8 - 278.3	1.5 - 2.5
Cretaceous	Rudist Limestone, all textures	Weger et al., 2009	10.6 - 30.4	0.06 - 290.54	1.71 - 2.53	39.1 - 570.4	41.3 - 167.1	1.7 - 2.2
Tithonian-Berriasian	Mudstone to Oolitic Packstone	Zeller et al., 2013	1.9 - 11.0	0.001 - 0.78	1.34 - 2.32	13.7 - 36.2	159.2 - 295.5	2.1 - 2.8

Table 4.1: Information about locality, age, rock type, petrophysical parameters porosity, permeability, and cementation factor, and pore geometry parameters DOMsize (Dominant Pore Size), PoA (Perimeter over Area), and Slope D (slope of log-log power law pore size distribution) for the individual sub-datasets.

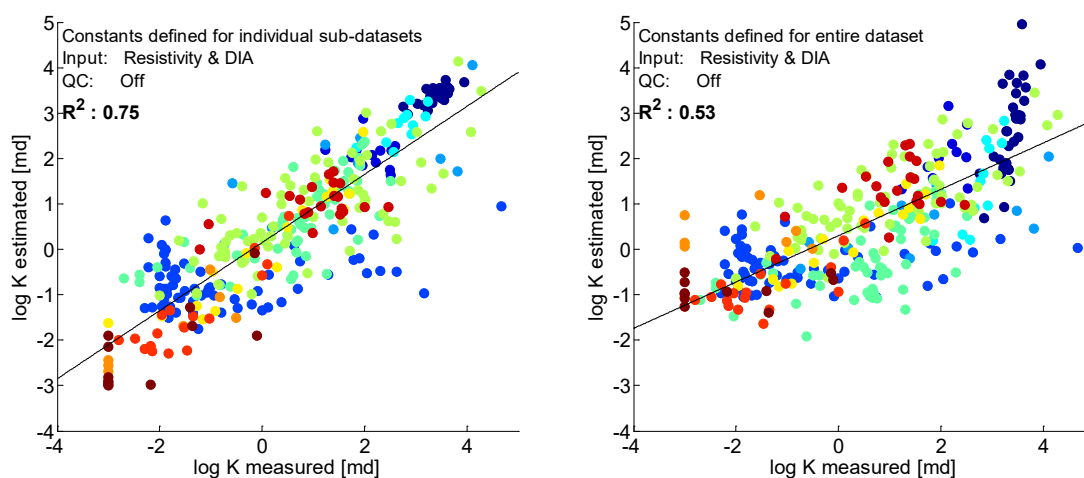
Predictions from DIA

DIA parameters DOMsize and PoA describe two aspects of the pore geometry that, in addition to porosity, are known to influence the petrophysical properties in carbonate rocks (Anselmetti et al., 1998; Eberli et al., 2003; Weger et al., 2009; Verwer et al., 2011; Norbistrath et al., 2015). Thus, predictions using these parameters should yield high correlation coefficients between measured and estimated values.

Permeability (K) is predicted using Equation 4.5 from both resistivity (Ω) and DIA parameters (DOMsize and PoA):

$$K_{\text{estimated}} = a\Omega^b \text{DOMsize}^c \text{PoA}^d \quad \text{Eq. 4.5}$$

The constants $abcd$ are first defined for each individual sub-dataset and subsequently for the entire data set. When constants $abcd$ are tuned to sub-datasets, the correlation coefficient for permeability predictions from DIA is $R^2 = 0.75$ (Figure 4.7; left), and when constants $abcd$ are tuned to the entire dataset it is $R^2 = 0.53$ (Figure 4.7; right).



- Modern Stromatolite (Hamelin Pool)
- Miocene Stromatolite
- Holocene Travertine
- Holocene Tufa
- Modern Stromatolite (Bahamas)
- Mississippian Dolomite
- Miocene Reefal Framestone/Grainstone
- Cretaceous Rudist Packstone/Grainstone
- Permian Oolithic Packstone/Grainstone
- Carboniferous Wackestone/Packstone
- Cretaceous Rudist Limestone
- Tithonian/Berriasian Mudstone-Oolithic Packstor

Figure 4.7: Permeability predictions from resistivity and DIA (Eq. 4.5) for entire dataset with constants $abcd$ defined for individual sub-datasets (left) and with constants $abcd$ defined for entire dataset (right).

Cementation factor (m) is predicted using Equation 4.6 from both porosity (ϕ) and DIA parameters (DOMsize and PoA).

$$m_{\text{estimated}} = a\phi^b \text{DOMsize}^c \text{PoA}^d \quad \text{Eq. 4.6}$$

When constants $abcd$ are tuned to the individual sub-datasets, the correlation coefficient for cementation factor predictions from DIA is $R^2 = 0.70$ (Figure 4.8; left). When $abcd$ are tuned to the entire dataset, the correlation coefficient is $R^2 = 0.33$ (Figure 4.8; right).

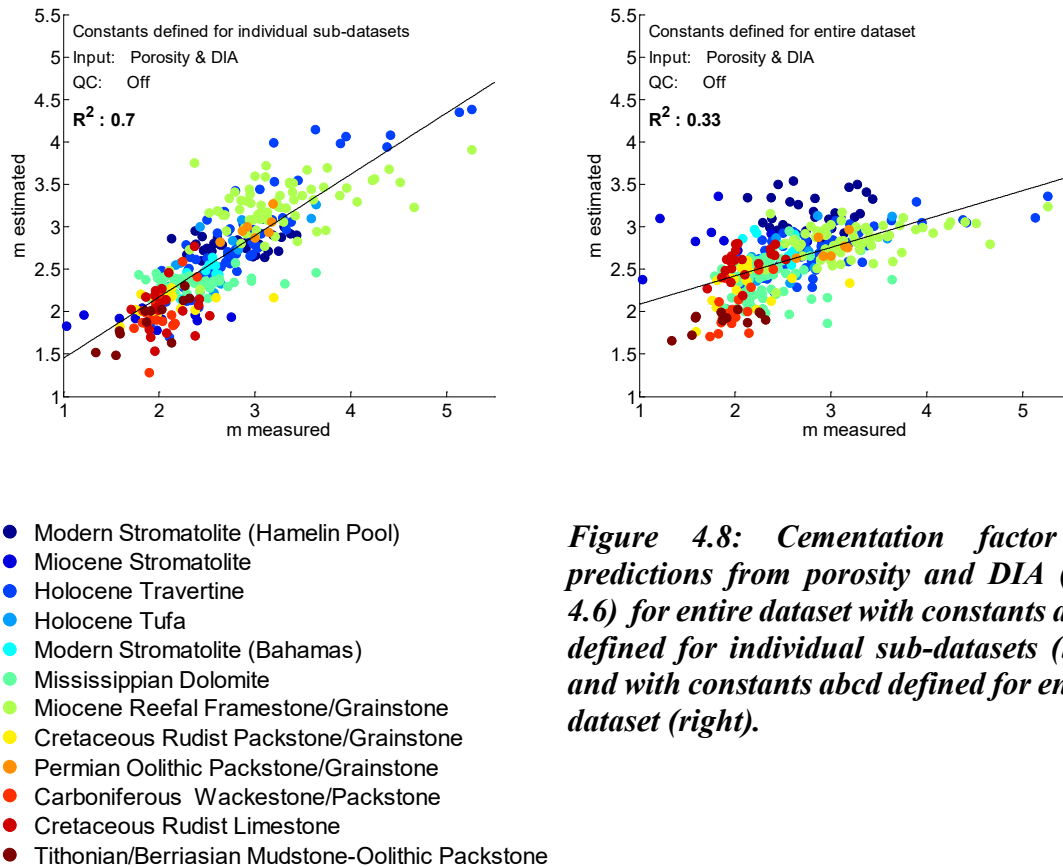


Figure 4.8: Cementation factor m predictions from porosity and DIA (Eq. 4.6) for entire dataset with constants $abcd$ defined for individual sub-datasets (left) and with constants $abcd$ defined for entire dataset (right).

Although for simplicity not further discussed here, the parameter Slope D can be used interchangeably for DOMsize or PoA in Equations 4.5 and 4.6, and achieves similar or better correlation coefficients (permeability predictions using Equation 4.5 with Slope D instead of PoA: $R^2 = 0.80$; cementation factor predictions using Equation 4.6 with Slope D instead of PoA: $R^2 = 0.71$).

Complex Resistivity Spectrum

The CRS show distinct behavior for samples with different permeability and formation factors (Figure 4.9). Generally, amplitude signals are often flat across the measurement range with drops above a certain frequency, whereas phase shift spectra show more variability. Most samples show distinct peaks or lows in the 100 – 10,000 Hz range. Samples with a flat amplitude signal (over the entire 10-100,000Hz range) and low phase shifts ($\log iX < 0$) display higher permeabilities (> 100 md) (Figure 4.9; left), indicating that a change in frequency influences the CRS less in samples with higher permeability. The characteristic CRS shapes allow the low- and high-permeability samples to be differentiated using frequency-dependent electrical measurements that ultimately enable our permeability predictions.

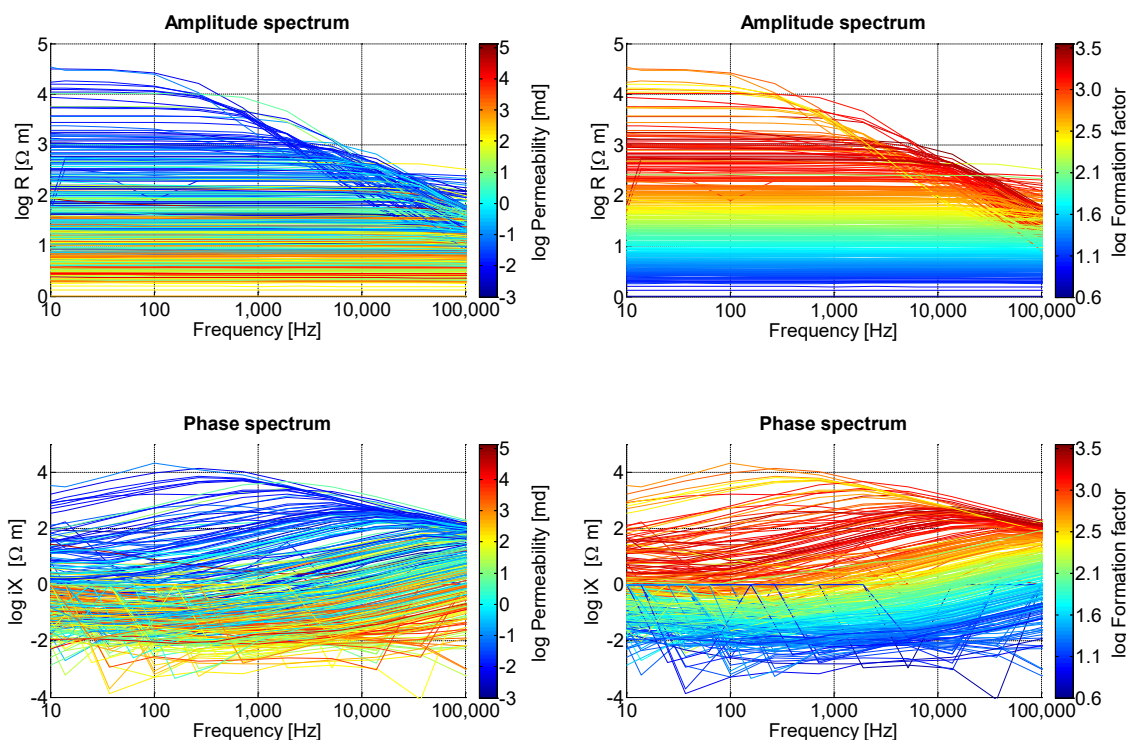


Figure 4.9: Complex resistivity amplitude (top) and phase spectra (bottom) of 330 carbonate plug samples, color-coded with permeability (left) and formation factors

(right). The amplitude curves (top) display less spikes and thus are more robust than the phase shift curves (bottom). Left: Samples with lower permeability show earlier drops in amplitude that coincide with phase shifts peaks. Right: Formation factors show excellent correlation with CRS curves. Samples with lower formation factors show flat amplitude curves and increase in phase shift towards higher frequencies.

Similar yet better defined trends exist for formation factors FF (Figure 4.9; right). The FF is the ratio of measured resistivity of the plug sample at 100 % water saturation over the resistivity of the saturating brine and is used to calculate cementation factors. Samples with a drop in amplitude signal (above 100 Hz) and high phase shifts ($\log iX > 0$) display higher formation factors (FF) over $\log FF = 2.5$. Hereby, drops in amplitude signal coincide with characteristic phase shift peaks at similar frequencies. The nearly perfect zonation of colors according to the FF illustrates the high correlation between CRS and FF, and explains the excellent fit when estimating cementation factors with CRS as input.

CRS vs. DIA

CRS parameters show a direct link to permeability and formation factor (Figure 4.9), similar to pore geometry parameters DOMsize and PoA (Figure 4.5). Hence it is to be expected that they will also correlate to each other. Indeed, samples with simple pore structures (high DOMsize, low PoA) show generally more negative slopes of $\beta_{\text{amplitude}}$ and $\beta_{\text{amplitude}}$ (Figure 4.10). Since CRS and pore geometry are interconnected, CRS shape parameters are expected to achieve similar high correlation coefficients for reservoir property predictions.

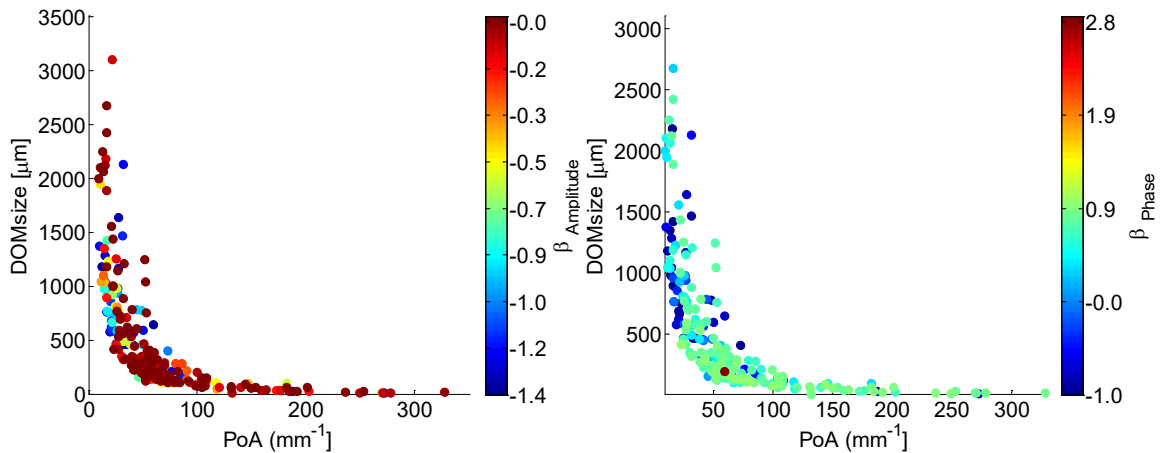


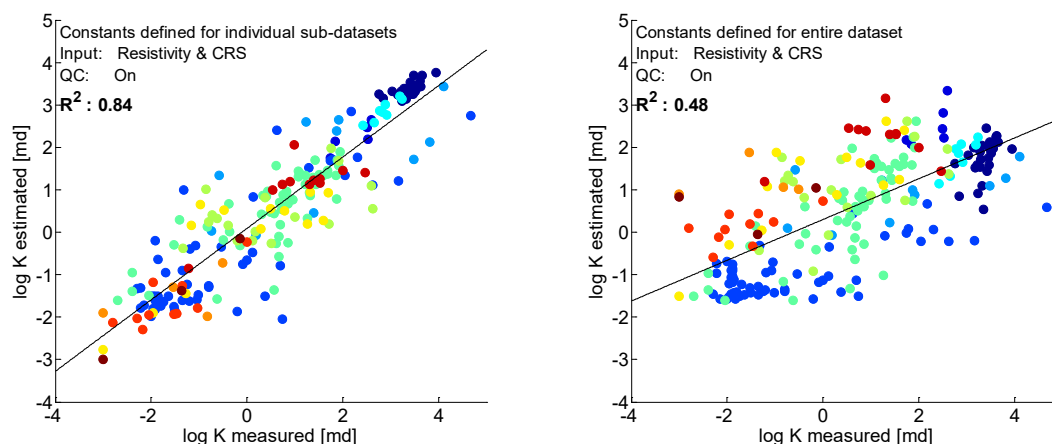
Figure 4.10: Cross-plots of Perimeter over Area (PoA) vs. Dominant Pore Size (DOMsize), color-coded with β amplitude (left) and β phase (right), illustrating link of CRS parameters to pore geometry. Samples with more negative β amplitude slopes tend to have large and simple pore structures (high DOMsize, low PoA), similar to samples with negative β phase slopes.

Predictions from CRS

Predictions of petrophysical parameters from CRS shape parameters show generally higher correlation coefficients than predictions from DIA parameters DOMsize and PoA. This underlines the strong connection between low-frequency complex resistivity dispersion and pore geometry-controlled petrophysical parameters.

Permeability can be predicted from resistivity (Ω) and CRS (β_{phase} and $\beta_{\text{amplitude}}$) using Equation 4.7 despite the high variability in each data subset.

$$K_{\text{estimated}} = a\Omega^b\beta_{\text{phase}}^c\beta_{\text{amplitude}}^d \quad \text{Eq. 4.7}$$



- Modern Stromatolite (Hamelin Pool)
- Miocene Stromatolite
- Holocene Travertine
- Holocene Tufa
- Modern Stromatolite (Bahamas)
- Mississippian Dolomite
- Miocene Reefal Framestone/Grainstone
- Cretaceous Rudist Packstone/Grainstone
- Permian Oolitic Packstone/Grainstone
- Carboniferous Wackestone/Packstone
- Cretaceous Rudist Limestone
- Tithonian/Berriasian Mudstone-Oolitic Packstone

Figure 4.11: Permeability predictions from resistivity and CRS (Eq. 4.7) for entire dataset with constants $abcd$ defined for individual subsets (left) and with constants $abcd$ defined for entire dataset (right). R -squares without quality control (QC): 0.81 (left) and 0.43 (right).

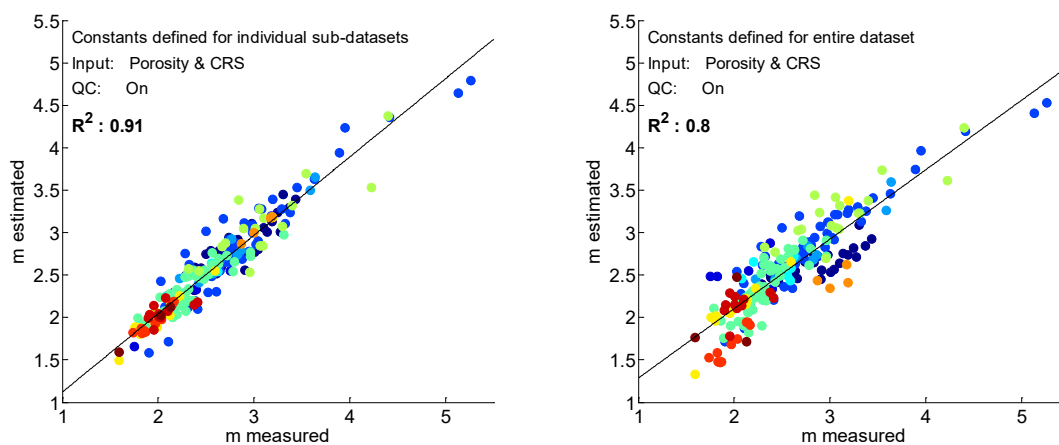
Combining results from individual predictions, i.e. tuning the constants $abcd$ to the individual data subsets, the method achieves a correlation coefficient of $R^2 = 0.84$ (Figure 4.11; left). This is significantly better than the outcome from predictions based on DIA parameters with $R^2 = 0.75$ (Figure 4.7).

However, the prediction of permeability with constants $abcd$ determined for the entire dataset lowers the correlation coefficient to $R^2 = 0.48$ (Figure 11; right), which is less than with digital image analysis (DIA: $R^2 = 0.53$). A diminished correlation is to be expected, as the combined dataset contains extreme sample heterogeneity that is unlikely to occur in a given well or even within one oil field.

Predictions of cementation exponents (m) from porosity (ϕ) and CRS (β_{phase} and $\beta_{\text{amplitude}}$) using Equation 4.8 generally have higher correlation coefficients than predictions of permeability.

$$m_{\text{estimated}} = a\Phi^b\beta_{\text{phase}}^c\beta_{\text{amplitude}}^d \quad \text{Eq. 4.8}$$

When constants $abcd$ are tuned to the individual sub-sets, correlation coefficients for cementation factor predictions from CRS are excellent with $R^2 = 0.91$ for the combined results (Figure 4.12; left). Furthermore, even the prediction of cementation factors from CRS with constants $abcd$ determined on the entire, extremely heterogeneous dataset show a very high correlation coefficient of $R^2 = 0.80$ (Figure 4.12; right). The correlations are substantially better than what is achieved with DIA input parameters ($R^2 = 0.7$ and 0.33 , respectively).



- Modern Stromatolite (Hamelin Pool)
- Miocene Stromatolite
- Holocene Travertine
- Holocene Tufa
- Modern Stromatolite (Bahamas)
- Mississippian Dolomite
- Miocene Reefal Framestone/Grainstone
- Cretaceous Rudist Packstone/Grainstone
- Permian Oolitic Packstone/Grainstone
- Carboniferous Wackestone/Packstone
- Cretaceous Rudist Limestone
- Tithonian/Berriasian Mudstone-Oolitic Packstone

Figure 4.12: Cementation factor m predictions from porosity and CRS (Eq. 4.8) for entire dataset with constants $abcd$ defined for individual sub-sets (left) and with constants $abcd$ defined for entire dataset (right). R -squares without quality control (QC): 0.87 (left) and 0.74 (right).

The high correlation coefficient of $R^2 = 0.80$ includes all samples from twelve extremely diverse carbonate datasets, indicating that a single equation can be used to estimate cementation exponents from CRS and porosity in carbonate rocks:

$$m_{\text{estimated}} = 1.25 \Phi^{0.4} \beta_{\text{phase}}^{-0.012} \beta_{\text{amplitude}}^{0.111} \quad \text{Eq. 4.9}$$

In this equation, the constants $abcd$ are determined by unconstrained nonlinear optimization using the entire dataset of 330 diverse carbonate rock samples.

Discussion

Pore geometry

This study emphasizes the extreme variability of pore geometry in carbonate rocks, which results in a large scatter between porosity and both permeability (Figure 4.2) and cementation factors (Figure 4.3). Thin-section digital image analysis (DIA) parameters illustrate the heterogeneity of the analyzed dataset with a broad spectrum of pore sizes (DOMsize) and pore network complexity (PoA) (Figure 4.4). These parameters have a close relationship to flow properties, where large and simple pore structures generally result in both high permeability (Figure 4.5; left) and high cementation factors (Figure 4.5; right). These findings corroborate previous studies on smaller datasets of carbonates (Weger et al., 2009; Verwer et al., 2011).

Fractal pore area distributions

Pore size distributions show a power-law distribution when plotted on double-logarithmic scale using non-linear binning (Figure 4.6). Fractals seem to be a re-occurring phenomenon in many natural systems (Mandelbrot, 1967; Turcotte & Brown, 1993). The Slope D of the pore size distribution also relates to flow properties of a sample, confirming that the Slope D is the fractal dimension and a measure of the complexity of a system, which in our case is the pore structure of individual samples. As a consequence, higher Slope D and higher complexity results in lower permeability (Figure 4.6; left) and lower cementation factors (Figure 4.6; right).

The fractal scaling of pore sizes could prove useful when available data about pore size distributions or pore geometries is scarce in certain scenarios. Under the assumption of scale-invariance of a pore system, statistics gathered at a certain scale can be used to determine pore distributions at smaller or larger scales (Purkis et al., 2015). Scaling rules are also valuable when building reservoir models and populating such models with pore parameters. Broad-ion-beam SEM (BIB-SEM) studies show that the fractal scaling in carbonates extends downwards from macropores into the micro- and nanopore range (Norbisrath et al., 2015). It has still to be tested if fractal scaling rules exist upwards of thin-section macropore scales. Such studies would have to include full-core scans or image logs. Several studies show that the fractal scaling is not only applicable to carbonates, but scale-invariant pore size distributions also occur in clays and mixed carbonate-siliciclastic rocks (Desbois et al., 2011; Curtis et al., 2012; Klaver et al., 2012; Houben et al., 2013; Hemes et al., 2015; Norbisrath et al., in press).

Predictions from pore geometry

Since pore geometries have deep ties with flow properties, they can be used for predictions of such properties. Taking pore geometry parameters DOMsize and PoA from DIA together with resistivity as input for permeability models, correlation coefficients of up to $R^2 = 0.75$ are achieved (Figure 4.7; left). The good correlation implies that DIA parameters can accurately describe the efficiency of the pore structure to allow fluid flow. Furthermore, predictions of cementation factors from DIA and porosity also show good correlation coefficients of $R^2 = 0.70$ (Figure 4.8; left). The extraction of pore geometric parameters, however, requires extensive and expensive special core analysis and digital image analysis of thin-sections. Although the measurements of electrical properties are also laborious, predictions from CRS parameters yield higher correlation coefficients. This advantage could partially be due to the inherent 3-dimensionality of an electrical measurement as compared to a 2-dimensional thin-section analysis, which may be a less adequate representation of the entire plug volume.

Complex resistivity spectra

In carbonate reservoirs flow properties are often hard to predict because of the complexity of the pore network. Mercury injection capillary pressure or a combination of NMR and borehole image logs are common techniques to tackle this “carbonate conundrum” (Ahr et al., 2005; Machado et al., 2011; Hulea & Nicholls, 2012). Exploiting the frequency dispersion of kHz-range complex resistivity presented in this study offers a new approach for this longstanding challenge. The feasibility of this approach is indicated by the excellent correlations between the frequency dispersion of kHz-range complex resistivity spectra (CRS) and petrophysical flow properties in a wide range of carbonate

core plug samples. Below we discuss this potential and how the fundamental relationships between low-frequency resistivity spectra and flow properties might be implemented in wire-line logging.

Chemali et al. (1995) observed little influence of polarization on low-frequency (20 kHz) wireline induction logging resistivity measurements. This agrees with our results, where this frequency represents a threshold above which the resistivity amplitude in most samples is severely affected by polarization effects. However, samples with low permeability and formation factors already show significant polarization effects even below 20 kHz (Figure 4.9).

Seleznev et al. (2011) show that MHz- to GHz-range dielectric logging is a fast and convenient way to determine kerogen content and salinity in oil shales. Bean et al. (2013) also confirm the use of these high-frequency dielectrics for estimates of water-filled porosity in wells drilled with oil-based mud. Anderson et al (2008) describe a technique of processing existing data from induction logs operating at lower frequencies to assess the dielectric permittivity for the identification of gas-producing shales. These workers use inversion to calculate dielectric constants from the 26 kHz and 52 kHz induction logs. The dielectric inversion results show dispersion effects, especially in low-resistivity rocks. They calibrate the results by laboratory core measurements and provide a means for identifying different rock types directly from resistivity logs, in shales and shale-bearing rocks. The results presented in this paper corroborate their assumption and expand them into carbonates, where dielectric dispersion allows us to estimate flow properties in a petrophysical rock typing approach. In a similar approach, Wang & Poppit (2013) demonstrate the use of several existing logging tools to study the frequency dispersion in

a gas shale formation, including wireline induction (26 kHz), LWD propagation (1MHz and 2 MHz), and wireline dielectric tools (4 frequencies from 20 MHz to 1 GHz). They show that dielectric dispersion is a function of clay volume and directly related to electrical double layer (EDL) polarization effects and the cation exchange capacity (CEC) in clays (Han et al., 2012).

Carbonates also display significant dielectric properties, possibly due to prevalence of extensive amounts of microporosity in carbonate rocks (Smith et al., 2003; Ahr, 2005; Verwer et al., 2011; Hulea & Nicholls, 2012; Lucia & Loucks, 2013; Harland et al., 2015). In addition, the dielectric dispersion is directly related to the formation factor (Figure 4.9; right) and to permeability (Figure 4.9; left), which are measures of the connectivity and openness of a pore system and are related to its specific surface area (the amount of pore wall area per volume). This corroborates the concept of low-frequency polarization effects, where interfacial polarization effects control low-frequency dielectric dispersion (Figure 4.1; Ellis & Singer, 2007).

Predictions from CRS

In our carbonate dataset, permeability can be estimated with great accuracy ($R^2 = 0.84$) just using electrical resistivity and CRS, if the model constants $abcd$ are determined for the individual datasets (Figure 4.8; left). In a dolomite dataset from the Mississippian Madison Formation in Wyoming, for example, the method achieves a correlation coefficient of $R^2 = 0.82$ for permeability predictions (Norbisrath et al., in press). This shows that permeability predictions are feasible within a well or a field only with knowledge about the general rock type from geological models or, if unavailable, with a few core plug samples to determine the constants. Furthermore, cementation exponents can be predicted

with high certainty ($R^2 = 0.80$) from porosity and CRS in our entire dataset with a universal equation (Figure 4.12; right). Since this model was defined from a comprehensive dataset, it could be used as a universal tool to predict cementation exponents in carbonate rocks (Eq. 4.9). This implies that cementation factors, which vary widely in carbonates (from 1.03 – 5.27 in our data set), potentially can be predicted in carbonates without core analysis or a knowledge of lithology. The variations of the cementation exponent m , when not identified, alter the assessment of water and oil saturation, and can drastically influence the assessment of a prospect reservoir unit in terms of producibility.

CRS frequency range

The high accuracy of our prediction indicates that low-frequency CRS are susceptible to aspects of the pore structure in a similar way as the predicted parameters, permeability and cementation factors. CRS curves show most variation in the 10,000 – 100,000 Hz frequency range (Figure 4.9). Pore structures and resulting CRS curves can, however, vary drastically, and studies on dolomites (Norbisrath et al., in press) and on shaly sands (Tong & Tao, 2008) show that permeability predictions in those rocks work best when using the 100 – 2,000 Hz range. Amplitude spectra are generally more consistent across the entire frequency range, while phase shift measurements often show spikes at low frequencies <100 Hz. This is probably due to electrode polarization of the measurement setup, although proper care was taken when mounting the sample. It appears that CRS measurements below 100 Hz are not useful and can be omitted in further studies or in possible wireline applications. Furthermore, measurements in the low-frequency range require more time, as, for example, alternating the applied electric field once (one complete AC cycle) for the 0.1 Hz measurement already takes up 20 seconds. This could become problematic during

well-logging where logging speeds are crucial, and hence it would be preferable if near-DC measurements could be omitted. It has to be seen, however, if logging tools would profit from inclusion of low-frequency dispersion data, as these could possibly be related to larger-scale features like karsts or fractures.

Challenges

Since we assume that the silver membranes used in our measurement setup establish good contact over the entire surface of both plug ends, our complex resistivity measurements are inherently 3-dimensional, and the resulting amplitude and phase shifts are a result of a combination of all features of the rock volume and its pore structure. This implies that CRS curves contain the most reliable information for more homogeneous plug samples. However, homogeneity is often not given for carbonate core plug samples, which complicates accurate permeability and cementation factor predictions. This is especially true for datasets with rocks that show extensive anisotropy due to layering (travertines, tufas, some mudstones), fractures, and vuggy porosity (reefal framestones). These features seem to go undetected by dielectric measurements. This plug-scale heterogeneity underlines the often-discussed issues of upscaling results from core plugs into reservoir models, as the small core plug cannot be used to represent large-scale, heterogeneous flow units. However, a continuous dielectric measurement from a wireline tool, could potentially give a much more accurate depiction of the pore structure in a reservoir unit than could otherwise be obtained from plug measurements because the logging tool integrates the low-frequency resistivity measurement over a larger unit.

Technology for wireline applications

The fundamental relationships between low-frequency resistivity spectra and flow properties could be tested in a well-logging scenario. However, CRS frequencies used in this study for flow predictions are not covered by existing logging tools. Dielectric dispersion properties are to date mostly used to estimate water saturations and salinity with tools operating at a much higher frequency range (20 MHz to 1 GHz) (Hizem et al., 2008). Since there are currently no tools measuring low-frequency CRS, testing our findings obviously necessitates the development of a new low-frequency dielectric tool.

Laterolog and induction resistivity logging tools with multiple transmitter-receiver spacings are already common, but mostly used for invasion profiling and skin-effect correction. Hypothetically, their measurement frequencies could be changed so that they would measure at different frequencies but at the same investigation depth. Furthermore, it might be possible to process the signal of existing induction logging tools to analyze dielectric dispersion effects after Anderson et al. (2008). This approach, however, is limited to the measurement frequencies of these tools. The concept for a wireline tool that measures complex resistivity with variable length arrays is shown by Sternberg et al. (1987) and at variable frequencies by Scott & Olhoeft (1980).

Our permeability and cementation factor prediction models use CRS and resistivity or porosity input data (Eq. 4.7 and 4.8), respectively. In a well-logging scenario, resistivity data for permeability predictions can be acquired from conventional deep resistivity tools. Porosity data as input for cementation factor predictions can come from conventional density-neutron porosity logs. To acquire CRS data, a new low-frequency complex

resistivity wireline tool would have to be developed. Based on our results, target frequency range for this tool would be 100 – 100,000 Hz (Figure 4.9; bottom).

Since the prediction method includes constants that change for different rock types, a general idea of the lithology down-hole would be required. Sidewall core could be used to calibrate the tool with plug measurements. For the prediction of cementation exponents, on the other hand, one could potentially use the universal parameters put forward in this study, which have been shown to produce reliable estimates in all analyzed samples across a broad range of carbonate rock types (Eq. 4.9). However, a new tool would have to be calibrated with and compared to CRS and flow parameters from core plug measurements.

A calibrated low-frequency dielectric wireline tool could greatly enhance the down-hole assessment of pore geometry and the intrinsic reservoir properties of a reservoir unit, especially in heterogeneous carbonate rocks. Specifically, the continuous measurement this tool could provide has great advantages over solitary core plug measurements or well tests at certain depths. Continuous permeability and cementation exponent curves would be of high value in both exploration and production phase, to determine perforation intervals and later understand the dynamic flow of the reservoir model. Additional usage scenarios for a potential low-frequency dielectric wireline tool could be both for conventional and unconventional reservoirs, as low-frequency CRS may contain many more undiscovered relationships between important reservoir parameters.

Future work: temperature, salinity, and water saturation effects on dielectric properties

There are three main uncertainties in the CRS prediction method. Firstly, the effects of changing water salinity should be studied. This study only uses samples saturated with 35

ppt NaCl brine. Weller et al. (2011) show that changing salinity mainly affects the overall value, but not the shape of their complex conductivity curves in three sandstone samples.

Secondly, the effects of changing temperature on low-frequency dielectric properties in natural rocks have not been sufficiently assessed yet. All measurements in this study were performed at room temperature. It is well known, however, that high temperatures generally disturb the alignment of dipoles in an outer field, resulting in a decrease of the dielectric constant with temperature. It has yet to be seen if this decrease in dielectric constant follows a uniform pattern solely related to the pore structure, or if more complicated effects occur.

Thirdly, the effects of changing water saturation or wettability have to be determined. All samples in this study are measured at 100% water saturation. Since dielectric properties in the low-frequency range are mostly attributed to the rock-fluid interface, wettability could have a great impact on the measured CRS. On the other hand, water saturation might not affect CRS much, as long as a continuous water film along the surface area of the rock is maintained, which would enable direct predictions of cementation exponents and permeability in at least partially hydrocarbon-saturated intervals, as well. Based on the CRS curves (Figure 4.9), peaks in phase shift especially in high-permeability samples often seem to occur above our measurement range of up to 100,000 Hz. Since our analyses and predictions involve slope data closely related to these peaks, further studies should include measurements possibly up to several hundred kHz.

Conclusion

Thin-section digital image analyses (DIA) corroborate previous findings of strong ties between pore structure and flow properties in carbonate rocks, where a large and simple

pore structure results in higher values of both permeability and cementation exponents. The pore size distribution in all 330 samples follows a power law that indicates fractal scaling of pore sizes in carbonate rocks. The power law implies predictability of the pore space, and could prove useful in data-scarce scenarios and in reservoir modeling. Fractal scaling of pore space potentially helps in the assessment of pore properties outside the scale of acquired data for a certain project or well. Similarly, it could help to upscale and populate a reservoir model with pore size information.

Results from electrical measurements show that complex resistivity spectra (CRS) in carbonates are directly related to plug permeability and formation factors, and can be used to predict reservoir properties. Our prediction models include constants that are defined with unconstrained non-linear optimization between measured input and output parameters. When constants are defined on the twelve individual sub-datasets, the method achieves overall correlation coefficients of $R^2 = 0.84$ and $R^2 = 0.91$ for permeability and cementation factor predictions, respectively. When constants are defined on the entire extremely heterogeneous dataset, correlations are lower for permeability with $R^2 = 0.48$, but still high for the cementation factor with $R^2 = 0.80$. The high accuracy of predictions using CRS shape parameters leads us to propose the following universal equation to determine cementation factors from complex resistivity spectra:

$$m_{\text{estimated}} = 1.25 \varphi^{0.4} \beta_{\text{phase}}^{-0.012} \beta_{\text{amplitude}}^{0.111} \quad \text{Eq. 4.9}$$

All measurements are performed on core plugs in the laboratory, but the found relationships should also be applicable to wireline measurements. However, no low-frequency dielectric wireline tool currently exists to measure CRS down-hole. Yet, it appears simple enough to engineer such a tool by modifying existing tools that measure

resistivity profiles. These tools use several transmitter-receiver spacings to achieve different depths of investigation but could theoretically be modified to measure at the same depth but different frequencies. Additionally, existing multi-array induction logs could be processed to gather information about low-frequency dielectric dispersion and establish an alternative method for assessment of reservoir properties down-hole. Such an endeavor would be especially advantageous in heterogeneous carbonate rocks where permeability and cementation factors are hard to assess. A continuous measurement of water saturation, and especially permeability, would greatly enhance reservoir models and reservoir estimates. Since CRS are mainly controlled by the pore geometry, these measurements could theoretically also be independent of water saturation or salinity.

Chapter 5: Nanopore Imaging in Vaca Muerta Mudrocks to Evaluate Controls on Complex Resistivity Spectra in Unconventional Reservoirs

Summary

Nanopore geometry and mineralogy are key parameters for hydrocarbon exploration and production in unconventional reservoirs. This study describes an approach to find relations between low-frequency complex resistivity spectra (CRS), nanopore geometry, and mineralogy in order to use CRS for estimates of reservoir parameters concerning flow, storage, and producibility.

For this purpose, the frequency dispersion of CRS is analyzed in 56 mudrock core plugs from the Vaca Muerta Formation in Argentina, along with cementation factors (m), carbonate content (CO_3) and total organic carbon (TOC). To quantify the nanoporosity, a subset of 23 samples are milled with broad-ion-beam (BIB) and imaged with scanning electron microscopy (SEM); the image rasters of these samples are stitched together into high-resolution BIB-SEM mosaics and investigated with digital image analysis techniques. Furthermore, humidity-drying is used to study the relations between irreducible water saturation ($S_{w_{\text{irr}}}$) and electrical properties on a subset of 13 samples.

In regards to controlling factors, porosity is the dominant control on electrical properties in these mudrocks. The mudrocks have a more complicated pore geometry at nano scales when compared to the $\text{ISA}_{2\text{D}}$ in coarser-grained carbonates (see chapter IV). Yet no conclusive evidence that pore geometry influenced the electrical properties in the mudrocks is found. Pore geometry parameters Dominant pore size (DOMsize), Perimeter over Area (PoA), and the slope of the power-law pore size distribution (Slope D) do not correlate with cementation factors or CRS. Instead, mineralogy plays a decisive role in determining electrical properties. Cementation exponents are generally higher in rocks

with high TOC and low CO₃ content, but predictability from CRS is limited with correlation coefficients of $R^2 = 0.47$ and $R^2 = 0.49$, respectively. CRS can be used to estimate porosity and cementation factors with high correlation coefficients of $R^2 = 0.71$ and $R^2 = 0.94$, respectively. Estimates of the 2-dimensional Interfacial Surface Area (ISA_{2D}), which is a function of both pore geometry and porosity, achieve an $R^2 = 0.59$.

The results of this study suggest that low-frequency dielectric rock properties, if measured down-hole, could be useful to find sweet spots in unconventional reservoirs, and to accurately determine cementation factors independent of formation fluids and porosity.

Introductory Remarks

Nano- and micropores are the dominant pore types in unconventional reservoirs but the controls of pore structure on petrophysical properties in unconventional rocks are poorly understood. This is mostly due to the small size of pores associated with clay minerals, which has prevented their accurate quantification for a long time (Bustin et al., 2009). Therefore, most researchers focus on indirect methods like mercury injection capillary pressure (MICP) (Nelson, 2009), nuclear magnetic resonance (NMR) (Clennell et al., 2006), or gas adsorption (Clarkson et al., 2011, 2013) to assess the pore geometry and relations to flow and storage properties in fine-grained rocks. TOC-rich intervals invoke further difficulties, as they often show increased variability of pore types due to secondary porosity in mature organic matter (Passey et al., 2010; Pommer & Milliken, 2015).

Recently, broad-ion-beam milling scanning electron microscopy (BIB-SEM) has been developed to create high-quality cross-sections in natural rocks that enables quantification of their micro- and nanoporosity (Loucks et al., 2009; Desbois et al., 2011; Laurich et al., 2014; Klaver et al., 2015a, 2015b; Norbistrath et al., 2015). This pore-scale imaging method

is used here to assess the influence of nanopore geometry on dielectric rock properties. Specifically, it is also used to quantify the 2-dimensional Interfacial Surface Area (ISA_{2D}), which represents the rock-fluid interface of a sample, and is supposed to have a strong influence on low-frequency dielectric rock properties.

The BIB-SEM analysis also enables a unique quantitative and qualitative comparison of clay- and kerogen-dominated porosity in mudrocks with carbonate microporosity from a previous BIB-SEM study (Norbisrath et al., 2015). The assessment of electrical flow properties in samples with different mineralogy should further clarify if there are universal nanopore geometric factors controlling electrical resistivity, or if mineralogy plays a decisive role such as hydroxyl layers in swelling clays, increased double-layer surface conductivity in clays, and pyrite associated with clays. Furthermore, it is largely unknown how carbonate content and total organic carbon (CO_3 and TOC) influence complex resistivity spectra and cementation factors, hence the goal is to find fundamental relationships between these parameters that can be useful in well-log inversion and interpretation. Additionally, we analyze the pressure-dependency of compacted mudrocks by varying the confining pressure in the measurement chamber from 2 MPa to 50 MPa effective pressure.

Electrical charges in mudrocks

Electrical phenomena at the rock-fluid interface in a clay-rich mudrock are linked to the electrical double layer (EDL) that occurs on the surface of clay minerals (Waxman & Smits, 1968; Passey et al., 2010; Revil, 2012). The key feature of the EDL are the contained free cations which are able to move when alternating current (AC) is applied. Preferential spatial accumulation of these movable cations within the pore structure results in temporary

charge storage and so-called interfacial polarization of a porous medium. Given the relatively large inertia of this process that involves physical movement of cations, interfacial polarization at the rock-fluid interface occurs only at lower frequencies (Figure 5.1). Therefore, it is deemed to be the main control on low-frequency dielectric rock properties, or complex resistivity spectra (CRS) (Cerepi, 2004; Hizem et al., 2008). Simply put, the low-frequency dispersion of CRS, which is measured in this study, is hypothesized to be mainly a result of the pore structure. This is the underlying concept that enables a new modeling approach that uses CRS to estimate reservoir properties. The approach has shown to work in shaly sandstones (Tong & Tao, 2008) and carbonate rocks (Norbisrath et al., in press) [chapter 4]. In this study, it is applied to a subsurface core plug dataset of fine-grained and kerogen-rich mixed carbonate-siliciclastic mudrock samples from the Vaca Muerta Formation in Argentina.

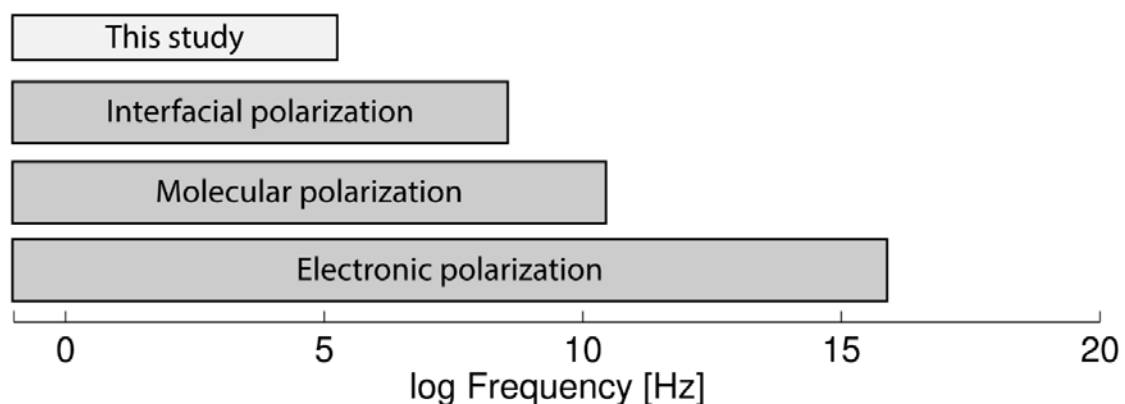


Figure 5.1: Span of polarization mechanisms in the frequency domain after Hizem et al. (2008). Interfacial polarization at rock-fluid boundary plays important role in low-frequency dielectrics. Frequency range of measurements in this study shown on top (0.1 – 100,000 Hz).

Dataset

The dataset of this study is comprised of 56 subsurface mudrock core plug samples from two wells drilled in the Vaca Muerta Formation (VMF) of the Neuquén Basin in Argentina (Mitchum and Uliana, 1985; Spalletti et al., 2000; Howell et al., 2005; Kietzmann et al., 2011; Leanza et al., 2011). The VMF is Late Jurassic to Early Cretaceous in age and constitutes the main hydrocarbon source rock in the basin (Uliana & Legarreta, 1993; Zeller et al., 2013) but has more recently been targeted as an unconventional reservoir (Garcia et al., 2013; Crousse et al., 2015). The samples are from depth intervals where the VMF is approximated to be in the oil window (Legarreta & Villar, 2011), which is corroborated by the thermally mature appearance of the organic matter in the BIB-SEM mosaics (Figure 5.2).

Methods

All 56 core plug samples are analyzed on porosity, carbonate content (CO_3), total organic carbon (TOC), cementation factors, and complex resistivity spectra (CRS). Nanopore geometry and 2-dimensional Interfacial Surface Area (ISA_{2D}) are quantified in 23 samples, and the irreducible water content ($S_{w_{\text{irr}}}$) is measured in 13 samples.

Acid washing, elemental analysis, and humidity drying

Crushed material from cut-offs of the core plugs is used to study the mineralogy of the samples. The carbonate content (CO_3) is determined by cold acid washing with 10 % HCl and subsequent weighing of remaining sample material. An elemental analyzer, utilizing a process of combustion and infrared spectroscopy, is used to assess the percentage of total organic carbon (TOC) contained in the samples. Porosity is measured by comparing caliper bulk plug volume to true skeletal volume from Helium pycnometry utilizing Boyle's law.

A subset of 13 samples is also analyzed on the amount of irreducible water saturation ($S_{w_{irr}}$) by humidity drying and comparison of the weight to fully dried samples (Bush & Jenkins, 1970).

BIB-SEM and pore geometries

In order to determine the importance of nanopore geometry and 2-dimensional Interfacial Surface Area (ISA_{2D}) for frequency dispersion of the CRS, a subset of 23 samples is imaged in high detail with the broad-ion-beam milling scanning electron microscopy (BIB-SEM) method.

The BIB-SEM method enables direct quantification of the amount of ISA_{2D} in the sample, as the milling removes any surface roughness and produces a nanometer-precision flat surface that can be accurately segmented into pore and solid phase (Figure 5.2).

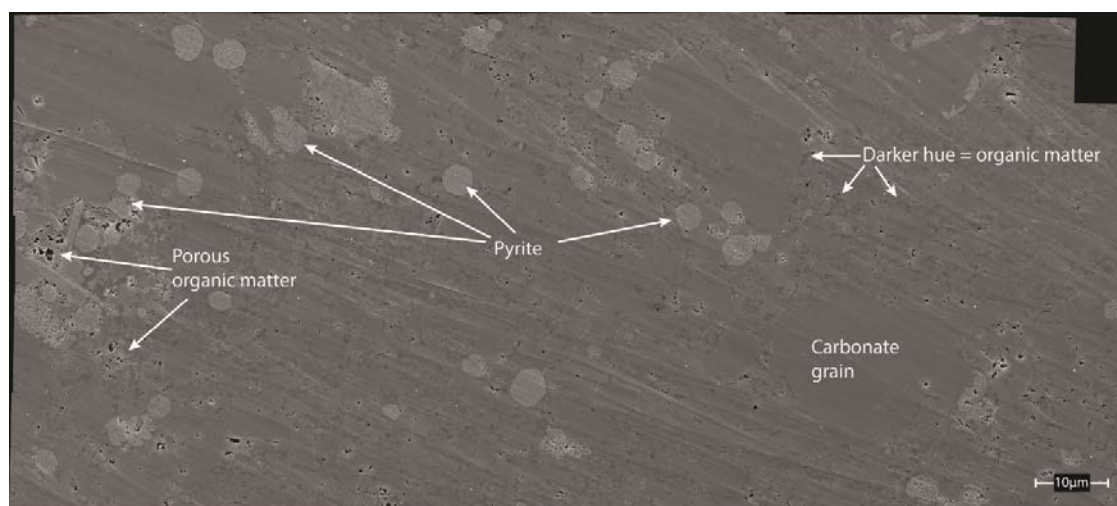


Figure 5.2: Example of un-cropped broad-ion-beam milling scanning electron microscopy (BIB-SEM) mosaic of sample P27_2a at 15,000x magnification, consisting of 50 SEM images. Irregularities at right edge are result of un-guided manual image raster acquisition. Dispersed round pyrite framboids in matrix of carbonate (44 % CO_3) and darker appearing organic matter (4.4 % TOC). Most porosity is within organic matter. Left edge: large, bubbly pores in mature organic matter.

The process involves several steps. First, rectangular subsamples (10 x 9 x 3 mm) are prepared with a high-precision diamond saw. The samples are cut in a way to produce two parallel long edges with one orthogonal short edge. Orthogonality ensures that the milling surface is parallel to the ion beam and the rock is milled down evenly. The short edge is then placed for ~8 hours at 5kV accelerating voltage in a JEOL IB-19500 CP ion mill. Polished samples are sputtered with Au/Pd (gold/palladium) for 20 seconds. SEM analyses are performed with a FEI Quanta 600 F field emission scanning electron microscope (FE-SEM). For each sample, several low- and high-magnification images are taken that focus on special features and the overall pore geometry of the milled surface. Then, an area that appears representative for the entire milled area is chosen to capture the image raster that will be stitched and quantified. SEM mosaics are acquired in a 10 by 5 image raster for a total of 50 images per mosaic (Figure 5.2). Individual images are taken at 15,000x magnification at 2048 by 1768 resolution at a scanning speed of 10 μ s per pixel, resulting in pixel size (side length) of 9.56 nm. Low accelerating voltage of 10 kV ensures shallow penetration depth of electron beam to focus on 2D surface geometry.

Broad-ion-beam (BIB) milled areas are approximately 0.8 - 1 mm² in size (Figure 5.3). All 23 stitched BIB-SEM mosaics consist of 50 images each and average around 17,000 * 8,000 pixels (165 * 75 μ m) in size. This translates to total mosaic areas of around 12,400 μ m² (0.012 mm²).

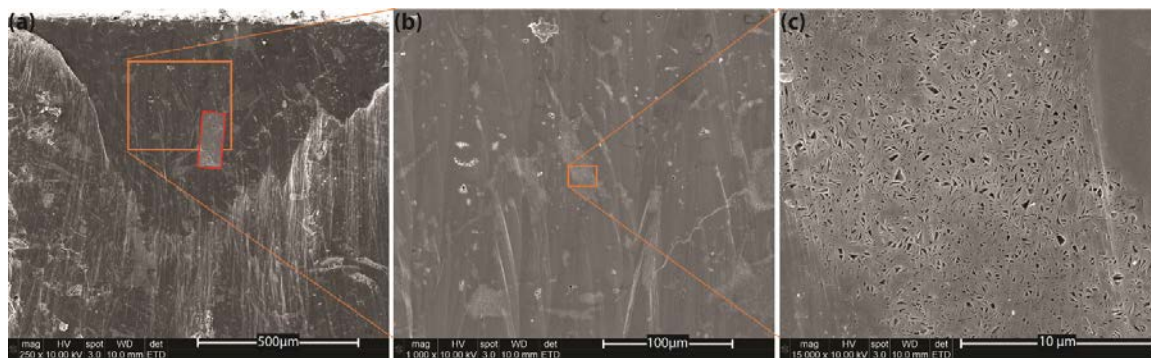


Figure 5.3: Broad-ion-beam (BIB) milled area with scanning electron microscopy images at increasing magnification from left to right, illustrating low surface roughness and quantifiable mudrock pore structure. (a) Overview of v-shaped, milled area. Red box indicates BIB-SEM mosaic area in this sample. (b) Distribution of smectite in milled area as indicated by lighter appearance due to high porosity and lower density. (c) Close-up of smectite nanopore structure. mag = magnification; HV = high voltage; spot = electron spot size in nanometers; WD = working distance; det = detector; ETD = Everhart-Thornley detector.

Image processing

Images are acquired with an overlap of around 25% to ensure successful automatic stitching into mosaics with Kolor Autopano Giga photo-panorama software. The mosaics are segmented into solid phase and pore phase with a combination of thresholding and sobel-edge-detection algorithms (Houben et al., 2013). The pore structure of the segmented, binary mosaics is quantified with open-source ImageJ software for digital image analysis (DIA) to extract pore geometry parameters.

DOMsize and PoA

Dominant pore size (DOMsize) and Perimeter over Area (PoA) are the main output variables of DIA (Weger et al., 2009). DOMsize is the maximum pore size needed to comprise 50 % of the porosity on a thin-section (from a cumulative addition starting with the smallest pores). The parameter gives a good indication of the overall pore network size. It is converted from area (pixel count) to size equivalent diameter. PoA is assessed by

relating the sum of the perimeter of all pores to the sum of the area of these pores. The parameter describes the complexity of the pore network. For calculations of both DOMsize and PoA, only pores consisting of at least 100 pixels are used, i.e. only pores that are larger than 960 nm² are considered for the DIA.

Interfacial Surface Area (2D)

The 2-dimensional Interfacial Surface Area (ISA_{2D}) is the ratio of the sum of the outlines of all pores identified on a mosaic over the total size of the mosaic, or simply the amount of pore perimeter per cross-sectional area:

$$ISA_{2D} = \frac{\sum \text{Perimeter}}{\text{Area}_{\text{Mosaic}}} \quad \text{Eq. 5.1}$$

The parameter ISA_{2D} increases both with increasing amount of porosity and increasing complexity of the pore system. This separates it from the PoA parameter, which only increases with complexity and is indifferent to the amount of porosity, hence a purely geometric parameter.

Slope D

Pore area distributions are analyzed by sorting all pores identified from DIA into pore size bins, where subsequent bins always double in bin width. The amount of pores per bin is normalized by mosaic size (analyzed area) and bin width (pore size range), and results plotted against bin centers (pore size) on a double logarithmic scale (Klaver et al., 2012; Houben et al., 2013; Hemes et al., 2015). Least square linear regression analysis is used to quantify the power law exponent that defines the slope of the pore size distributions:

$$\text{Slope D} = - \frac{\log\left(\frac{\text{Pore area frequency}}{\text{Mosaic size} * \text{Bin width}}\right)}{\log(\text{Pore area})} \quad \text{Eq. 5.2}$$

The negative of the slope ($D = - \text{slope}$) thereby represents the fractal dimension of the pore space (Mandelbrot, 1967), in the following referred to as Slope D.

Cementation factors

Electrical resistivity is measured in a true four-electrode setup in a log sweep of 15 discrete frequencies from 0.1 – 100,000 Hz and at varying pressure steps up to 50 MPa effective pressure on fully 35ppt NaCl brine-saturated core plug samples. Steps include 2, 5, 10, 15, 20, 25, 30, 40, 50, 40, 30, 25, 20, 15, 10, 5, and 2 MPa effective pressure (confining minus pore pressure). The varying pressure conditions are used to assess the influence of overburden on electrical properties. The log sweep of measurements takes around two minutes at each pressure step. This means that one pressure cycle takes around 30 minutes. For a more detailed description of the measurements and setup see Norbistrath et al. (2015) [chapter 2].

For calculations of cementation exponents, pore fluid temperature-corrected (Arps, 1953) measurements of resistivity amplitude (R_f) at 50 MPa effective pressure and 720 Hz are used as input for Archie's (1942) empirical formula,

$$FF = \frac{R_f}{R_w} = \phi^{-m} \quad \text{Eq. 5.3}$$

where FF is the Formation Factor, R_f is the measured resistivity at 100% water saturation, R_w is the resistivity of the saturating fluid, ϕ is the porosity, and m is the cementation exponent.

Complex resistivity spectra (CRS)

Complex resistivity is measured across the sample and across a reference resistor connected in series with the sample. The amplitude ratio and phase shift between the two signals is used to measure the complex electrical impedance (Z^*) of the sample,

$$Z^* = R - iX \quad \text{Eq. 5.4}$$

where R is the resistance and iX the reactance (Knight & Nur, 1987). The frequency dispersion in the 10,000 – 100,000 Hz range is quantified by fitting a curve to the CRS of both amplitude (resistance R) and phase shifts (reactance iX). The extracted CRS slopes of both amplitude and phase shift ($\beta_{\text{amplitude}}$ and β_{phase}) are used to estimate reservoir properties.

Predictions of reservoir properties

We use a modified model from Tong & Tao (2008) for estimates of various reservoir and other properties,

$$X_{\text{estimated}} = aY^b Z_1^c Z_2^d \quad \text{Eq. 5.5}$$

where X is the parameter to be estimated (cementation factor, porosity, Interfacial surface area, carbonate content, total organic carbon, or irreducible water saturation), Y is either porosity (ϕ) or resistivity amplitude (R_f), and Z_1 and Z_2 are either are the CRS slopes in the 10 – 100 kHz range ($\beta_{\text{amplitude}}$ and β_{phase}) or pore geometry parameters from BIB-SEM mosaics (DOMsize and PoA). The constants $abcd$ are determined with unconstrained non-linear optimization (Nelder & Mead, 1965).

Results

TOC and CO₃ content

Total organic carbon (TOC) values range from 0.06 – 10.15 % TOC and carbonate content (CO₃) values from 7.09 – 92.98 % CO₃ in the dataset. Plotted against each other, there is a very weak trend of lower TOC with higher CO₃ content (Figure 5.4).

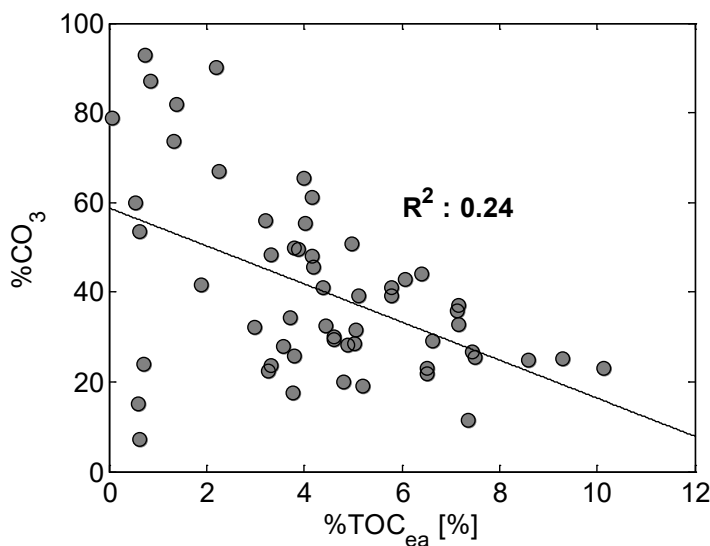


Figure 5.4: Cross-plot of TOC and CO₃ of 56 mudrock samples from the Vaca Muerta Formation, indicating a trend of lower organic carbon at higher levels of carbonate content.

Cementation factor m and porosity

Cementation factors (m) at 50 MPa effective pressure range between 1.27 - 3.2 and porosity between 0.2 - 17.5 %. Cementation factors have a positive correlation to porosity ($R^2 = 0.73$) (Figure 5.5; top) and TOC content ($R^2 = 0.39$) (Figure 5.5; middle). Samples with more than 7.5 % porosity only show cementation factors above $m = 2.0$, and more than 8.0 % TOC results in cementation factors only above $m = 2.5$. A slight trend of lower cementation factors with increasing carbonate content ($R^2 = 0.19$) exists, but samples with

varying CO₃ content can have high ($m > 2.5$) or low ($m < 1.5$) cementation factors (Figure 5.5; bottom).

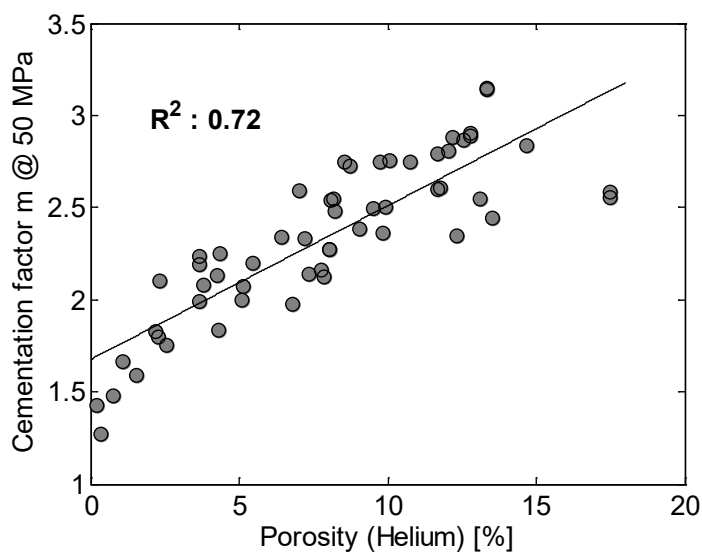
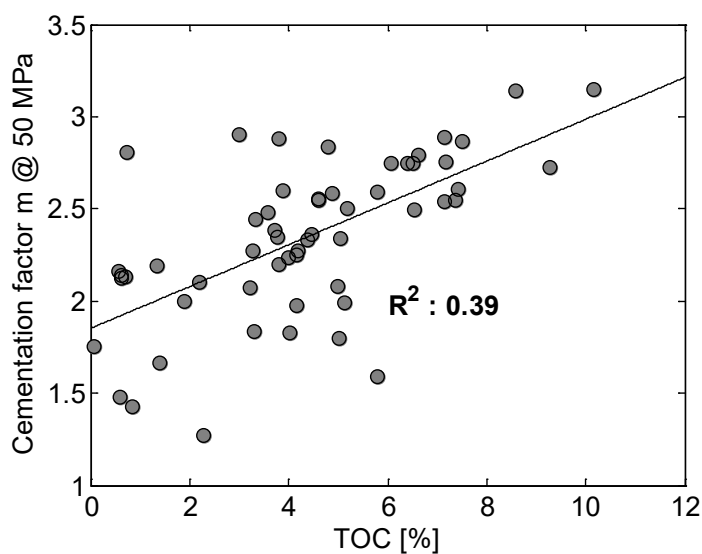


Figure 5.5:
Cementation factors of 56 Vaca Muerta mudrocks vs. porosity (top), total organic carbon (TOC; middle), and carbonate content (CO₃; bottom). Higher porosity and higher TOC result in higher cementation factor m , whereas increased carbonate content tends to lower m .



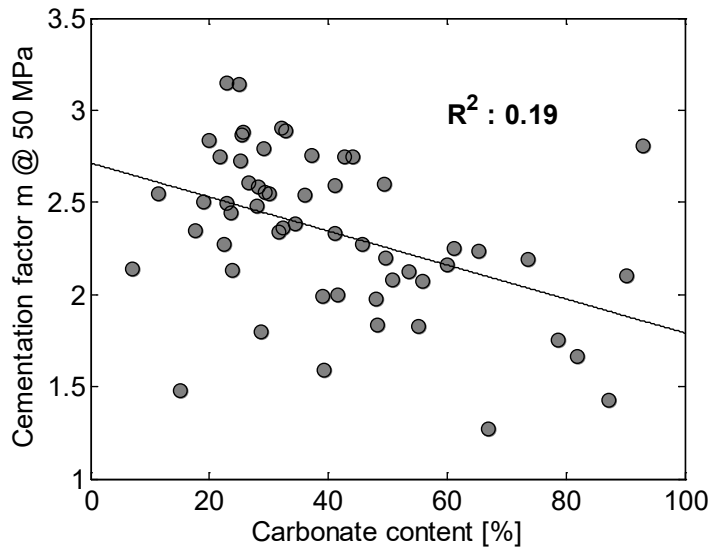


Table 5.1: Mineralogy parameters porosity, carbonate content (%CO₃), total organic carbon (%TOC), and cementation factors at 5 and 53 MPa confining pressure.

Sample	Phi [%]	%CO ₃	%TOC (EA)	m @ 5 MPa	m @ 53 MPa
1	8.54	21.80	6.51	2.49	2.75
2	8.04	22.49	3.27	2.19	2.28
3	5.09	41.54	1.88	1.92	1.99
4	7.34	7.09	0.62	2.08	2.14
5	9.52	22.95	6.53	2.44	2.50
6	3.67	39.16	5.13	1.90	1.99
7	2.29	28.60	5.03	1.68	1.80
8	0.35	66.90	2.27	1.20	1.27
9	5.44	49.73	3.80	2.10	2.20
10	3.79	50.74	4.98	1.91	2.08
11	7.77	59.95	0.56	2.08	2.16
12	2.18	55.22	4.03	1.73	1.83
13	8.08	35.95	7.13	2.32	2.54
14	9.05	34.40	3.72	2.23	2.38
15	12.78	32.21	2.99	2.64	2.90
16	0.78	15.05	0.59	1.45	1.48
17	12.18	25.68	3.80	2.65	2.88
18	7.85	53.63	0.62	2.01	2.12
19	13.10	30.14	4.61	2.40	2.55
20	13.54	23.54	3.33	2.31	2.44
21	8.19	11.42	7.37	2.31	2.55
22	12.31	17.66	3.76	2.19	2.35

23	8.23	27.94	3.58	2.31	2.48
24	5.16	55.84	3.22	1.97	2.07
25	8.04	45.72	4.19	2.14	2.27
26	6.45	31.65	5.05	2.10	2.34
27	4.29	48.38	3.31	1.72	1.84
28	4.27	23.81	0.72	2.10	2.13
29	3.65	73.64	1.34	2.11	2.19
30	4.35	61.25	4.17	2.07	2.25
31	1.53	39.23	5.79	1.45	1.59
32	7.04	41.02	5.78	2.44	2.59
33	2.55	78.77	0.06	1.70	1.75
34	1.08	81.82	1.39	1.55	1.66
35	7.22	41.09	4.39	2.15	2.33
36	0.20	87.16	0.85	1.40	1.43
37	10.76	42.71	6.07	2.54	2.75
38	9.85	32.35	4.45	2.23	2.36
39	17.47	29.48	4.61	2.35	2.55
40	9.94	18.94	5.19	2.39	2.50
41	11.68	49.44	3.88	2.42	2.60
42	2.35	90.13	2.19	1.95	2.10
43	12.05	92.98	0.73	2.60	2.80
44	13.36	23.00	10.15	2.84	3.15
45	8.73	25.21	9.29	2.47	2.72
46	12.78	32.74	7.16	2.61	2.89
47	11.77	26.66	7.44	2.52	2.61
48	11.69	29.23	6.62	2.58	2.79
49	10.06	37.17	7.17	2.56	2.76
50	12.57	25.36	7.49	2.67	2.87
51	13.33	24.97	8.58	2.93	3.14
52	9.76	44.17	6.40	2.55	2.74
53	14.68	20.00	4.80	2.66	2.84
54	3.66	65.36	4.00	2.11	2.24
55	17.49	28.22	4.89	2.40	2.59
56	6.81	48.04	4.17	1.95	1.97

Pressure dependency of m

The analyzed mudrock samples show an increase of cementation exponent (m) with increase in confining pressure (CP). The mean change in cementation exponent between 5

and 53 MPa CP measurements is 12.6 ± 5.1 % (Figure 5.6). The pressure dependency is also related to the amount of porosity whereby higher porosity samples show higher absolute increase of m (Figure 5.7).

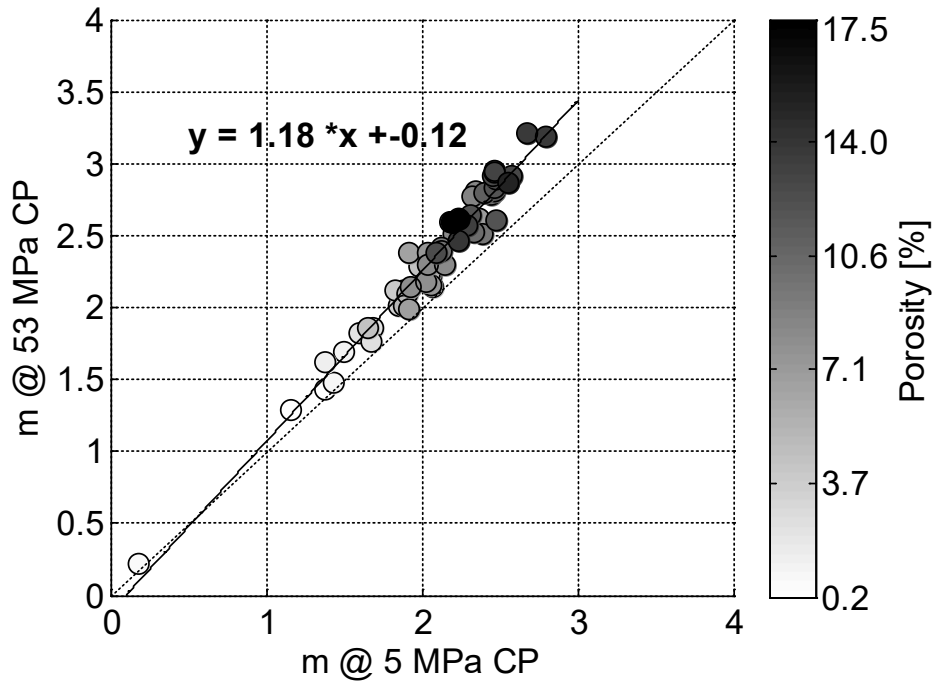


Figure 5.6. Cross-plot of cementation factors m measured at 5 MPa vs 53 MPa confining pressure, grayscale indicates porosity. Plot demonstrates increase of m with increasing pressure. Higher porosity samples hereby show higher absolute increase of m . Dashed line is the unity function. Equation of linear regression plotted next to solid regression line.

Samples also show an overall small hysteresis effects for measurements at 5 MPa CP before and after the pressure sweep up to 53 MPa CP. After experiencing the higher pressures, subsequent 5 MPa measurements show higher m -values. The mean hysteresis in cementation exponent is 3.6 ± 2.1 % (Figure 5.7).

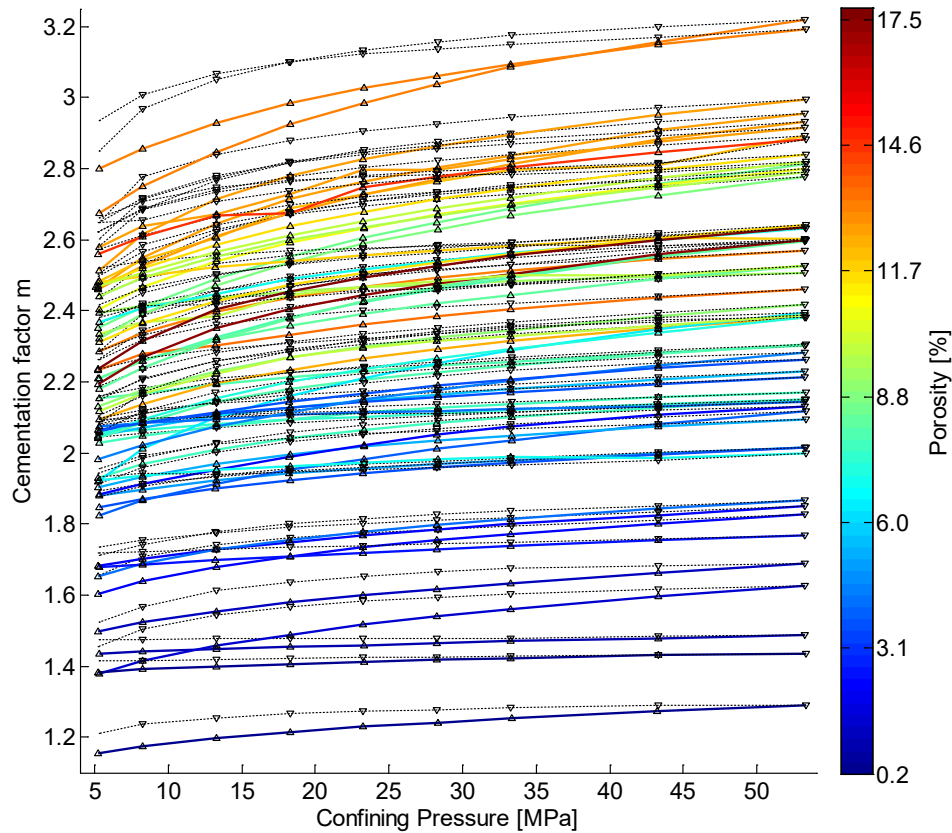


Figure 5.7: Plot of confining pressure vs cementation factor m . The increasing pressure leg is color-coded with porosity, while the decreasing pressure leg is plotted as black, dashed line. All samples show hysteresis effects, i.e. a different cementation factor at 5 MPa before and after being pressurized to 53 MPa.

The samples with higher cementation factors ($> m = 2.0$) generally show higher percental increase ($> 10\%$) of cementation factors between measurements at 2 and 50 MPa effective pressure ($EP = CP - \text{pore pressure of } 3 \text{ MPa}$) (Figure 5.8; top), and more hysteresis effects ($> 5\%$) (Figure 5.8; bottom). These samples also generally have a higher porosity.

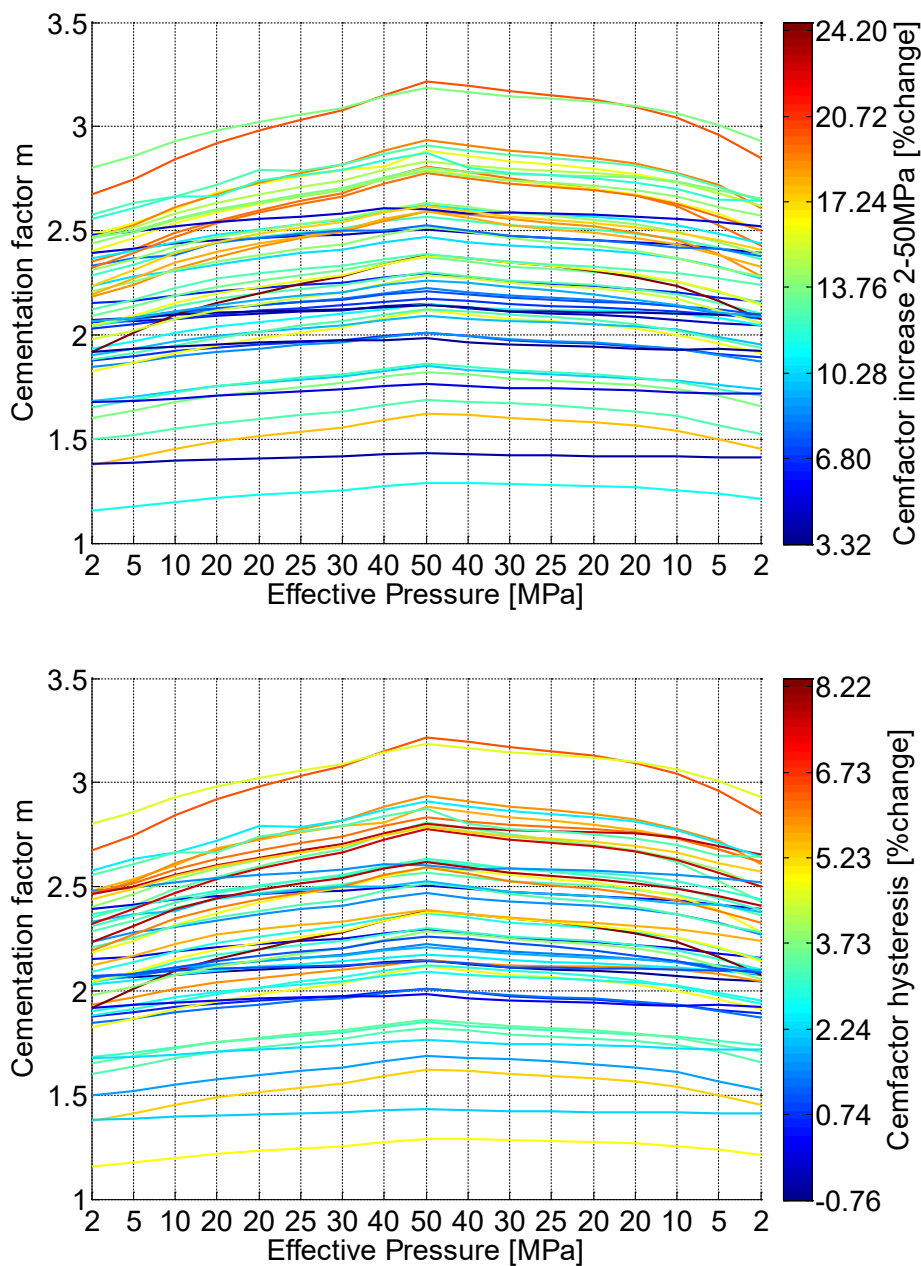


Figure 5.8: *Effective pressure (EP) vs cementation factor for increasing and decreasing pressure leg (2 MPa - 50 MPa - 2 MPa), color-coded with percent increase in cementation factor (top) and amount of hysteresis after pressure cycle (bottom). Samples with higher cementation factors show higher percent changes for both analyses.*

Irreducible water saturation ($S_{w_{irr}}$)

Humidity-drying on a subset of 13 mudrock samples reveals irreducible water saturations ($S_{w_{irr}}$) between 24.2 – 100 %. Samples with higher carbonate content (CO_3) show higher $S_{w_{irr}}$ (Figure 5.9; left). The samples with higher $S_{w_{irr}}$ content also generally have less porosity, which increases the effect of a small amount of irreducible water on the percentage of $S_{w_{irr}}$. Because porosity exerts a strong control on cementation exponents and higher $S_{w_{irr}}$ means lower porosity, an increasing amount of $S_{w_{irr}}$ results in lower cementation exponents (m) (Figure 5.9; right).

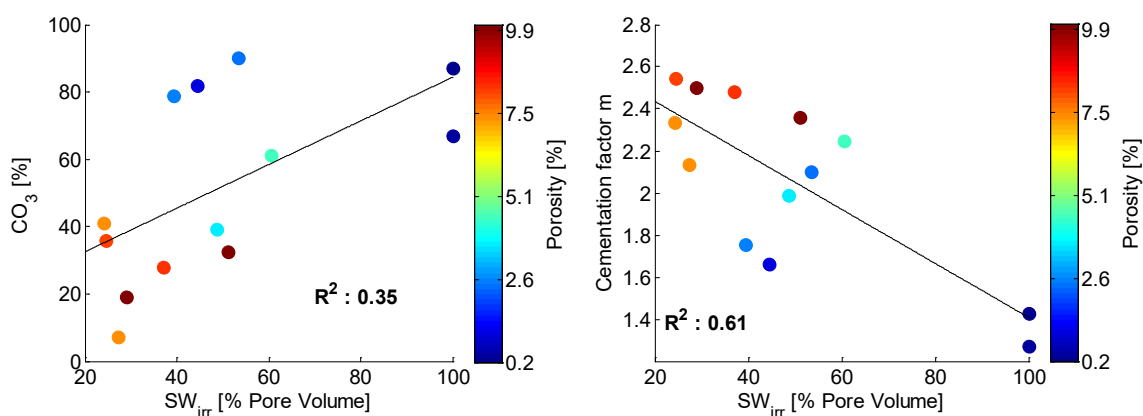


Figure 5.9: *Left: Cross-plot of irreducible water saturation ($S_{w_{irr}}$) and carbonate content (CO_3), color-coded with percentage of porosity. Higher carbonate content means higher percentage of irreducible water saturation of the total pore volume, but also lower porosity. Right: Cross-plot of $S_{w_{irr}}$ and cementation factor m , color-coded with porosity. Samples with higher fractions of $S_{w_{irr}}$ have lower cementation factors because they are less porous.*

BIB-SEM

The 23 mudrock samples analyzed with BIB-SEM are clay-rich mixed carbonate-siliciclastic rocks that contain between 0.06 – 10.15 % TOC and between 7.1 – 90.1 % CO_3 (weight %). The BIB-SEM mosaics show various clay minerals among carbonate grains,

pyrite, and organic matter (OM); this composition is in line with findings from X-ray diffraction (XRD) studies of the Vaca Muerta Formation (Vittore et al., 2014). Some examples of pyrite, kaolinite, smectite, and OM are displayed in Figure 5.10.

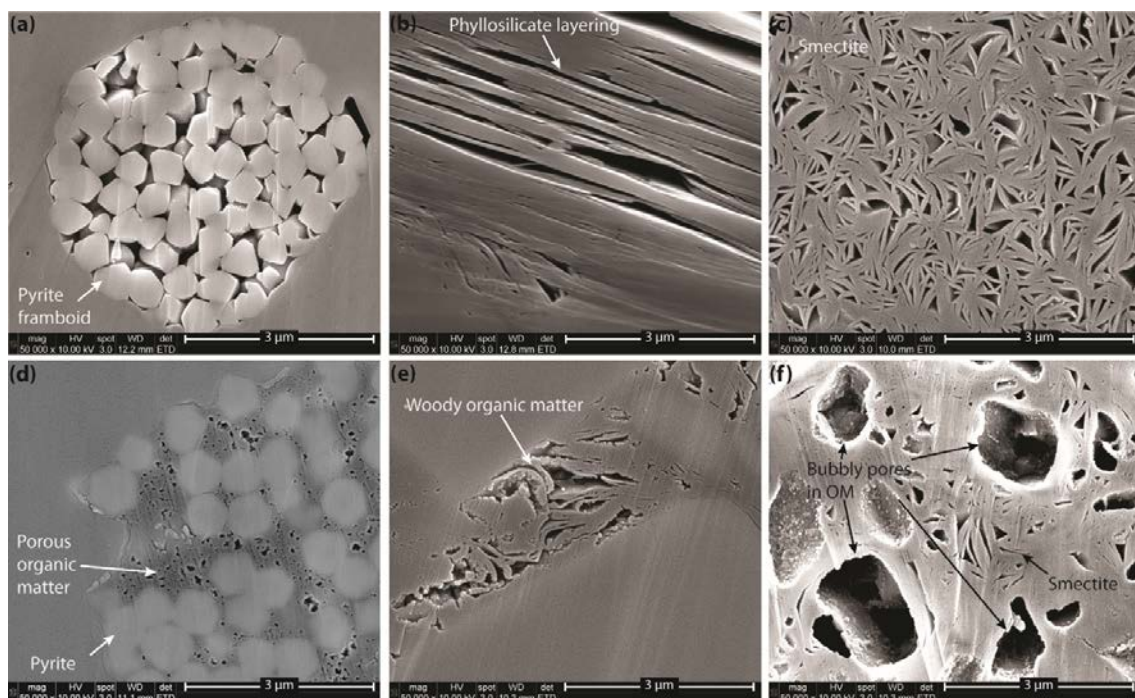


Figure 5.10: Examples of minerals and organic matter (OM) in Vaca Muerta mudrocks in broad-ion-beam milling scanning electron microscopy (BIB-SEM) images at 50,000x magnification. (a) Pyrite framboid with intercrystalline porosity. (b) Porous region in platy, sheet-like structure of kaolinite. (c) Highly porous flaky structure of smectite. (d) Mature OM associated with loosely packed pyrite framboid. (e) Woody OM between carbonate grains. (f) Highly mature OM with bubbly porosity, associated with smectite. mag = magnification; HV = high voltage; spot = electron spot size in nanometers; WD = working distance; det = detector; ETD = Everhart-Thornley detector.

Pore structure analysis

In order to study the pore geometries, mosaics are segmented into pore and solid phase so that the pore geometries can be quantified. The quantification is performed on all 23 samples, and the resulting pore geometric parameters are then related to other mineralogical and petrophysical properties (Figure 5.11).

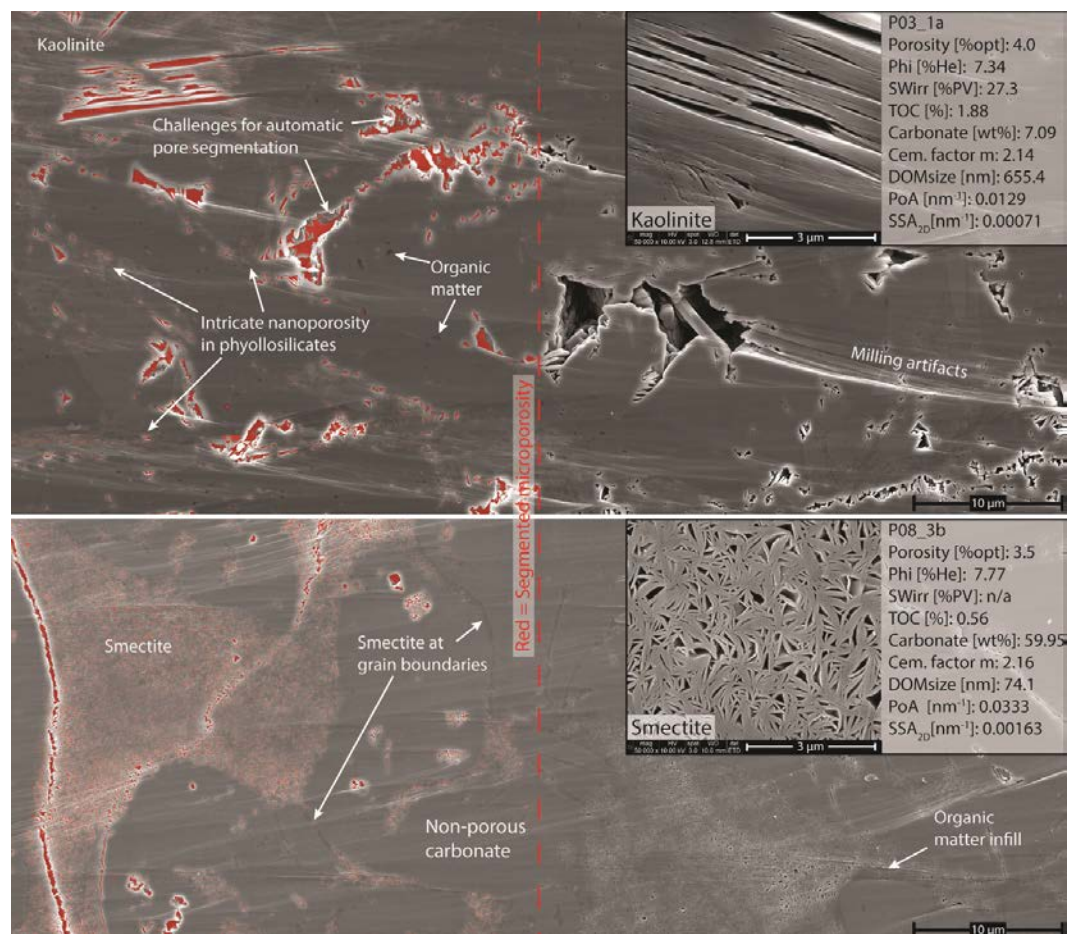


Figure 5.11: Two broad-ion-beam milling SEM mosaics consisting of 50 images each at 15,000x magnification and 9.6 nm pixel side length. The left side of the images shows segmented microporosity in red. Inserts show petrophysical and mineralogical data and zoom into clay nanoporosity at 50,000x magnification and 2.9 nm pixel side length. Near-vertical grooves are milling artifacts. Top (P03_1a): Kaolinite and large pores in probably clastic matrix. Bottom (P08_3b): Smectite matrix around large, non-porous carbonate clasts. Top and bottom samples have significantly different nanopore geometries and carbonate content, yet an equal cementation factor m . mag = magnification; HV = high voltage; $spot$ = electron spot size in nanometers; WD = working distance; det = detector; ETD = Everhart-Thornley detector.

Pore geometry parameters

The two pore geometry parameters Dominant pore size (DOMsize) and Perimeter over Area (PoA) are measured from segmented BIB-SEM mosaics. They range from 98 - 719 nm and 0.013 - 0.043 nm⁻¹, respectively. Both pore structure parameters show no correlation with cementation exponents (Figure 5.12; left). Samples with high or low

cementation factors can have both complex and simple nanopore geometry. Notably, two samples with the same cementation factor of around $m = 2.0$ (turquoise dots) plot in opposite ends of the spectrum; one has the highest DOMsize (> 700 nm) and lowest PoA, the other has low DOMsize but the most complex pore structure (PoA > 0.04 nm⁻¹).

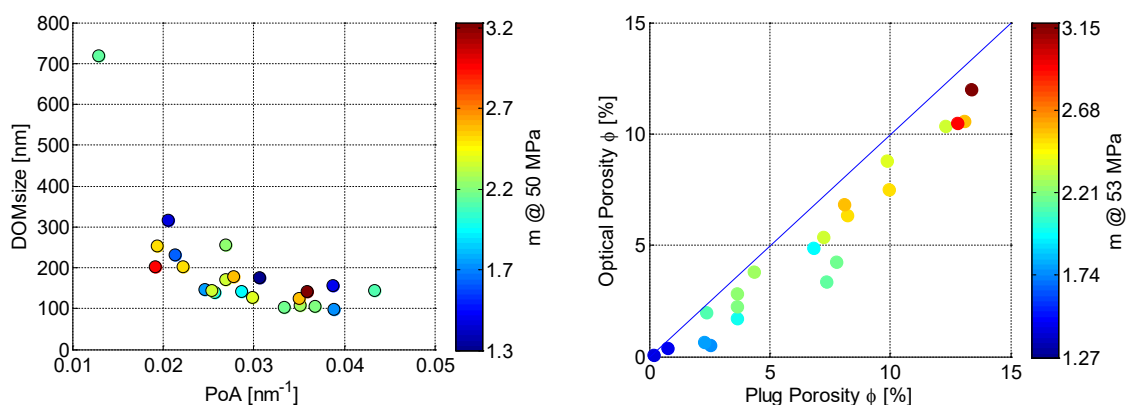


Figure 5.12: *Left: Cross-plot of Perimeter over Area (PoA) and Dominant pore size (DOMsize), color-coded with cementation exponent m . Scattered colors illustrate lack of influence of nanopore geometry on cementation factors. Right: Plug porosity vs optical porosity for the mudrock samples, color-coded with cementation factors at 53 MPa. Discrepancy between optical and plug porosity explains why the analyzed nanopore geometry does not correlate with cementation factors.*

The inconsistency between pore parameters and m is most likely due to the fact that not all porosity has been included in the pore shape analysis, i.e. the mosaics are not representative for the plug sample. The resolved and quantified image porosity (Φ_{opt}) is not equal to plug porosity, which is used to determine cementation factors (Figure 5.12; right).

2-dimensional Interfacial Surface Area (ISA_{2D})

Values for the 2-dimensional Interfacial Surface Area (ISA_{2D}) calculated with Equation 5.1 range from $4.0\text{e-}5$ – $1.6\text{e-}3$ nm⁻¹. The parameter shows only a slight association with cementation exponents, whereby samples with higher interfacial surface tend to show higher cementation factors. However, the controlling factor behind this relationship

appears to be the inherent higher porosity in samples with higher ISA_{2D} (Figure 5.13; top). The significantly lower correlation coefficient of ISA_{2D} with m ($R^2 = 0.10$) as compared to porosity with m ($R^2 = 0.72$; Figure 5.5; top) underlines this assumption. DOMsize and PoA show no correlation with cementation factor (Figure 5.13; middle and bottom).

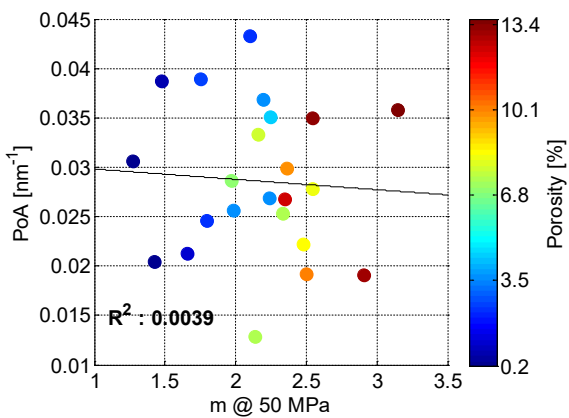
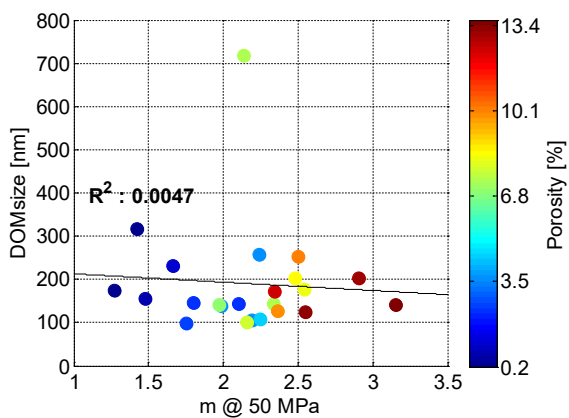
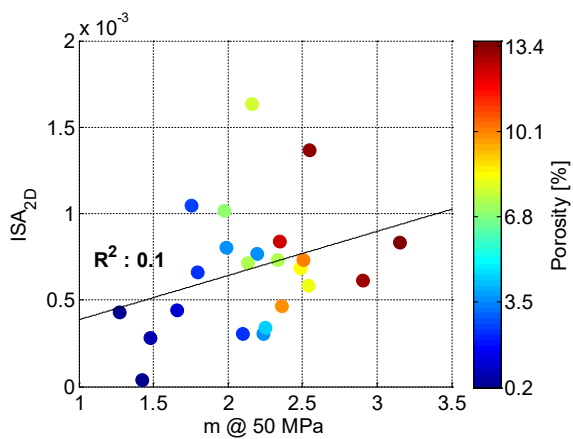
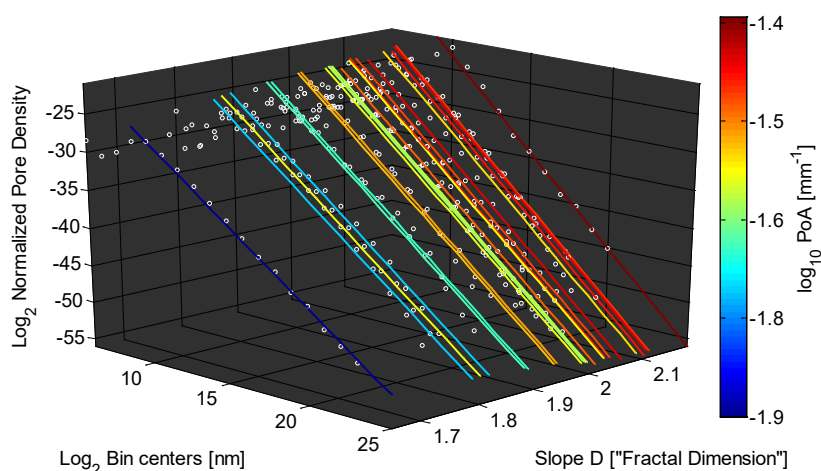


Figure 5.13: Cross-plots of cementation factor m vs pore geometry on y-axis, color-coded with porosity. Top: 2-dimensional Interfacial Surface Area (ISA_{2D}), demonstrating the slight correlation of ISA_{2D} with m . Middle and bottom: $DOMsize$ and PoA show lesser correlation with m than ISA_{2D} , which incorporates porosity.

Fractal analysis

All samples show fractal pore size distributions across the investigated length scales (9.56 nm pixel size up to mosaic size $\sim 0.012 \text{ mm}^2$) as indicated by the excellent fit of a log-log linear regression curve to the data points (Figure 5.14). The values for the fractal dimension or Slope D, extracted from this linear regression, range from Slope D = 1.55 – 2.19.

The fractal dimension is a measure of the complexity of the pore space and hence correlates well with PoA, which defines complexity by relating the pore perimeter of all pores to the combined pore area (Figure 5.14; top). However, the complexity of the nanopores does not seem to control cementation factors (Figure 5.14; bottom).



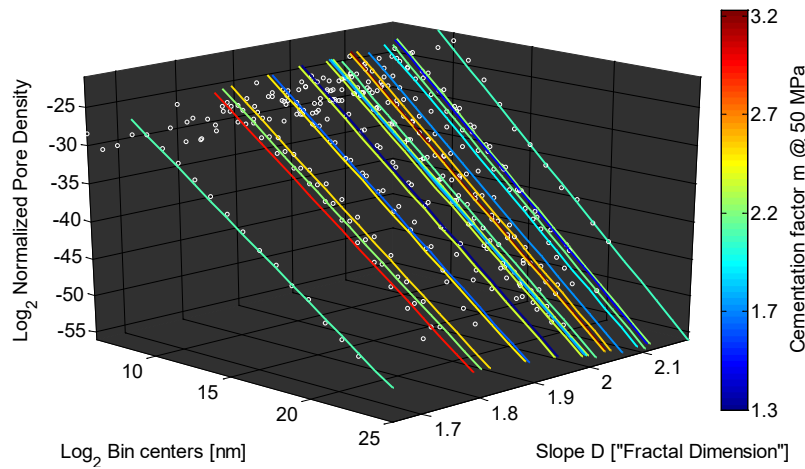


Figure 5.14: Double-logarithmic plot of pore size bin centers vs normalized pore density per bin, indicating a power-law pore size distribution. Slope D of power-law distribution or fractal dimension of pore space on Z -axis. Top color-coded with Perimeter over Area (PoA) and bottom with cementation factor m . A steeper Slope D indicates higher complexity of the pore system, which is corroborated by higher PoA-values in these samples (top). No definite trend is visible between pore structure and cementation factor (bottom).

Table 5.2. Pore geometry parameters Dominant pore size (DOMsize), Perimeter over Area (PoA), Interfacial Surface Area (ISA_{2D}), and slope of pore size distribution (Slope D) in order of ascending cementation factor (m). The pore geometry appears to have little impact on m .

Sample	m	DOMsize [nm]	PoA [nm^{-1}]	ISA_{2D} [nm^{-1}]	Slope D
06_2a	1.27	175	0.031	4.3E-04	1.94
28_2a	1.43	317	0.021	4.0E-05	1.55
11_2a	1.48	156	0.039	2.8E-04	2.11
26_2a	1.66	232	0.021	4.4E-04	1.89
24_2b	1.75	98	0.039	1.0E-03	2.06
05_2ab	1.80	145	0.025	6.6E-04	1.99
A8a	1.97	142	0.029	1.0E-03	2.09
05_2a	1.99	139	0.026	8.0E-04	1.99
31_2a	2.10	144	0.043	3.1E-04	2.19
03_1a	2.14	719	0.013	7.1E-04	1.65
08_3b	2.16	102	0.033	1.6E-03	2.01
20_2a	2.19	105	0.037	7.7E-04	2.10
A10_2a	2.24	257	0.027	3.1E-04	1.80
22_2a	2.25	108	0.035	3.4E-04	2.11
27_2a	2.33	143	0.025	7.4E-04	2.00

15_1b	2.35	171	0.027	8.4E-04	1.98
29_2a	2.36	127	0.030	4.7E-04	1.94
16_2a	2.48	203	0.022	6.8E-04	1.88
30_2a	2.50	254	0.019	7.3E-04	1.82
10_1a	2.54	177	0.028	5.8E-04	2.03
13_1b	2.55	125	0.035	1.4E-03	2.04
11_1b	2.90	203	0.019	6.2E-04	1.79
38_1a	3.15	141	0.036	8.4E-04	2.03

Discussion of cementation factors, mineralogy, and pore geometry

We will first discuss the influence of different petrophysical, physical, and mineralogical parameters on cementation exponents, and then discuss nanopore geometries as extracted from BIB-SEM mosaics.

Cementation factors

TOC & CO₃

Kerogen (TOC) content is arguably the most important factor in unconventional reservoirs, as an interval can only be considered a reservoir rock if it is rich in hydrocarbons. This study finds a positive correlation between cementation factor m and TOC content, i.e. a higher TOC content results in higher m (Figure 5.5; middle). This indicates that the OM (organic matter) in our samples is not mature enough to be conductive, unlike graphite and other highly mature OM minerals which are contributing to conductivity (Kethireddy et al., 2014; Firdaus & Heidari, 2015). Nevertheless, our samples show clear indications of maturity, e.g. bubbly porosity within the OM (Figure 5.10), and the well location where the samples are from also places the Vaca Muerta Formation in the oil window (Legarreta & Villar, 2011). Theoretically, the bubbly porosity in the OM shows geometric similarity to vuggy porosity in carbonates (Jackson et al., 1993; Verwer et al., 2011). Vuggy porosity does not contribute to electrical conductivity and would explain an increased cementation exponent.

Samples with high carbonate content (CO_3) and low amount of clay show low cementation factors (Figure 5.5; bottom). In the VMF dataset, high carbonate content is usually accompanied by low porosity (Figure 5.9; left). Low porosity in samples with high carbonate content has been reported in other shale reservoir rocks (Bustin et al., 2008). This observation contradicts the notion that only clays reduce cementation exponents due to favorable conductivity of their electrical double layer (EDL) and higher cation exchange capacity (CEC; Waxman & Smits, 1968). The low porosity is likely a more important reducer of cementation exponents (Figure 5.5 top). It indicates that a large fraction of the porosity is related to the OM, which is a common theme in mature unconventional reservoirs where the organic portion develops pores when hydrocarbons are extracted during and after maturation (Passey et al., 2010; Driskill et al., 2013; Crousse et al., 2015). Consequently, intervals with low cementation factors would indicate higher carbonate content and higher brittleness suitable for fracking-stimulated hydrocarbon extraction. However, higher carbonate content also indicates less organic matter and hence less extractable hydrocarbons (Figure 5.4).

Porosity

Porosity is high in the analyzed mudrocks with values up to 17 %, so the results may not be representative for all shale and unconventional reservoirs. Our results indicate that porosity is the dominant control on cementation factors in mudrocks because samples with higher porosity show higher cementation factors (Figure 5.5; top). This might be a result of increased rock solid phase conductivity in mudrocks due to clay and pyrite content, which both contribute to conductivity. Important factors hereby include hydroxyl layers in swelling clay minerals and increased double-layer (EDL) surface conductivity in all clay

minerals. Pyrite is a metal and itself highly conductive. Since the rock is already conductive at near-zero porosity, adding porosity consequently just increases the cementation exponent according to Archie's equation (Eq. 5.3). This is especially true since most porosity is in the OM, and appears largely unconnected (Figure 5.10d, f).

Cementation factors and pyrite

Some low-porosity samples show very low cementation exponents close to the theoretically lowest possible value of $m = 1$, which is the value for a straight tube filled with conductive brine. The extremely low values are probably the result of the high pyrite content in these samples (Figure 5.2; Figure 5.10d, e, and f). Both pyrite and the brine that fills the pore space are conductive, hence the volume of pyrite would have to be added to the porosity term in Archie's equation in order to get a reasonable result for the cementation factor (Eq. 5.3). Disregarding the pyrite volume leads to an underestimation of the conductive portion and cementation factors (Clennell et al., 2010; Passey et al., 2010; Kethireddy et al., 2014).

Pressure dependency of cementation factors

All measured mudrock samples show pressure dependency of electrical conductivity and resulting cementation factors (Figure 5.6). This is due to the compression of the plug in a higher stress regime. With increasing pressure, micro- and nanopores of the intricate mudrock pore system would narrow down or close completely, which leads to a decrease in conductivity. Even if the pore network connectivity was not affected, a compression of the plug samples would lead to lower porosity values than those measured on the core plugs beforehand and used as input for the calculation of the cementation exponents with Archie's equation (Eq. 5.3).

The high compressibility of the mudrock samples, which contain clays and organic material, might be due to the swelling of clay minerals during saturation with brine (Garcia et al., 2013). This would allow for compression during pressurization, as swollen clays are comparatively easy to dehydrate and re-compact. Thus, the log calibration in mudrocks requires the adjustment of plug confining and pore pressure to reservoir conditions, i.e. the right pressure according to the depth the sample was taken from.

All samples show a hysteresis effect at 5 MPa in cementation factor measurements before and after the 50 MPa pressure sweep (Figure 5.7, 5.8). This "memory effect" implies that either the porosity of the sample or the internal pore geometry and connectivity has been changed permanently. However, in the experiment the rocks are given little time to relax after the pressure sweep, hence it is not clear if the change is more temporarily than permanent. A permanent change in porosity is unlikely because the plug samples are from more than 2,500 meters depth, so their porosity should not be permanently altered by 50 MPa measurements (roughly equivalent to 2,000 m overburden). It is more likely that the pore connectivity has been changed, as the micro- and nanopores tend to have miniscule pore throats that get occluded or closed easily. However, blocked pore connections also would lead to a small decrease in overall porosity, so the hysteresis effect is most likely a combination of both change in porosity and pore connectivity. The porosity is not measured during the pressure increase, as only the length but not the circumference of the plug can be monitored.

Micropores and Sw_{irr}

Humidity-drying methods on 13 samples enables assessment of the amount of microporosity, also referred to as ineffective porosity in terms of hydrocarbon

producibility. Electrical conduction is favored by a small and intricate pore system with a large number of pores (Verwer et al., 2011; Norbistrath et al., 2015). Thus, if a higher percentage of the brine is contained in micropores, it will add substantially to electrical conduction and hence lower cementation factors. Consequently, the finding that samples with higher Sw_{irr} show lower cementation factors (Figure 5.9; right) implies an intricate pore network that is well connected at the micropore scale. This corroborates previous work and the theory of electrical efficiency, where surface conductivity plays a large role and most of the macropore volume is considered to be electrically dead volume (Herrick & Kennedy, 1994; Abousrafa et al., 2009). A higher Sw_{irr} would indicate less macropore volume and more effective surface conduction.

Another interesting finding is that samples with the highest irreducible water saturation (Sw_{irr}) also had the highest amount of carbonate content (Figure 5.9; left). This is counterintuitive as clays are usually considered to contain most of the irreducible water, either as part of their hydrated mineral structure or in ionic bonds with their electric double layer (EDL) (Passey et al., 2010). The EDL is related to the high Interfacial Surface Area (ISA_{2D}) of clay microporosity (Figure 5.15, 5.17). However, samples with highest carbonate content also showed the least amount of overall porosity, which increases the effect of a small amount of irreducible water on Sw_{irr} .

Sw_{irr} and CRS

Samples with high Sw_{irr} show high reactance values (Figure 5.22; bottom right). This is in accordance with the notion that interfacial polarization leads to phase shifts in the low-frequency spectrum (Cerepi, 2004; Hizem et al., 2008). Higher Sw_{irr} indicates larger Interfacial Surface Area and hence higher interfacial polarization effects due to higher

retention of adsorbed water on clay surfaces (Bush & Jenkins, 1970). However, the findings related to the irreducible water saturation are limited by the small number of analyzed samples, and further work is required to establish the reliability of the results and effects of $S_{w_{irr}}$ on CRS.

BIB-SEM

Broad-ion-beam milling scanning electron microscopy (BIB-SEM; Figure 5.3) allows to image and quantify micro- and nanopore structures in mudrocks (Figure 5.11). We have applied the BIB-SEM method to 23 mudrock samples in this study, where the findings add to a growing body of literature on nanopore geometries in unconventional rocks (Curtis et al., 2010; Desbois et al., 2011; Driskill et al., 2013; Hemes et al., 2015; Klaver et al., 2015a,2015b). In addition, an attempt is made to identify their effects on flow and storage in unconventional rocks (Figure 5.12, 5.13, 5.14, and 5.15).

Nanopore geometry

One key outcome of this study is that the nanopore geometry does not exert a strong control on electrical rock properties like cementation factor (Figure 5.12; left) or complex resistivity spectra (Figure 5.21; middle and right). For example, the DIA-derived pore geometry parameters DOMsize and PoA show no correlation with CRS. Instead, the amount of plug porosity determines the cementation exponent in mudrocks (Figure 4; top) and controls the resistivity spectra (Figure 5.20; left). The 2-dimensional Interfacial Surface Area (ISA_{2D}), which is deemed to be the primary control on low-frequency dielectric rock properties, appears to be only a secondary control on CRS (Figure 5.21; left).

Fractals

A common theme in all natural rocks is the power-law distribution of pore sizes; not only for shales (Clarkson et al., 2013; Hemes et al., 2015; Klaver et al., 2015b) but also in siliciclastic (Katz & Thompson, 1985; Krohn, 1988; Pape et al., 1999) and carbonate rocks (Mazzullo et al., 1996; Norbistrath et al., 2015; Purkis et al., 2015).

This mudrock study finds a power-law distribution of pore sizes across the investigated scales, indicating a fractal scaling of pore sizes, which implies self-similarity of the pore space and predictability of pore sizes outside the investigated length scales. However, the magnitude of scales and the resolution pose some challenges. For example, for the extremely small pore sizes there are apparent kinks in the distribution that deviate from a log-log linear behavior (Figure 5.14). These kinks are likely the result of the resolution limit that fails to properly resolve the size of pores that approximate 1-4 pixels. Previous multiscale analyses further strengthen this assumption, as they found similar kinks in results from lower-resolution BIB-SEM mosaics, yet results from overlapping, higher-magnification mosaics still showed the power law in place. In rocks with both macro and microporosity a multiscale approach conforms a powerlaw distribution (Norbistrath et al., 2015). In mudrocks, the multiscale approach is not possible because they mostly contain nanoporosity. On the other hand, mudrock pore structure can accurately be represented by single-magnification BIB-SEM mosaics, although the analyzed area and covered pore sizes are relatively small.

Mudrock vs. carbonate nanoporosity

Comparing mudrocks to carbonates in a cross-plot of the amount of interfacial surface (ISA_{2D}) per percent of optical porosity (Φ_{opt}), it is apparent that mudrocks have by far more complex nanopores than previously analyzed carbonates (Figure 5.15; Norbistrath et

al., 2015). With increasing optical porosity, the amount of interfacial surface in the mudrocks increases faster than in the carbonates, which implies that their pores are more complex.

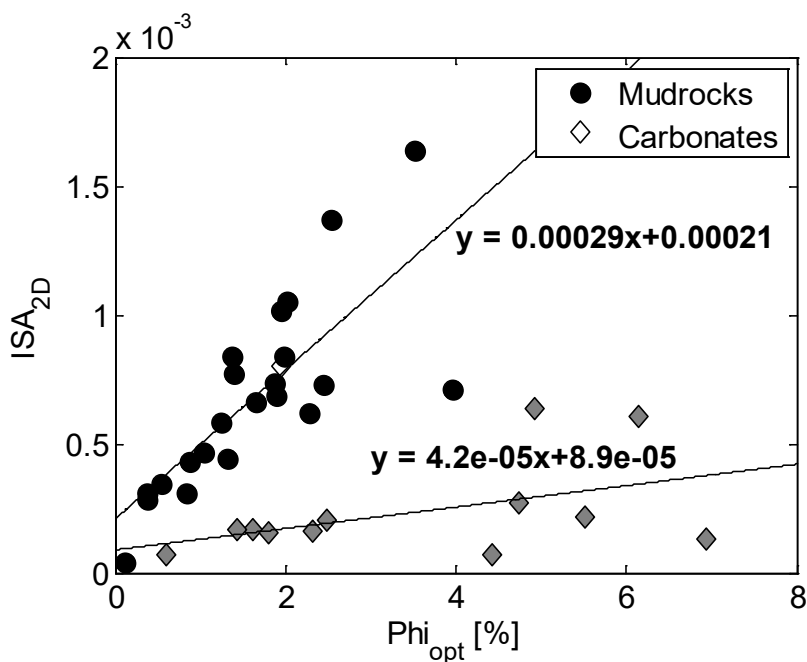


Figure 5.15: Cross-plot of optical porosity (Φ_{opt}) from BIB-SEM mosaics vs 2-dimensional Interfacial Surface Area (ISA_{2D}) indicating the higher complexity of nanoporosity in mudrocks as compared to carbonates. Mudrocks have more Interfacial surface per percent porosity. Linear equations ($y=mx+b$) shown for individual datasets.

The difference in nanopore geometry can also be seen when plotting both carbonate and mudrock datasets on a single PoA-DOMsize plot (Figure 5.16). There is no significant trend between nanopore complexity and cementation factors. Samples with higher m in warmer colors can have both small and complex or large and simple pores.

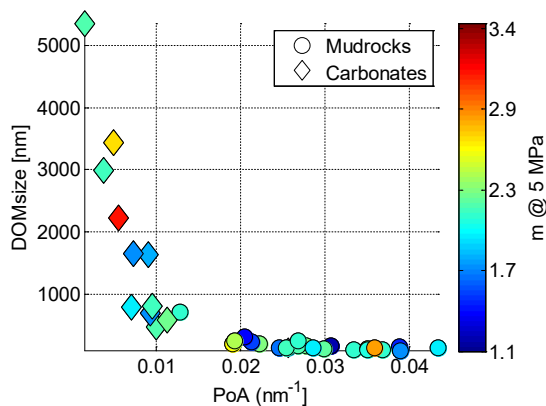


Figure 5.16: Cross-plot of Perimeter over Area (PoA) vs Dominant pore size (DOMsize) for both carbonates and mudrocks with color-coded m . Cementation factor m is from 5 MPa measurements.

It is well known that mudrocks contain a very intricate pore system (Curtis et al., 2010; Desbois et al., 2011). The increased complexity of the pore space in mudrocks is illustrated by a comparison of a typical microporous region in a carbonate and a mudrock (Figure 5.17). The mudrock consists of more numerous and intricate nanopores, mostly associated with clays and organics, whereas the carbonate shows few, mostly intergranular pores. Mudrocks show a much higher amount of ISA_{2D} per percent of porosity (Figure 5.15), and also much lower DOMsize and higher PoA than the carbonate rocks (Figure 5.16).

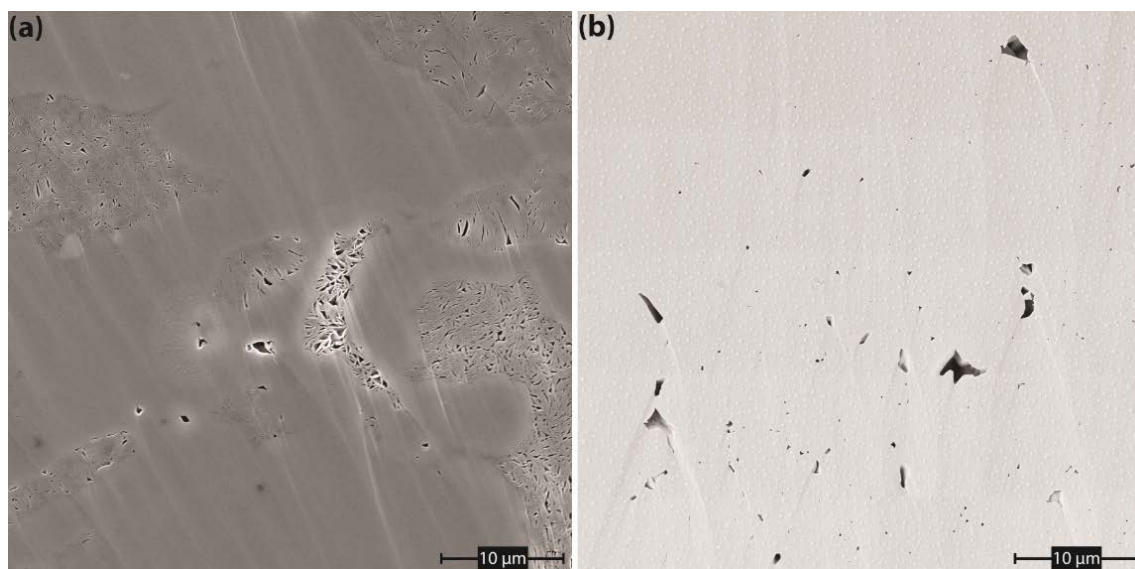


Figure 5.17: Comparison of pore geometry in a (a) mudrock and (b) carbonate sample with equal helium porosity of ~3.6 %, illustrating the increased nanopore complexity of a typical mudrock.

One theory is that the nanopores in clays and their increased surface area has great impact on low-frequency electrical flow properties (Cerepi, 2004; Hizem et al., 2008; Bean et al., 2013). The results of this study, however, indicate that the nanopore geometry cannot fully explain the electrical behavior of a rock (Figure 5.16; Figure 5.21; middle and right; Figure 5.25; middle). Mineralogy in mudrocks (Figure 5.10) has great impact on cementation factor and CRS (Figure 5.5).

Limitations in the pore geometry analysis on BIB-SEM images

In the presented analysis the measurements of complex resistivity from relatively large 1-inch core plug are correlated to pore structural parameters gathered from miniscule BIB-SEM mosaic areas averaging 0.012 mm^2 (about $12,000 \text{ }\mu\text{m}^2$) in size. Although the mudrocks are fairly homogeneous, these small areas are potentially not representative for the entire plug. However, the fact that correlations exist between CRS and ISA_{2D} that is

also determined from the BIB-SEM mosaic areas indicates the existence of a fundamental relationship.

Complex resistivity spectra (CRS)

Dispersion phenomena of amplitude and phase shifts (CRS) of low-frequency alternating electric current applied to a rock sample reflect on the internal geometry of the sample, as they are mostly influenced by electrical double layer effects that occur on the surface of the pore system, i.e. the interface between pore fluid and solid phase. Thus, interfacial polarization at the rock-fluid boundary is deemed to be the controlling factor on low-frequency dispersion (Slater et al., 2006; Ellis & Singer, 2009; Wang & Poppit, 2013) (Figure 5.1). CRS in the mudrocks show a distinct frequency dispersion that can be correlated to various petrophysical, pore geometrical, and mineralogical parameters.

Frequency range and slopes

We find the most diversity of frequency dispersion and hence discriminability between samples in the 10 – 100 kHz range (Figure 5.18). Therefore, we use this range to fit linear equations (dashed lines) for extraction of the slope parameters $\beta_{\text{amplitude}}$ and β_{phase} , which are also used for predictions of various parameters. The frequency dispersion is most likely not a result of the interfacial polarization alone, however, it enables predictions of pore geometry related parameters with high correlation coefficients.

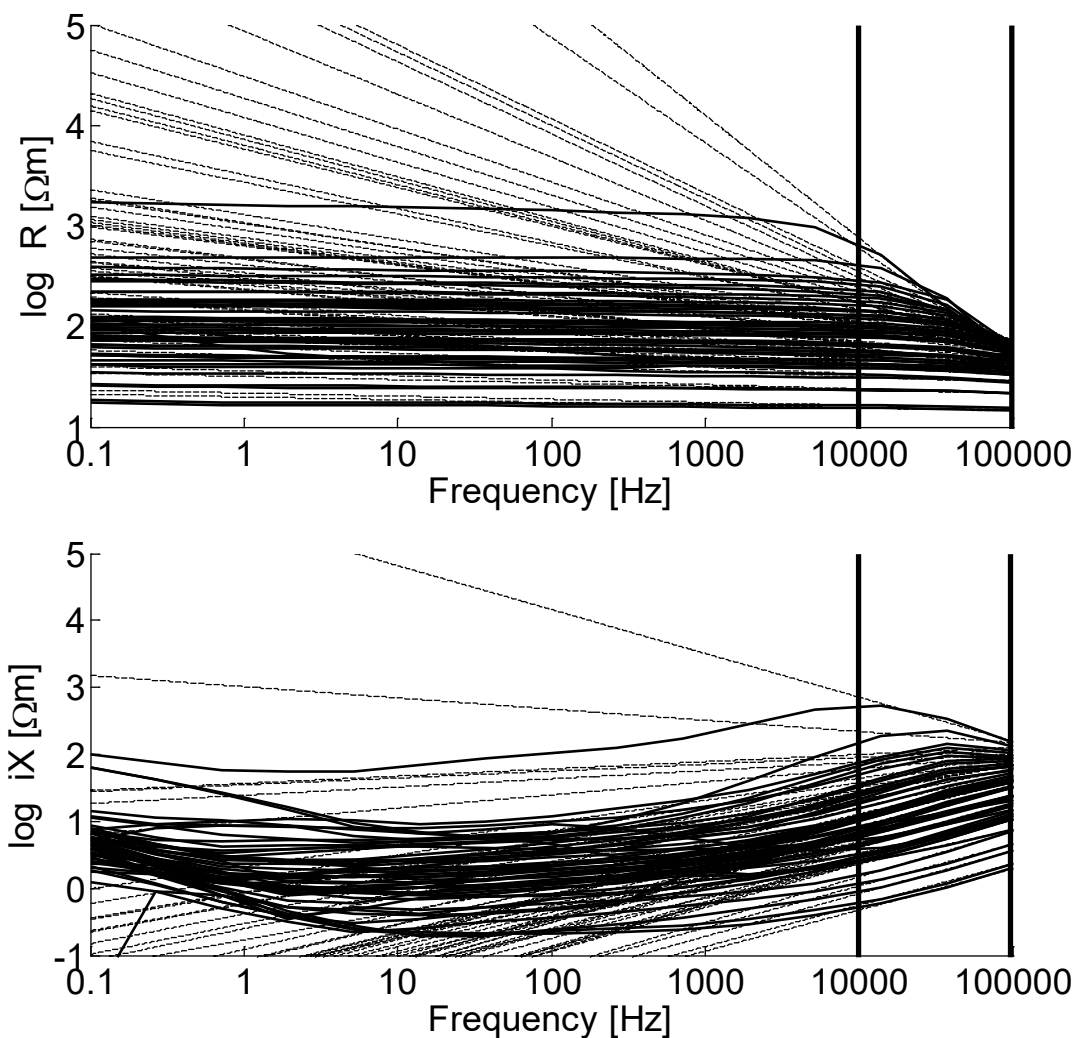


Figure 5.18: Plot of frequency vs resistivity amplitude (resistance R ; top) and resistivity phase (reactance iX ; bottom). Vertical thick lines indicate 10 – 100 kHz fitting range for extraction of CRS slope parameters. Dashed lines are fitted curves of $\beta_{\text{amplitude}}$ (top) and β_{phase} (bottom).

The extracted slope parameters $\beta_{\text{amplitude}}$ and β_{phase} of the 10 – 100 kHz range show a distinct correlation between each other (Figure 5.19). A sample that has higher $\beta_{\text{amplitude}}$ also has higher β_{phase} . The sample with lowest $\beta_{\text{amplitude}}$ (< -1.0) has also the lowest β_{phase} (< -0.5). This sample (28_2a) corresponds to the topmost dashed line (most negative slope) in Figure 5.18; top and bottom. It has a very high carbonate content of 87.2 % and very low cementation factor of $m = 1.43$.

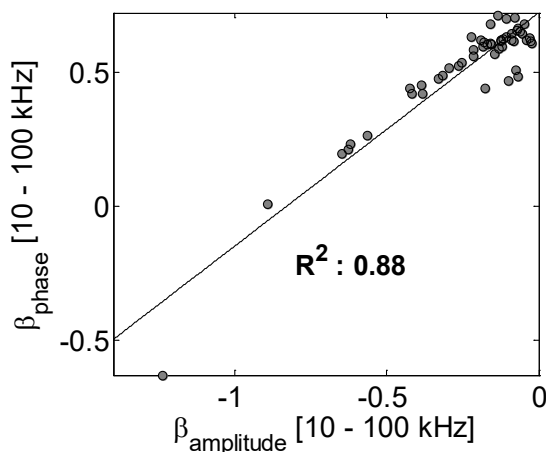


Figure 5.19: Correlation between the slope of phase and amplitude frequency dispersion of 56 mudrock samples in 10 – 100 kHz range ($\beta_{\text{amplitude}}$ and β_{phase}).

CRS slopes vs porosity and Formation Factor

The best correlation found between CRS and other petrophysical parameters is with porosity and Formation Factor (FF). Color-coding CRS curves with porosity reveals that higher porosity samples (> 12 %) have lower and less variable resistance curves (R; Figure 5.20; top left), and show a distinct increase in reactance in the 10 – 100 kHz range (iX; Figure 5.20; bottom left). Samples with high Formation Factors FF (> log FF = 3), on the other hand, show a significant decrease in resistance (R; Figure 5.20; top right) and high reactance (iX; Figure 5.20; bottom right).

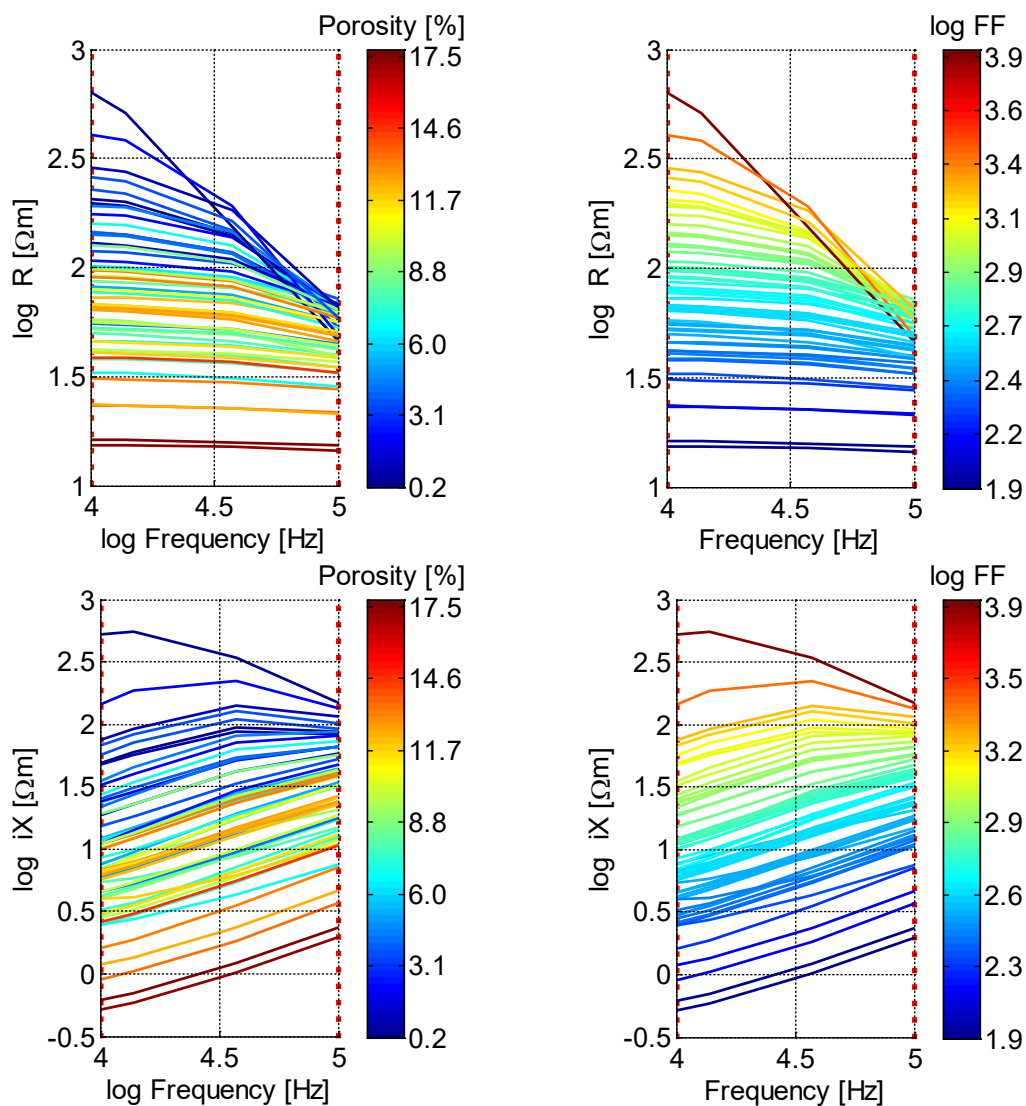


Figure 5.20: Complex resistivity spectra (top: resistance R ; bottom: reactance iX) in the 10 – 100 kHz range, color-coded with porosity (left) and Formation Factor (right). Higher porosity results in lower resistivity and distinct increase in reactance, while samples with higher Formation Factor show distinct decrease in resistance and reactance.

CRS slopes vs ISA_{2D} , DOM_{size} , and PoA

Color-coding the CRS with the amount of Interfacial Surface Area (ISA_{2D}) shows a similar yet weaker trend than with porosity (Figure 5.20; left).

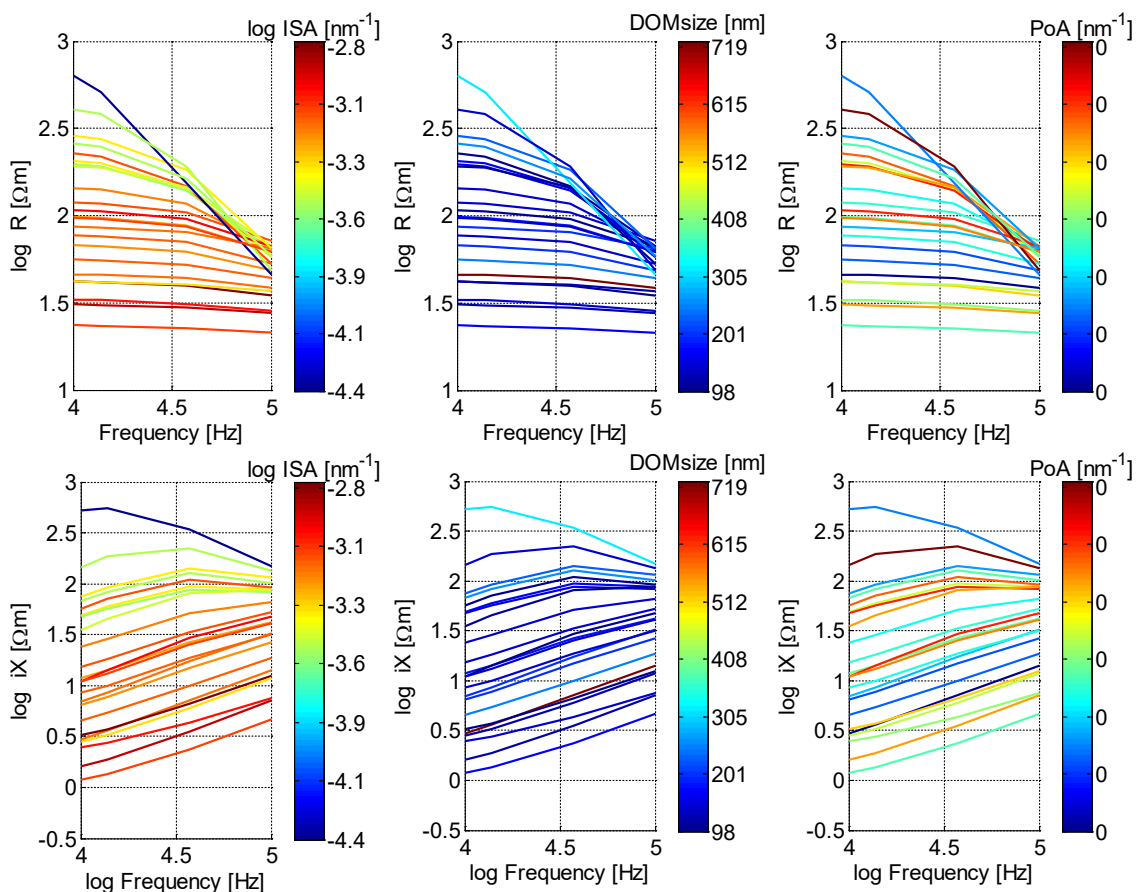


Figure 5.21: Complex resistivity spectra (top: resistance R ; bottom: reactance iX) in the 10 – 100 kHz range, color-coded with amount of Interfacial Surface Area (ISA_{2D} ; left), Dominant pore size ($DOMsize$; middle), and Perimeter over Area (PoA ; right). $DOMsize$ and PoA show little correlation with CRS, but ISA_{2D} shows trend of higher resistance (R) and reactance (iX) with less surface area.

Samples with higher ISA_{2D} , similar to samples with higher porosity, generally show less pronounced CRS dispersion in the 10 – 100 kHz range. $ISA_{2D} > 3.0 \text{ nm}^{-1}$ results in flat resistance curves (R ; Figure 5.21; left top) and lower reactance (iX ; Figure 5.21; left bottom). Purely pore-geometric parameters $DOMsize$ and PoA , on the other hand, display little correlation with CRS as no clear zonation according to $DOMsize$ or PoA is visible (Figure 5.21; middle and right).

CRS slopes vs TOC, CO₃, and Sw_{irr}

Color-coding CRS slopes with mineralogy parameters produces mixed results. Total organic carbon (TOC) has the least visible correlation with CRS. Samples with highest TOC values (> 7 % TOC) plot in the middle of both resistance and reactance spectra (Figure 5.22; left). Carbonate content (CO₃) and irreducible water (Sw_{irr}), on the other hand, show clear trends; samples with higher values (> 60 % CO₃ & > 80 % Sw_{irr}) have higher resistance and reactance (Figure 5.22; middle and right).

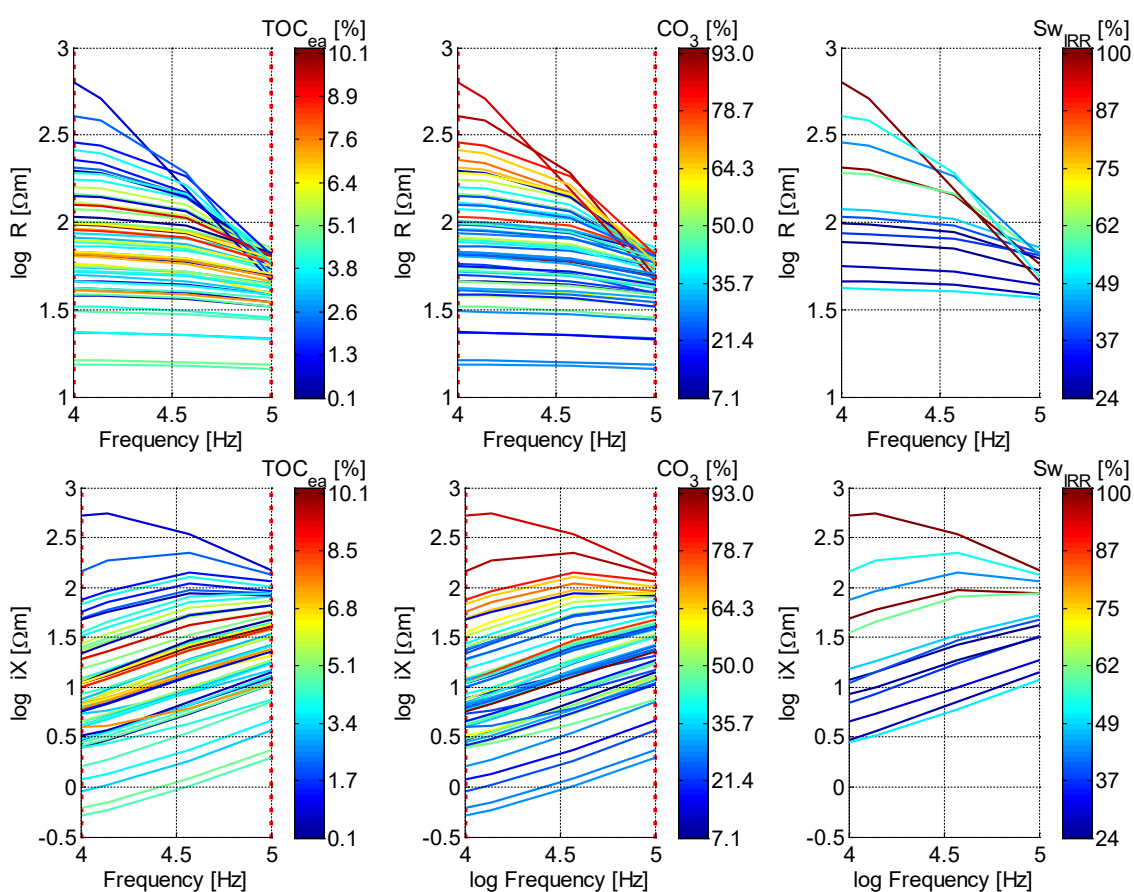


Figure 5.22: Complex resistivity spectra (top: resistance R ; bottom: reactance iX) in the 10 – 100 kHz range, color-coded with amount of total organic carbon (TOC; left), carbonate content (CO₃; middle), and irreducible water saturation on a subset of 13 samples (Sw_{irr}; right).

Predictions of TOC, CO₃, S_w_{irr}

In this section the results are shown from prediction models for total organic carbon (TOC), carbonate content (CO₃), and irreducible water saturation (S_w_{irr}) that use either just CRS slope parameters as input, or models that further incorporate porosity.

Results for predictions from a simplified model (Equation 5.6) that uses only CRS slopes $\beta_{\text{amplitude}}$ and β_{phase} as input (Figure 5.23; top row) are presented first:

$$X_{\text{estimated}} = a \beta_{\text{phase}}^b \beta_{\text{amplitude}}^c \quad \text{Eq. 5.6}$$

Results from Equation 5.6 are then compared to predictions of TOC, CO₃, and S_w_{irr} using Equation 5.7 with porosity (Φ) as additional input parameter (Figure 5.23; bottom row).

$$X_{\text{estimated}} = a \Phi^b \beta_{\text{phase}}^c \beta_{\text{amplitude}}^d \quad \text{Eq. 5.7}$$

Using Equation 5.7, the method achieves a high correlation coefficient of $R^2 = 0.79$ when predicting the irreducible water saturation S_w_{irr} in 13 humidity-dried samples (Figure 5.23; bottom right). However, this is only slightly better than predictions from CRS alone with $R^2 = 0.73$ using Equation 5.6 (Figure 5.23; top right). Similarly, predictions of carbonate content (CO₃; Figure 5.23; middle) are not greatly enhanced by inclusion of porosity, from $R^2 = 0.46$ to and $R^2 = 0.49$.

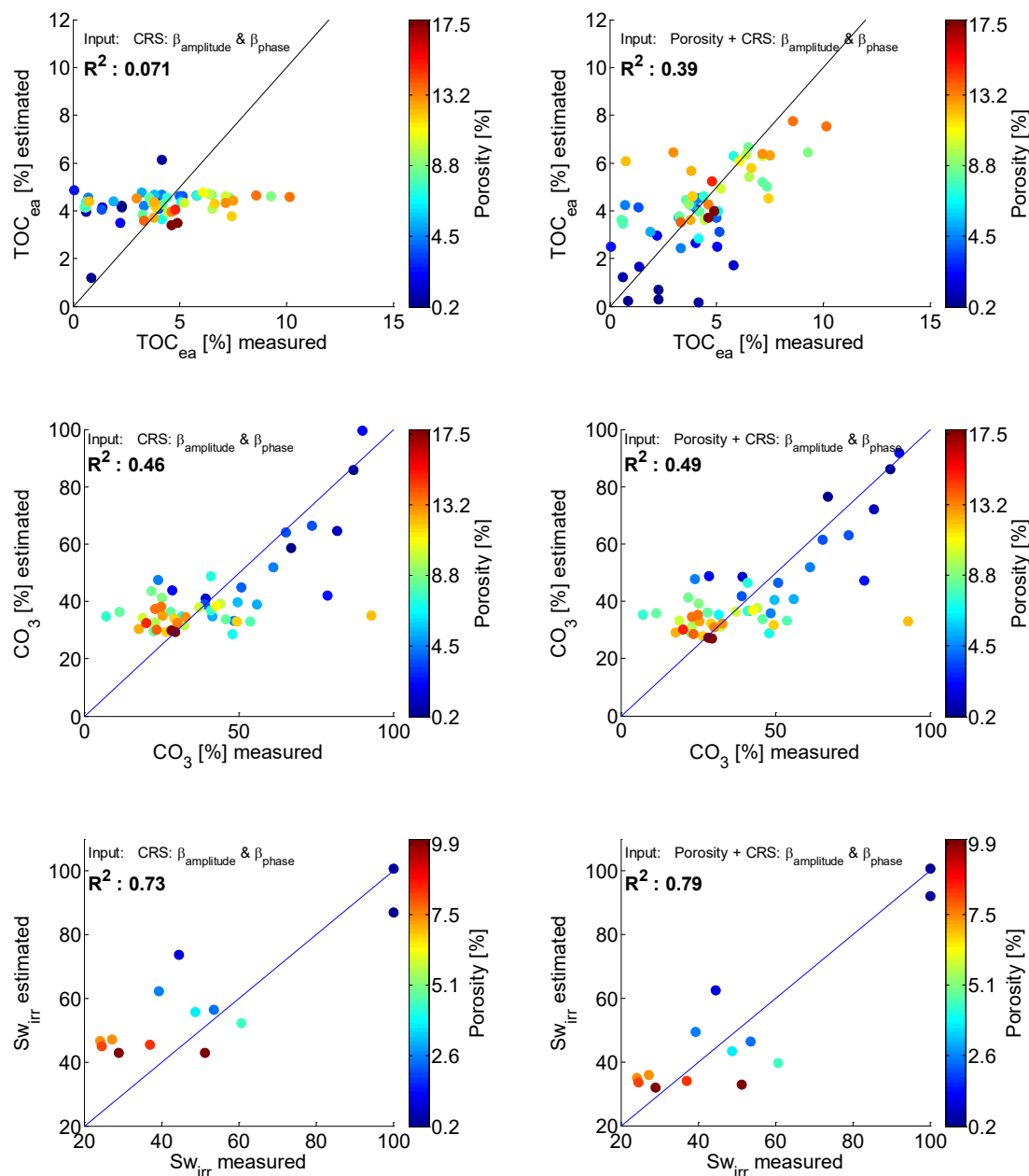


Figure 5.23: Predictions of total organic carbon (TOC; top), carbonate content (CO₃; middle), and irreducible water saturation (Sw_{irr}; bottom) from CRS parameters $\beta_{\text{amplitude}}$ and β_{phase} alone using Equation 5.6 (left) and including porosity using Equation 5.7 (right). All predictions gain in accuracy from inclusion of CRS parameters.

On the other hand, predictions of total organic carbon (TOC; Figure 5.23; left) are improved by inclusion of porosity data using Equation 5.7, from $R^2 = 0.07$ to $R^2 = 0.39$. TOC apparently does not correlate with CRS parameters.

Predictions of porosity and ISA_{2D}

In this section we show the results from prediction models of porosity and 2-dimensional Interfacial Surface Area (ISA_{2D}) on a subset of 23 samples that were analyzed with the BIB-SEM method. A simplified model that only use resistivity (R_f) as input parameter (Figure 5.24; top) in Equation 5.8

$$X_{\text{estimated}} = aR_f^b \quad \text{Eq. 5.8}$$

shows lesser correlation coefficients than predictions that incorporate CRS slope parameters $\beta_{\text{amplitude}}$ and β_{phase} (Figure 5.24; bottom) using Equation 5.9

$$X_{\text{estimated}} = aR_f^b \beta_{\text{phase}}^b \beta_{\text{amplitude}}^d \quad \text{Eq. 5.9}$$

Correlation coefficients are better for predictions of porosity ($R^2 = 0.71$) than for predictions of ISA_{2D} ($R^2 = 0.59$; Figure 5.24). This is probably related to the fact that ISA_{2D} is partially controlled by the complexity of the pore space. The good correlation coefficients that CRS parameters achieve for predictions of porosity leads to the conclusion that porosity is the main control on frequency dispersion of CRS in the frequency range from 10 – 100 kHz.

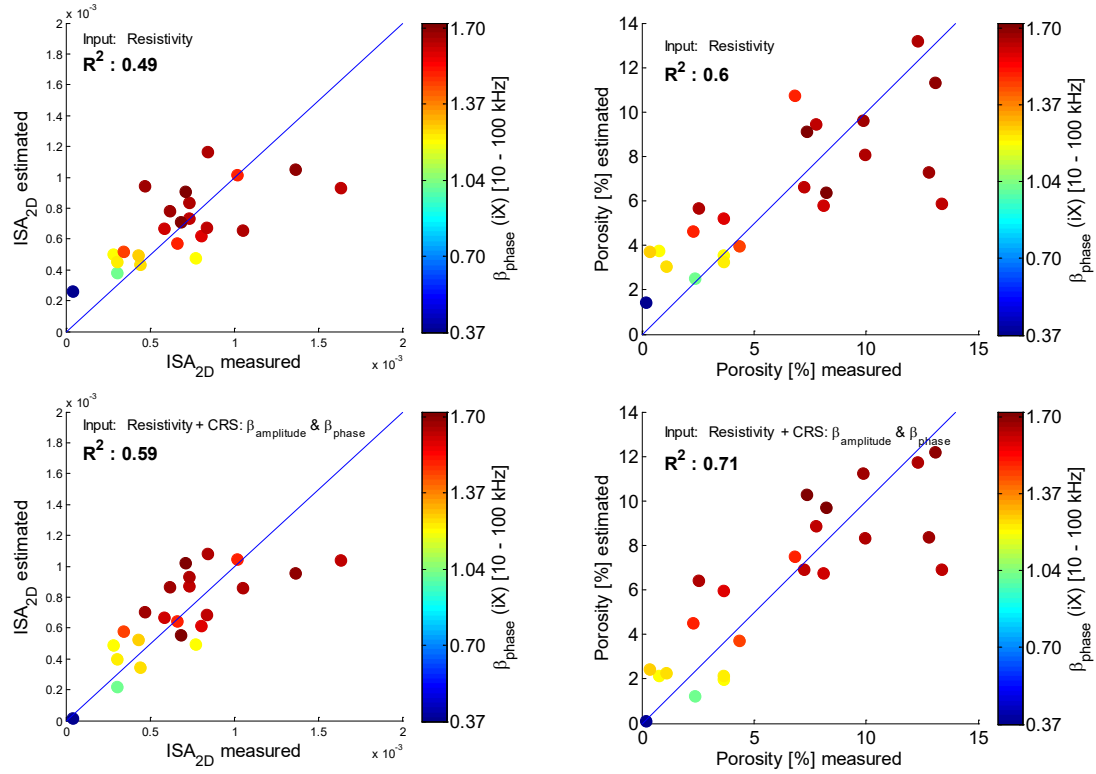


Figure 5.24: Predictions of 2-dimensional Interfacial Surface Area (ISA_{2D} ; left) and porosity (right) from resistivity alone using Equation 5.8 (top) and including CRS parameters $\beta_{amplitude}$ and β_{phase} using Equation 5.9 (bottom). Both predictions gain in accuracy from inclusion of CRS parameters.

Predictions of cementation factors

Predictions of cementation factors (m) are made on a subset of 23 samples that were analyzed with the BIB-SEM method. We use three different equations (5.10, 5.11, and 5.12) that use different input parameters. The first one uses only porosity as input (Equation 5.10):

$$m_{estimated} = a\phi^b \quad \text{Eq. 5.10}$$

The second uses nanopore geometry parameters DOMsize and PoA from BIB-SEM analysis as additional input (Equation 5.11):

$$m_{estimated} = a\phi^b \text{DOMsize}^c \text{PoA}^d \quad \text{Eq. 5.11}$$

For the third equation, we replace DIA parameters $DOMsize$ and PoA with $\beta_{amplitude}$ and β_{phase} from CRS measurements (Equation 5.12):

$$m_{estimated} = a\phi^b \beta_{phase}^c \beta_{amplitude}^d \quad \text{Eq. 5.12}$$

The comparison of results from models with DIA or CRS input parameters (Eq. 5.11 and Eq. 5.12) is done to test the applicability of CRS as a parameter that can describe the pore geometry and electrical flow properties.

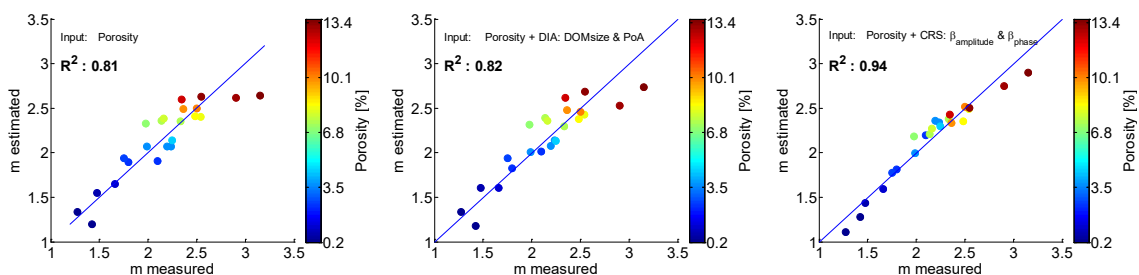
Porosity as sole input parameter (Eq. 5.10) already enables predictions of cementation exponents with $R^2 = 0.81$ (Figure 5.25; top left). Incorporating nanopore geometry parameters from BIB-SEM DIA into the predictions using Equation 5.11 does not significantly improve estimates with $R^2 = 0.82$ (Figure 5.25; top middle). However, incorporating CRS information gives significantly better results with a correlation coefficient of $R^2 = 0.94$ (Figure 5.25; top right). Predictions from DIA parameters alone (Equation 5.13):

$$m_{estimated} = aDOMsize^b PoA^c \quad \text{Eq. 5.13}$$

show weak correlation coefficients of $R^2 = 0.053$ (Figure 5.25; bottom left). Predictions from CRS parameters alone (Equation 5.14)

$$m_{estimated} = a\beta_{phase}^b \beta_{amplitude}^c \quad \text{Eq. 5.14}$$

show better correlation coefficients of $R^2 = 0.35$ (Figure 5.25; bottom right).



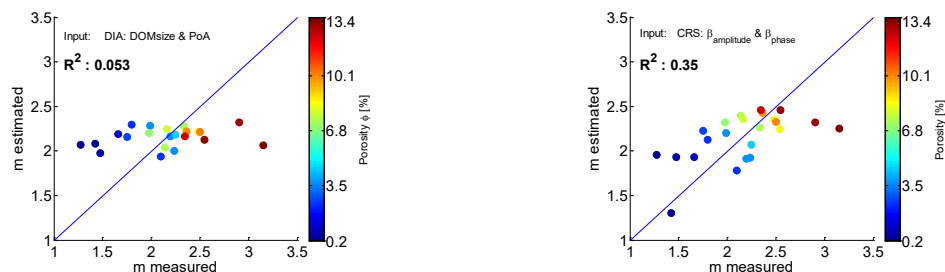


Figure 5.25: Predictions of cementation factor m from porosity using Equation 5.10 (top left), porosity and DIA parameters using Equation 5.11 (top middle), and from porosity and CRS slopes using Equation 5.12 (top right). The plot demonstrates that nanopore geometry has little influence on cementation factors, while CRS parameters evidently are highly related to m . Bottom row shows prediction just from DIA parameters (bottom left) using Equation 5.13 and predictions just from CRS parameters (bottom right) using Equation 5.14.

This underlines the strong connections between the frequency dispersion of CRS and Formation Factors in this dataset (Figure 5.20; right), which allows for predictions of cementation factors in mudrocks with a universal equation (Equation 5.15):

$$m_{\text{estimated}} = 1.71\phi^{0.31}\beta_{\text{phase}}^{-0.20}\beta_{\text{amplitude}}^{0.10} \quad \text{Eq. 5.15}$$

Similarly, predictions of cementation factors on the entire dataset of 56 core plugs using Equations 5.10 and 5.12 show significant gain in correlation from inclusion of CRS parameters (Figure 5.26). Using only porosity as input, the method achieves a correlation coefficient of $R^2 = 0.76$, but including CRS parameters improves it to $R^2 = 0.95$. Using Equation 5.15, with the constants $abcd$ determined on the smaller BIB-SEM dataset, the method still achieves a correlation coefficient of $R^2 = 0.94$. The high correlation coefficient underlines the general applicability of Equation 5.15 for predictions of cementation factors in mudrocks.

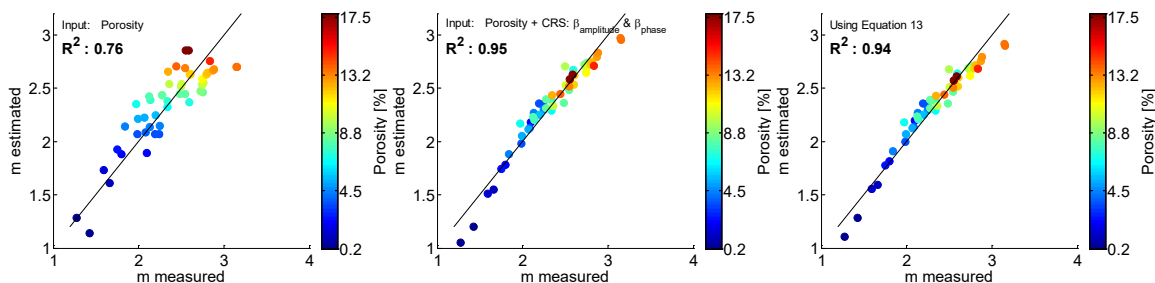


Figure 5.26: Predictions of cementation factor m in 56 mudrock core plug samples from porosity using Equation 5.10 (left), from porosity and CRS slopes using Equation 5.12 (middle), and using Equation 5.15 that was defined on a smaller subset of 23 BIB-SEM samples (right). Inclusion of CRS parameters drastically improve predictions of cementation exponents, even with a model that has been defined on a smaller subset.

For the subset of 23 BIB-SEM samples, the predictions of cementation exponents from CRS and porosity achieve $R^2 = 0.94$ (Figure 5.25; right). This is a significant improvement over predictions from a model that uses only porosity as input with an $R^2 = 0.81$ (Figure 5.25; left), or a model that uses pore geometry parameters DOMsize and PoA and porosity (Figure 5.25; middle). For the entire dataset of 56 core plugs, correlation coefficients for predictions of cementation exponents from porosity alone achieve $R^2 = 0.76$ (Figure 5.26; left) and with CRS parameters $R^2 = 0.95$ (Figure 5.26; middle).

Discussion of CRS

Pore geometry and porosity

Recent studies of dielectric dispersion properties discuss the importance and difference between the *specific surface area per unit mass* (S_m) compared to the *surface to pore volume ratio* (S_{por}) (Revil, 2012; Weller & Slater, in press). These studies estimate specific surface properties from volumetric adsorption experiments using different gases. In this study, we assess specific surface parameters from direct nanopore imaging of 2-dimensional BIB-SEM mosaics. Hereby, S_m is comparable to ISA_{2D} (amount of pore wall surface per cross-sectional area), and S_{por} is comparable to the PoA parameter (amount of

pore wall surface per pore area). Our results indicate that the ISA_{2D} is the more important factor for the dielectric behavior in the 0.1- 100,000 Hz range, as it shows good correlation with CRS curves (Figure 5.21; left). The PoA parameter (S_{por}), which effectively factors out the porosity and is purely geometric, on the other hand, does not correlate well with CRS (Figure 5.21; right). Nevertheless, the frequency dispersion of CRS generally is mostly controlled by total porosity (Figure 5.20; left).

Formation Factor & Cementation factor m

Formation factors (FF) show the best correlation with CRS in this mudrock dataset, as indicated by the near-perfect color zonation of the CRS curve according to FF (Figure 5.20; right). This explains the high correlation coefficients for predictions of m from CRS. The underlying principle for CRS predictions becomes evident when plotting porosity against FF and color-coding the plot with our CRS input parameters. The slopes of both real (Figure 5.27; left) and imaginary (Figure 5.27; right) part of complex resistivity ($\beta_{amplitude}$ and β_{phase}) hereby show clear horizontal zonation, i.e. their values do not follow the lines of equal cementation factors. This implies that the slopes $\beta_{amplitude}$ and β_{phase} can be used to assess Formation Factors independent of plug porosity. Porosity and FF are the input for calculations of cementation exponents with Archie's equation (Eq. 5.3).

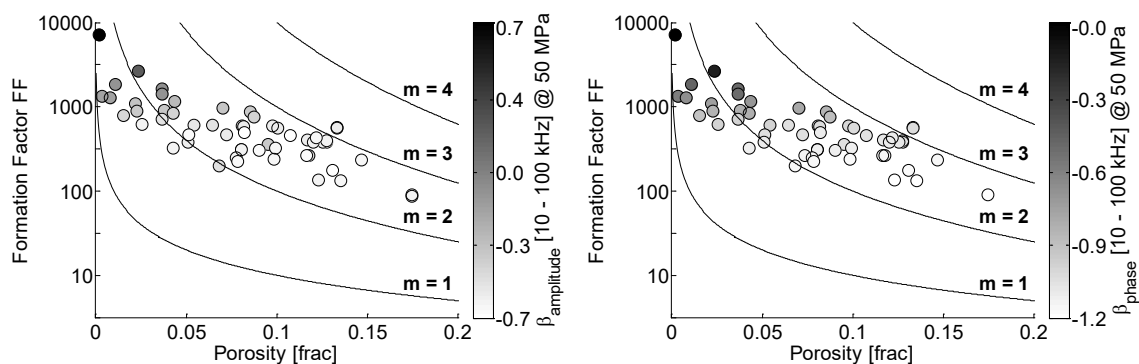


Figure 5.27: Cross-plots of porosity and Formation Factor, grayscale-coded with real slope of CRS ($\beta_{amplitude}$; left) and imaginary slope of CRS (β_{phase} ; right) at 50 MPa

effective pressure. Strong horizontal zonation of colors indicates that both slopes are sensitive to the absolute value of Formation Factor independent of the porosity.

Noteworthy is that we could calibrate model parameters *abcd* on a subset of 23 BIB-SEM samples and apply this Equation 5.15 to the entire core plug dataset of 56 samples, yet still get a correlation coefficient of $R^2 = 0.94$ (Figure 5.26; right). This shows that one can calibrate the constants on subsets and then apply the constants to larger intervals or even the entire formation. It is even possible that a universal equation is adequate to estimate cementation factors in all mudrock and also carbonate rocks, as predictions with a model calibrated on a carbonate dataset from a previous study (Norbisrath et al., in press) still yields very high correlation coefficients of $R^2 = 0.94$, even if a bit (Figure 5.28).

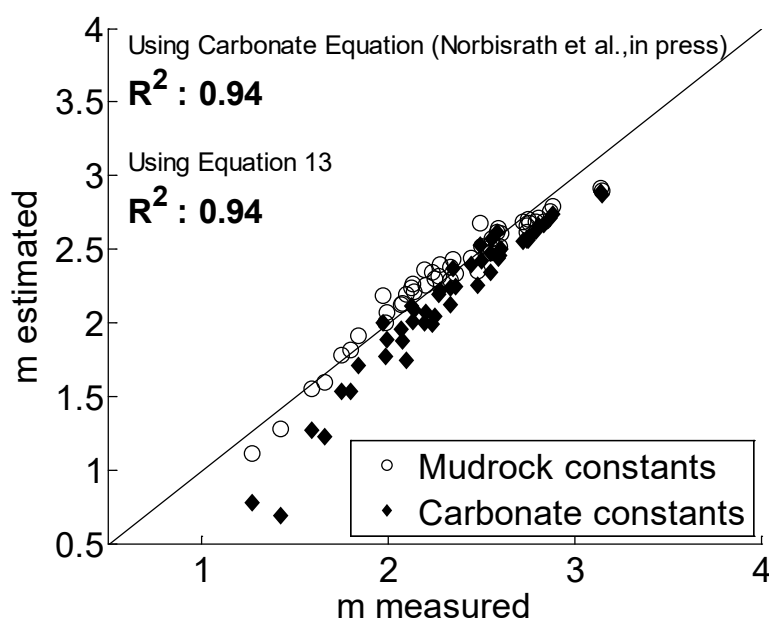


Figure 5.28: Predictions of cementation factor *m* on the entire mudrock dataset, using constants defined on smaller subset of 23 BIB-SEM samples (circles) and on a very heterogeneous carbonate dataset from a previous study (filled diamonds; Norbisrath et al., in press).

Wireline application

Due to the connection of CRS to pore geometry and surface-chemical processes, complex resistivity spectra have the potential to be used as direct estimators of cementation factor, porosity, and also mineralogy in laboratory and possible future wireline applications. Good correlations achieved in the lab on core material are especially encouraging since plugs have been dried and re-saturated, which usually reduces the accuracy of petrophysical core plug measurements (Bust et al., 2013). Development of a CRS wireline tool could help establish an alternative method to estimate important reservoir parameters, both in conventional and unconventional rocks.

Conclusion

This core plug study of mudrocks from the Vaca Muerta Formation in Argentina had two goals. 1) to assess the controlling factor on the resistivity on these mudrocks and 2) to predict physical properties using broad-ion-beam milling scanning electron microscopy (BIB-SEM) and measurements of complex resistivity spectra (CRS).

The most important finding is that cementation exponents show a strong positive correlation with porosity ($R^2 = 0.72$) in the dataset. Mineralogical results show that cementation factors increase with increasing TOC content, and decrease with increasing CO_3 . This information can aid in interpretation and well-log inversion of important reservoir properties in unconventional reservoirs.

Stitched BIB-SEM mosaics are used for quantification of the nanopore structure. BIB-SEM result show that the pore size distribution follows a power law in all samples, indicating that fractal scaling governs the pore space. Fractal scaling of the pore space enables predictions of pore size distributions and can also be used as a scaling rule in reservoir modeling.

The nanopore structure and the 2-dimensional Interfacial Surface Area (ISA_{2D}) are deemed to be a major controls on the frequency dispersion of CRS through interfacial polarization effects. However, connected helium plug porosity is the primary control on CRS, which is in turn directly related to formation factors. ISA_{2D} is only a secondary factor, while PoA or DOMsize, solely describing nanopore complexity, have no influence on CRS or cementation factors. The relationship between porosity and CRS is the underlying concept that enables the use of CRS for estimates of reservoir properties. Using a modified model from Tong & Tao (2008) with CRS input parameters, the method predicts cementation exponents with a correlation coefficient of $R^2 = 0.94$. The model further proves its general applicability to mudrock samples, as it is tested on a larger dataset of 56 samples and achieved $R^2 = 0.95$. Hence, a universal equation is put forward that is applicable to most tight mixed carbonate-siliciclastic reservoir rocks to predict cementation exponents from CRS:

$$m_{\text{estimated}} = 1.71\phi^{0.31}\beta_{\text{phase}}^{-0.20}\beta_{\text{amplitude}}^{0.10} \quad \text{Eq. 5.15}$$

The CRS prediction method has proven to be applicable to core plug measurements and now has to be tested in a wireline scenario. A successful technology transfer to well-logging would establish a new way to assess mineralogical and petrophysical properties down-hole, without the need for expensive coring and lab work.

Chapter 6: Summary

Rationale

This dissertation addresses the multiscale variability in carbonate pore structure and its effects on electrical resistivity, fluid flow, and low-frequency dielectric dispersion. The prevalence of heterogeneity presents a great challenge for reservoir evaluation and development in carbonates, which contain over 50 % of the world's remaining conventional oil in place. The goal is to improve inversion of well log data by improving the understanding of how measured data can be translated into usable parameters.

The pore geometry of a reservoir rock is the characteristic that regulates its hydrocarbon storage capacity and producibility. Carbonate rocks show highly variable pore structures due to the wide range in size and shape of their biogenic components, the often in-situ and unsorted deposition, and their strong diagenetic affinity. This heterogeneity leads to very complex petrophysical behavior, especially for the conduction of electrical charge where the fundamental controlling factors on cementation exponents have yet to be found.

As a result, inversion of petrophysical properties from wireline logs in carbonate rocks is still a challenge. This is especially true for estimates of water saturation, as cementation exponents in carbonates have been reported between $m = 1.0 - 5.5$ (Verwer et al., 2011; Ditya et al., 2013; Eberli et al., 2014; Norbistrath et al., 2015). Due to the exponential nature of m , a slightly different value can change the well assessment from a discovery to a dry hole. Hence, it is of utmost importance to achieve good estimates of cementation factor in carbonate rock formations.

Outcome

In this dissertation I present a new way to determine electrical and fluid flow properties from complex resistivity spectra (CRS). The phase shift of CRS is related to the dielectric properties of the sample and often shows a characteristic dispersion, i.e. a change of strength with frequency. This is attributed to polarization effects at the brine-rock interface and directly related to the amount of specific surface area, which controls permeability and cementation factors. This is the underlying connection that allows the use of CRS measurements for estimates of reservoir properties. The CRS method is applied to several datasets of dolomites, carbonates, and mudrocks and shown in chapter 3, 4, and 5, respectively, where it achieves very good correlation coefficients.

Further problems arise when trying to upscale results to a reservoir scale, as heterogeneity persists at all scales of carbonate pore space. This issue has been addressed in chapter 2 by combining quantitative pore structure parameters from analyses at different length scales into a multiscale analysis (Multiscale Digital Image Analysis – MsDIA). This method encompasses 6 orders of magnitude in pore sizes, from nanometer to millimeter scales. It explicitly includes carbonate microporosity, which has proven its influence on macroscopic and economically important flow and storage properties in reservoir rocks.

Implications

The combined results of this dissertation are meant to aid the inversion of carbonate pore structure from resistivity log data and thereby refine calculations of water and oil saturation in formation evaluation of carbonate reservoirs. A better understanding of micropore architecture and distribution together with knowledge about the inherent flow characteristics will aid in exploration and production from microporous formations.

Conclusion

This research effort has contributed three main insights into aspects of the heterogeneous carbonate pore structure and its petrophysical properties that can be useful in reservoir characterization of carbonate rocks:

- 1) Carbonate rocks contain at least four microporosity types, each of which has distinct electrical and fluid flow characteristics.
- 2) Complex resistivity spectra can be used to accurately estimate fluid and electrical flow properties.
- 3) Fractal scaling rules of pore sizes exist in all sedimentary rocks, expressed by log-log linear power law pore size distributions.

Chapter 1: Introduction

In chapter one gives an introduction into the purpose of the research and also introduces the two main new methodologies which are presented in this dissertation: (1) the use of broad-ion-beam milling (BIB) for effective quantification of carbonate microporosity types, and (2) the use of complex resistivity spectra (CRS) for estimates of pore structure and flow properties. The main work is presented in four chapters that each addresses a specific topic or dataset, and each chapter has been submitted to a suitable journal in order to make the result accessible to a broad audience:

Chapter 2: Electrical and Fluid Flow Properties of Carbonate Microporosity Types from Multiscale Digital Image Analysis and Mercury Injection

- Published in AAPG Bulletin

The purpose of chapter two was to better understand how microporosity influences electrical flow properties in carbonate rocks. Direct imaging and quantification of

microporosity has recently become possible with the adaption of the broad-ion-beam (BIB) milling method for flat surface preparation designed for SEM imaging (BIB-SEM). We utilized BIB-SEM and MICP methods, and main results are:

- The type of microporosity plays a crucial role for the electrical properties of a carbonate rock.
- Power-law pore size distributions is in place across all investigated length scales, from nanometer to millimeter scale.
- Smaller pore throats result in lower cementation factors.

Chapter 3: Fractal Pore Structure and Complex Resistivity Spectra (CRS) for Estimating Permeability in Dolomites from the Mississippian Madison Formation, Wyoming

- Submitted to SPWLA Petrophysics

Chapter three was an experiment to test if complex resistivity spectra could be used to estimate fluid flow properties in a homogeneous dolomite dataset consisting of 56 samples. This chapter builds on a previous dataset by Shen et al. that studied the influence of dolomite crystals shape and its results on petrophysical properties. Main results are:

- Crystal size has no influence on permeability or cementation factors in sucrosic dolomites
- Complex resistivity spectra can be used to estimate permeability in a homogeneous dolomite dataset.

Chapter 4: Complex Resistivity Spectra and Pore Geometry for Predictions of Reservoir Properties in Carbonate Rocks

- Submitted to AAPG Bulletin

In chapter four, the methodology of chapter three is applied on a heterogeneous carbonate dataset in order to estimate fluid and electrical flow properties. The dataset consists of 330 samples and various carbonate rock types from 12 separate studies (sub-datasets). The fundamental idea is that the pore geometry has a decisive effect on complex electrical resistivity spectra which consequently can be used to estimate other pore-geometry related petrophysical properties. Main results are:

- CRS can be used to reliably estimate permeability within a certain sub-dataset, and cementation factors within all measured samples with a single equation.
- Power-law pore size distributions are in place in all carbonate rock types.

Chapter 5: Nanopore Imaging in Vaca Muerta Mudrocks to Evaluate Controls on Complex Resistivity Spectra in Unconventional Reservoirs

- In preparation to be submitted to SPE Reservoir Engineering: Formation Evaluation

Chapter five applies the complex resistivity technique to estimate nanopore geometries and electrical flow properties in a mudrock dataset. Utilizing BIB-SEM and CRS methods, main results are:

- Nanopore geometry does not control electrical properties like CRS or cementation factors. Instead, porosity is the main control.
- CRS can be used to reliably estimate cementation factors in mixed carbonate-siliciclastic mudrocks, but also to estimate TOC, CO₃ and specific surface area.
- Power-law pore size distributions are in place in mudrocks.

References

- Abousrafa, E. M., J. M. Somerville, S. A. Hamilton, P. W. H. Olden, B. D. G. Smart, and J. Ford, 2009, Pore geometrical model for the resistivity of brine saturated rocks: *Journal of Petroleum Science and Engineering*, v. 65, no. 3–4, p. 113–122, doi:10.1016/j.petrol.2008.12.009.
- Adisoemarta, P. S., G. A. Anderson, S. M. Frailey, and G. B. Asquith, 2001, Saturation exponent n in well log interpretation: Another look at the permissible range: SPE Permian Basin Oil and Gas Recovery Conference, Midland, Texas, May 15–17, 2001, SPE Paper 70043, 4 p., doi:10.2118/70043-MS.
- Ahr, W. M., D. Allen, A. Boyd, H. N. Bachman, T. Smithson, E. Clerke, K. Gzara, J. Hassall, C. Murty, and H. Zubari, 2005, Confronting the carbonate conundrum: *Oilfield Review*, v. 17, p. 18–29.
- Ambrose, R. J., 2011, Micro-structure of gas shales and its effects on gas storage and production performance: Ph.D. thesis, The University of Oklahoma, Norman, Oklahoma, 180 p.
- Anderson, B., T. Barber, M. Lüling, P. Sen, R. Taherian, and J. Klein, 2008, Identifying Potential Gas-Producing Shales From Large Dielectric Permittivities Measured By Induction Quadrature Signals, SPWLA 49th Annual Logging Symposium, May 25-28, 2008, Society of Petrophysicists and Well-Log Analysts.
- Anselmetti, F. S., and G. P. Eberli, 1993, Controls on sonic velocity in carbonates: *Pure and Applied Geophysics*, v. 141, p. 287-323.
- Anselmetti, F. S., Eberli, G.P., and Bernoulli, D., 1997, Seismic modeling of a carbonate platform margin (Montagna della Maiella, Italy): variations in seismic facies and implications for sequence stratigraphy. In: Marfurt, F.J. and Palaz, A. (eds.) *Carbonate Seismology: SEG Geophysical Developments Series 6*, p. 373-406.
- Anselmetti, F. S., S. Luthi, and G. P. Eberli, 1998, Quantitative characterization of carbonate pore systems by digital image analysis: *AAPG Bulletin*, v. 82, p. 1815–1836.
- Archie, G. E., 1942, The electrical resistivity log as an aid in determining some reservoir characteristics: *Transactions of the AIME*, v. 146, p. 54-62. Arps, J. J., 1953, The effect of temperature on the density and electrical resistivity of sodium chloride solutions: *Journal of Petroleum Technology*, v. 5, p. 17-20.
- Archie, G. E., 1952, Classification of carbonate reservoir rocks and petrophysical considerations: *AAPG Bulletin*, v. 36, p. 278–298.

- Arns, C. H., F. Bauget, A. Ghous, A. Sakellario, U. T. J. Senden, A. P. Sheppard, R. M. Sok, W. V. Pinczewski, J. C. Kelly, and M. A. Knackstedt, 2005, Digital core laboratory: Petrophysical analysis from 3D imaging of reservoir core fragments: *Petrophysics*, v. 46, p. 260–277.
- Arps, J. J., 1953, The effect of temperature on the density and electrical resistivity of sodium chloride solutions: *Journal of Petroleum Technology*, v. 5, no. 10, p. 17–20, doi:10.2118/953327-G.
- Baechle, G. T., A. Colpaert, G. P. Eberli, and R. J. Weger, 2008, Effects of microporosity on sonic velocity in carbonate rocks: *The Leading Edge*, v. 27, p. 1012–1018.
- Bean, C., S. Cole, K. Boyle, D. Kho, and T. J. Neville, 2013, New Wireline Dielectric Dispersion Logging Tool Result in Fluvio-Deltaic Sands Drilled with Oil-Based Mud, Society of Petrophysicists and Well-Log Analysts.
- Beaumont, E. A., and N. H. Foster, 1999, *Treatise of petroleum geology—Handbook of petroleum geology: Exploring for oil and gas traps*: AAPG, p. 9-1–9-154.
- Bloecher, G., and G. Zimmermann, 2008, Settle3D—A numerical generator for artificial porous media: *Computers and Geosciences*, v. 34, p. 1827–1842.
- Braithwaite, C. J., G. Rizzi, and G. Darke, 2004, The geometry and petrogenesis of dolomite hydrocarbon reservoirs: introduction: Geological Society, London, Special Publications, v. 235, p. 1-6.
- Buoniconti, M.R., 2008, The evolution of the carbonate shelf margins and fill of the Antler foreland basin by prograding Mississippian carbonates. Ph.D. dissertation, University of Miami, 436p.
- Bush, D. C., and R. E. Jenkins, 1970, Proper Hydration of Clays for Rock Property Determinations: *Journal of Petroleum Technology*, v. 22, p. 800 - 804.
- Bust, V. K., A. A. Majid, J. U. Oletu, and P. F. Worthington, 2013, The petrophysics of shale gas reservoirs: Technical challenges and pragmatic solutions: *Petroleum Geoscience*, v. 19, p. 91-103.
- Bustin, R. M., A. M. Bustin, A. Cui, D. Ross, and V. M. Pathi, 2008, Impact of shale properties on pore structure and storage characteristics: SPE shale gas production conference.
- Bustin, R. M., A. M. Bustin, D. Ross, G. Chalmers, V. Murthy, C. Laxmi, and X. Cui, 2009, Shale gas opportunities and challenges: AAPG Annual Convention, San Antonio, Texas, April 20–23, 2008, AAPG Search and Discovery Article #40382.

- Cerepi, A., C. Durand, and E. Brosse, 2002, Pore microgeometry analysis in low-resistivity sandstone reservoirs: *Journal of Petroleum Science and Engineering*, v. 35, no. 3–4, p. 205–232, doi:10.1016/S0920-4105(02)00244-9.
- Cerepi, A., 2004, Geological control of electrical behaviour and prediction key of transport properties in sedimentary porous systems: *Colloids and Surfaces A: Physicochemical and Engineering Aspects*, v. 241, p. 281-298.
- Chafetz, H. S., 2013, Porosity in bacterially induced carbonates: Focus on micropores: *AAPG Bulletin*, v. 97, no. 11, p. 2103–2111, doi:10.1306/04231312173.
- Chemali, R., D. Heysse, G. Merchant, and C. Jackson, 1995, Comparisons of wireline and LWD resistivity highlight resistivity frequency dispersion in sedimentary formations: *SPWLA 36th Annual Logging Symposium*.
- Choquette, P. W., and L. C. Pray, 1970, Geologic nomenclature and classification of porosity in sedimentary carbonates: *AAPG Bulletin*, v. 54, p. 207–250.
- Choquette, P. W., and E. E. Hiatt, 2008, Shallow-burial dolomite cement: a major component of many ancient sucrosic dolomites: *Sedimentology*, v. 55, p. 423-460.
- Clarkson, C. R., J. L. Jensen, and T. Blasingame, 2011, Reservoir engineering for unconventional reservoirs: what do we have to consider?: *North American Unconventional Gas Conference and Exhibition*.
- Clarkson, C. R., N. Solano, R. M. Bustin, A. M. Bustin, G. R. L. Chalmers, L. He, Y. B. Melnichenko, A. P. Radliński, and T. P. Blach, 2013, Pore structure characterization of North American shale gas reservoirs using USANS/SANS, gas adsorption, and mercury intrusion: *Fuel*, v. 103, p. 606-616.
- Clennell, B., D. Dewhurst, M. Raven, R. Sedev, and A. Borysenko, 2006, Shale petrophysics: electrical, dielectric and nuclear magnetic resonance studies of mudrocks and clays: *SPWLA 47th Annual Logging Symposium*.
- Clennell, M. B., M. Josh, L. Esteban, C. D. Piane, S. Schmid, M. Verrall, D. Hill, C. Woods, and B. McMullan, 2010, The influence of pyrite on rock electrical properties: a case study from NW Australian gas reservoirs: *SPWLA 51st Annual Logging Symposium*.
- Clerke, E. A., H. W. Mueller III, E. C. Phillips, R. Y. Eyvazzadeh, D. H. Jones, R. Ramamoorthy, and A. Srivastava, 2008, Application of Thomeer Hyperbolas to decode the pore systems, facies and reservoir properties of the Upper Jurassic Arab D Limestone, Ghawar field, Saudi Arabia: A “Rosetta Stone” approach: *GeoArabia*, v. 13, p. 113-160.

- Crousse, L. C., S. A. Cuervo, D. Vallejo, L. E. Mosse, T. Fischer, and D. McCarty, 2015, Unconventional Shale Pore System Characterization in El Trapial Area, Vaca Muerta, Argentina: Unconventional Resources Technology Conference (URTEC).
- Curtis, M. E., R. J. Ambrose, and C. H. Sondergeld, 2010, Structural characterization of gas shales on the micro- and nano-scales: Canadian Unconventional Resources and International Petroleum Conference, Calgary, Alberta, October 19–21, 2010, SPE Paper 137693, 15 p., doi:10.2118/137693-MS.
- Curtis, M. E., C. H. Sondergeld, R. J. Ambrose, and C. S. Rai, 2012, Microstructural investigation of gas shales in two and three dimensions using nanometer-scale resolution imaging: AAPG Bulletin, v. 96, no. 4, p. 665–677, doi:10.1306/08151110188.
- Denicol, P. S., and X. D. Jing, 1998, Effects of water salinity, saturation and clay content on the complex resistivity of sandstone samples: Geological Society, London, Special Publications, v. 136, p. 147-157.
- Desbois, G., J. L. Urai, and P. Kukla, 2009, Morphology of the pore space in claystones—Evidence from BIB/FIB ion beam sectioning and cryo-SEM observations: Earth Discussions, v. 4, no. 1, p. 1–19, doi:10.5194/eed-4-1-2009.
- Desbois, G., J. L. Urai, P. A. Kukla, J. Konstanty, and C. Baerle, 2011, High-resolution 3D fabric and porosity model in a tight gas sandstone reservoir: A new approach to investigate microstructures from mm- to nm-scale combining argon beam cross-sectioning and SEM imaging: Journal of Petroleum Science and Engineering, v. 78, no. 2, p. 243–257, doi:10.1016/j.petrol.2011.06.004.
- Ditya, A., 2012, Petrophysical characterization of Pliocene-Pleistocene Reefal Carbonates, Southern Dominican. MS Thesis University of Miami, Open Access Theses, paper 358, 145pp.
- Dixon, J., and B. Marek, 1990, The effect of bimodal pore size distribution on electrical properties of some middle eastern limestones: SPE Annual Technical Conference and Exhibition, New Orleans, Louisiana, September 23–26, 1990, SPE Paper 20601, p. 743–750, doi:10.2118/20601-MS.
- Driskill, B., J. Walls, J. DeVito, and S. W. Sinclair, 2013, Applications of SEM Imaging to reservoir characterization in the Eagle Ford Shale, South Texas, USA: Electron Microscopy of Shale Hydrocarbon Reservoirs: AAPG Memoir 102, v. 102, p. 115.
- Dunham, R. J., 1962, Classification of carbonate rocks according to depositional texture, in W. E. Hamm, ed., Classification of carbonate rocks—A symposium: AAPG Memoir 1, p. 108–121.

- Eberli, G. P., G. Baechle, F. Anselmetti, and M. Incze, 2003, Factors controlling elastic properties in carbonate sediments and rocks: *The Leading Edge*, v. 22, no. 7, p. 654–660, doi:10.1190/1.1599691.
- Eberli, G. P., R. J. Weger, E. Karaca, E. Parke, J. H. Norbistrath, and G. Della Porta, 2014, Comparison of petrophysical properties and pore structures of stromatolites, travertine and tufa. *CSL Annual Review Meeting Abstract volume*, p. 93- 96.
- Ehrlich, R., E. L. Etris, D. Brumfield, L. Yuan, and S. J. Crabtree, 1991, Petrography and reservoir physics III: Physical models for permeability and formation factor: *AAPG Bulletin*, v. 75, p. 1579–1592.
- Ellis, D. V., and J. M. Singer, 2007, *Well Logging for Earth Scientists: Well Logging for Earth Scientists*, by DV Ellis and JM Singer. Berlin: Springer, 2007. ISBN: 978-1-4020-3738-2, v. 1.
- Firdaus, G., and Z. Heidari, 2015, Quantifying electrical resistivity of isolated kerogen from organic-rich mudrocks using laboratory experiments, *SPE Annual Technical Conference and Exhibition*, 28-30 September, Houston, Texas, USA, Society of Petroleum Engineers.
- Folk, R. L., 1959, Practical petrographic classification of lime- stones: *AAPG Bulletin*, v. 43, p. 1–38.
- Garcia, M. N., F. Sorenson, J. C. Bonapace, F. Motta, C. Bajuk, and H. Stockman, 2013, Vaca Muerta Shale Reservoir Characterization and Description: The Starting Point for Development of a Shale Play with Very Good Possibilities for a Successful Project: *Unconventional Resources Technology Conference (URTEC)*.
- Garing, C., L. Luquot, P. A. Pezard, and P. Gouze, 2014, Electrical and flow properties of highly heterogeneous carbonate rocks: *AAPG Bulletin*, v. 98, no. 1, p. 49–66, doi:10.1306/05221312134.
- Garrouch, A. A., and M. M. Sharma, 1992, Techniques for the measurement of electrical properties of cores in the frequency range 10 Hz to 10 MHz: international symposium for the Society of Core Analysts, Oklahoma City, Oklahoma.
- Glover, P., 2009, What is the cementation exponent? A new interpretation: *The Leading Edge*, v. 28, p. 82-85.
- Gong, L., and J. k. Wu, 2006, Resistance effect of electric double layer on liquid flow in microchannel: *Applied Mathematics and Mechanics*, v. 27, p. 1391–1398, doi:10.1007/s10483-006-1011-1.

- Han, M., J. Cuadros, C. A. P. Suarez, E. Decoster, O. Faivre, L. Mosse, and N. Seleznev, 2012, Continuous Estimate Of Cation Exchange Capacity From Log Data: A New Approach Based On Dielectric Dispersion Analysis, Society of Petrophysicists and Well-Log Analysts.
- Hemes, S., G. Desbois, J. L. Urai, M. De Craen, and M. Honty, 2013, Variations in the morphology of porosity in the Boom Clay Formation: insights from 2D high resolution BIB-SEM imaging and Mercury injection Porosimetry: Netherlands Journal of Geosciences—Geologie en Mijnbouw, v. 92, p. 275–300, p. 5631.
- Hemes, S., G. Desbois, J. L. Urai, B. Schröppel, and J.-O. Schwarz, 2015, Multi-scale characterization of porosity in Boom Clay (HADES-level, Mol, Belgium) using a combination of X-ray μ -CT, 2D BIB-SEM and FIB-SEM tomography: Microporous and Mesoporous Materials, v. 208, p. 1-20.
- Herrick, D. C., and W. D. Kennedy, 1994, Electrical efficiency— A pore geometric theory for interpreting the electrical properties of reservoir rocks: Geophysics, v. 59, no. 6, p. 918–927, doi:10.1190/1.1443651.
- Hizem, M., H. Budan, B. Deville, O. Faivre, L. Mosse, and M. Simon, 2008, Dielectric Dispersion: A New Wireline Petrophysical Measurement, Society of Petroleum Engineers.
- Houben, M. E., G. Desbois, and J. L. Urai, 2013, Pore morphology and distribution in the Shaly facies of Opalinus Clay (Mont Terri, Switzerland): Insights from representative 2D BIB-SEM investigations on mm to nm scale: Applied Clay Science, v. 71, p. 82–97, doi:10.1016/j.clay.2012.11.006.
- Houben, M. E., G. Desbois, and J. L. Urai, 2014, A comparative study of representative 2D microstructures in Shaly and Sandy facies of Opalinus Clay (Mont Terri, Switzerland) inferred from BIB-SEM and MIP methods: Marine and Petroleum Geology, v. 49, p. 143–161, doi:10.1016/j.marpetgeo.2013.10.009.
- Howell, J., A., E. Schwarz, L.A. Spalletti, and G.D. Veiga, 2005, The Neuquén Basin: an overview. In: The Neuquén Basin, Argentina - A case Study in Sequence Stratigraphy and Basin Dynamics (Eds G.D. Veiga, L.A. Spalletti, J.A. Howell and E. Schwarz), Special Publication, 1-14. Geological Society, London.
- Hulea, I. N., and C. A. Nicholls, 2012, Carbonate rock characterization and modeling: Capillary pressure and permeability in multimodal rocks—A look beyond sample specific heterogeneity: AAPG Bulletin, v. 96, no. 9, p. 1627–1642, doi:10.1306/02071211124.

- Jackson, P. D., R. D. Jarrard, C. J. Pigram, and J. M. Pearce, 1993, Resistivity/porosity/velocity relationships from down-hole logs: An aid for evaluating pore morphology, in J. A. McKenzie, P. J. Davies, and A. Palmer-Julson et al., Proceedings of the Ocean Drilling Program, Scientific Results, v. 133, College Station, Texas, p. 661–686, doi: 10.2973/odp.proc.sr.133.271.1993.
- Jackson, P. M., and L. K. Smith, 2014, Exploring the undulating plateau: the future of global oil supply: *Philosophical Transactions of the Royal Society of London A: Mathematical, Physical and Engineering Sciences*, v. 372, p. 20120491.
- Janssen, C., R. Wirth, A. Reinicke, E. Rybacki, R. Naumann, H.-R. Wenk, and G. Dresen, 2011, Nanoscale porosity in SAFOD core samples (San Andreas Fault): *Earth and Planetary Science Letters*, v. 301, no. 1–2, p. 179–189, doi:10.1016/j.epsl.2010.10.040.
- Karaca, E., 2015, Pore Structure and Petrophysical Characterization of Hamelin Pool Stromatolites and Pavements, Shark Bay, Western Australia. MS Thesis University of Miami, Open Access Theses, paper 567, 134pp.
- Katz, A. J., and A. H. Thompson, 1985, Fractal sandstone pores: Implications for conductivity and pore formation: *Physical Review Letters*, v. 54, no. 12, p. 1325–1328, doi:10.1103/PhysRevLett.54.1325.
- Katz, A. J., and A. H. Thompson, 1987, Prediction of rock electrical conductivity from mercury injection measurements: *Journal of Geophysical Research: Solid Earth*, v. 92, p. 599–607, doi:10.1029/JB092iB01p00599.
- Kazemzadeh, E., M. Nabi-Bidhendi, M. K. Moezabad, M. Rezaee, and K. Saadat, 2007, A new approach for the determination of cementation exponent in different petrofacies with velocity deviation logs and petrographical studies in the carbonate Asmari formation: *Journal of Geophysics and Engineering*, v. 4, no. 2, p. 160–170, doi:10.1088/1742-2132/4/2/005.
- Kethireddy, N., H. Chen, and Z. Heidari, 2014, Quantifying the effect of kerogen on resistivity measurements in organic-rich Mudrocks, v. 55, p. 136 - 146.
- Kietzmann, D.A., Martín-Chivelet, J., Palma, R.M., López-Gómez, J., Lescano, M. and Concheyro, A. (2011) Evidence of precessional and eccentricity orbital cycles in a Tithonian source rock: The mid-outer carbonate ramp of the Vaca Muerta Formation, northern Neuquén Basin, Argentina. *AAPG Bulletin*, 95, 1459-1474.
- Klaver, J., G. Desbois, J. L. Urai, and R. Littke, 2012, BIB-SEM study of the pore space morphology in early mature Posidonia Shale from the Hils area, Germany: *International Journal of Coal Geology*, v. 103, p. 12–25, doi:10.1016/j.coal.2012.06.012.

- Klaver, J., S. Hemes, M. Houben, G. Desbois, Z. Radi, and J. L. Urai, 2015a, The connectivity of pore space in mudstones: Insights from high-pressure Wood's metal injection, BIB- SEM imaging, and mercury intrusion porosimetry: *Geofluids*, doi:10.1111/gfl.12128.
- Klaver, J., G. Desbois, R. Littke, and J. L. Urai, 2015b, BIB-SEM characterization of pore space morphology and distribution in postmature to overmature samples from the Haynesville and Bossier Shales: *Marine and Petroleum Geology*, v. 59, p. 451-466.
- Knight, R. J., and A. Nur, 1987, The dielectric-constant of sandstones, 60 KHz to 4 MHz: *Geophysics*, v. 52, p. 644-654.
- Krohn, C. E., 1988, Sandstone fractal and Euclidean pore volume distributions: *Journal of Geophysical Research: Solid Earth*, v. 93, p. 3286–3296, doi:10.1029/JB093iB04p03286.
- Lasswell, P. M., 2006, Core analysis for electrical properties: *Petrophysics*, v. 47, p. 191-213.
- Laurich, B., J. L. Urai, G. Desbois, C. Vollmer, and C. Nussbaum, 2014, Microstructural evolution of an incipient fault zone in Opalinus Clay: Insights from an optical and electron microscopic study of ion-beam polished samples from the Main Fault in the Mt-Terri Underground Research Laboratory: *Journal of Structural Geology*, v. 67, Part A, p. 107-128.
- Leanza, H., F. Sattler, R.S. Martinez, and O. Carbone, 2011, La Formacion Vaca Muerta y Equivalentes (Jurassico Tardio - Cretacico Temprano) en la Cuenca Neuquina. In: *Geologia y Recursos Naturales de la Provincia del Neuquen, Relatorio del XVIII Congreso Geologico Argentino* (Eds H. Leanza, C. Arregui, O. Carbone, J.C. Danieli and J.M. Valles), 113-130. Asociacion Geologica Argentina, Buenos Aires.
- Legarreta, L., and H. J. Villar, 2011, Geological and Geochemical Keys of the Potential Shale Resources, Argentina Basins: *Search and Discovery Article*, v. 80196.
- De Lima, O. A., and M. M. Sharma, 1991, Water conductivity and saturation effects on the dielectric response of shaly sands: *SPWLA 32nd Annual Logging Symposium*.
- Little, J. D., D. R. Julander, L. C. Knauer, J. T. Aultman, and J. L. Hemingway, 2010, Dielectric dispersion measurements in California heavy oil reservoirs, *Society of Petrophysicists and Well-Log Analysts*.
- Lønøy, A., 2006, Making sense of carbonate pore systems: *AAPG Bulletin*, v. 90, no. 9, p. 1381–1405, doi:10.1306/03130605104.

- Loucks, R. G., R. M. Reed, S. C. Ruppel, and D. M. Jarvie, 2009, Morphology, Genesis, and distribution of nanometer-scale pores in Siliceous Mudstones of the Mississippian Barnett Shale: *Journal of Sedimentary Research*, v. 79, p. 848-861.
- Loucks, R. G., F. J. Lucia, and L. E. Waite, 2013, Origin and description of the micropore network within the Lower Cretaceous Stuart City Trend tight-gas limestone reservoir in Pawnee Field in South Texas: *GCAGS Journal*, v. 2, p. 29–41.
- Lucia, F., 1983, Petrophysical parameters estimated from visual descriptions of carbonate rocks: a field classification of carbonate pore space: *Journal of Petroleum Technology*, v. 35, p. 629-637.
- Lucia, F. J., 1995, Rock-fabric/petrophysical classification of carbonate pore space for reservoir characterization: *AAPG Bulletin*, v. 79, p. 1275–1300.
- Lucia, F. J., 1999, Carbonate reservoir characterization: New York, Springer-Verlag, 226 p.
- Lucia, F. J., and R. G. Loucks, 2013, Microporosity in carbonate mud: Early development and petrophysics: *GCAGS Journal*, v. 2, p. 1–10.
- Machado, V., P. Frederico, P. Netto, R. Bagueira, A. Boyd, A. Souza, L. Zielinski, and E. Junk, 2011, Carbonate petrophysics in wells drilled with oil-base mud: SPWLA 52nd Annual Logging Symposium, Society of Petrophysicists and Well-Log Analysts.
- Mandelbrot, B. B., 1967, How long is the coast of Britain: *Science*, v. 156, no. 3775, p. 636–638, doi:10.1126/science.156.3775.636.
- Markov, M., E. Kazatchenko, A. Mousatov, and E. Pervago, 2012, The dielectric permittivity of carbonate formations from the unified microstructure model: *Journal of Applied Geophysics*, v. 76, p. 56-63.
- Mazzullo, S., H. Rieke, and G. Chilingarian, 1996, Carbonate Reservoir Characterization: A Geologic-Engineering Analysis, Part II: A Geologic-Engineering Analysis, v. 44, Elsevier.
- McCreech, C. A., R. Ehrlich, and S. J. Crabtree, 1991, Petrography and reservoir physics II: Relating thin section porosity to capillary pressure, the association between pore types and throat size: *AAPG Bulletin*, v. 75, p. 1563–1578.

- Melim, L., H. Westphal, P. Swart, G. Eberli, and A. Munnecke, 2002, Questioning carbonate diagenetic paradigms: Evidence from the Neogene of the Bahamas: *Marine Geology*, v. 185, no. 1–2, p. 27–53, doi:10.1016/S0025-3227(01)00289-4.
- Merkle, A. P., and J. Gelb, 2013, The ascent of 3D X-ray microscopy in the laboratory: *Microscopy Today*, v. 21, no. 2, p. 10–15, doi:10.1017/S1551929513000060.
- Mitchum, R.M. and M.A. Uliana, 1985, Seismic stratigraphy of carbonate depositional sequences, Upper Jurassic-Lower Cretaceous, Neuquén Basin, Argentina. In: *Seismic Stratigraphy: An Integrated Approach to Hydrocarbon Exploration*. AAPG Memoir (Eds B.R. Bero and D.G. Wooverton), AAPG Memoir, 255-274.
- Moore C. H., 2001, Carbonate Reservoirs: Porosity evolution and diagenesis in a sequence stratigraphic framework. *Developments in Sedimentology*, v. 55, Elsevier, Amsterdam, 444 p.
- Mosse, L., R. Carmona, E. Decoster, O. Faivre, and M. Hizem, 2009, Dielectric dispersion logging in heavy oil: a case study from the Orinoco belt: SPWLA 50th Annual Logging Symposium.
- Moulin, P., and H. Roques, 2003, Zeta potential measurement of calcium carbonate: *Journal of colloid and interface science*, v. 261, p. 115-126.
- Mude, J., S. Arora, T. McDonald, and J. Edwards, 2010, Wireline Dielectric Measurements Make a Comeback: Applications In Oman For a New Generation Dielectric Log Measurement, Society of Petrophysicists and Well-Log Analysts.
- Nelder, J. A., and R. Mead, 1965, A simplex method for function minimization: *The Computer Journal*, v. 7, p. 308-313.
- Nelson, P. H., 2009, Pore-throat sizes in sandstones, tight sandstones, and shales: *AAPG Bulletin*, v. 93, no. 3, p. 329– 340, doi:10.1306/10240808059.
- Norbisrath, J. H., G. P. Eberli, R. J. Weger, M. Knackstedt, and K. Verwer, 2011, Modeling electrical resistivity in carbonates using micro-CT scans and assessing the influence of microporosity using MICP. Abstract CSL Annual Review Meeting.
- Norbisrath, J. H., G. P. Eberli, B. Laurich, G. Desbois, R. J. Weger, and J. L. Urai, 2015, Electrical and fluid flow properties of carbonate microporosity types from multiscale digital image analysis and mercury injection: *AAPG Bulletin*, v. 99, p. 2077-2098.

- Norbisrath, J. H., G. P. Eberli, S. Shen, and R. J. Weger, in press, Fractal Pore Structure and Complex Resistivity Spectra (CRS) for Estimating Permeability in Dolomites from the Mississippian Madison Formation, Wyoming: SPWLA Petrophysics.
- Pape, H., C. Clauser, and J. Iffland, 1999, Permeability prediction based on fractal pore-space geometry: *GEOPHYSICS*, v. 64, p. 1447-1460.
- Pirrone, M., N. Bona, M. Galli, F. Pampuri, O. Faivre, M. Han, M. Hizem, and L. Mosse, 2011, An innovative dielectric dispersion measurement for better evaluation of thin layered reservoirs applied in a south Italy well: Offshore Mediterranean Conference and Exhibition.
- Purkis, S. J., B. M. Riegl, and S. Andréfouët, 2005, Remote sensing of geomorphology and facies patterns on a modern carbonate ramp (Arabian Gulf, Dubai, U.A.E.): *Journal of Sedimentary Research*, v. 75, no. 5, p. 861–876, doi:10.2110/jsr.2005.067.
- Purkis, S., G. Casini, D. Hunt, and A. Colpaert, 2015, Morphometric patterns in Modern carbonate platforms can be applied to the ancient rock record: Similarities between Modern Alacranes Reef and Upper Palaeozoic platforms of the Barents Sea: *Sedimentary Geology*, v. 321, p. 49-69.
- Radlinski, A., M. Ioannidis, A. Hinde, M. Hainbuchner, M. Baron, H. Rauch, and S. Kline, 2004, Angstrom-to- millimeter characterization of sedimentary rock microstructure: *Journal of Colloid and Interface Science*, v. 274, no. 2, p. 607–612, doi:10.1016/j.jcis.2004.02.035.
- Raythatha, R., and P. N. Sen, 1986, Dielectric properties of clay suspensions in MHz to GHz range: *Journal of Colloid and Interface Science*, v. 109, p. 301-309.
- Revil, A., 2012, Spectral induced polarization of shaly sands: Influence of the electrical double layer: *Water Resources Research*, v. 48.
- Rezende, M. F., S. N. Tonietto, and M. C. Pope, 2013, Three- dimensional pore connectivity evaluation in a Holocene and Jurassic microbialite buildup: *AAPG Bulletin*, v. 97, no. 11, p. 2085–2101, doi:10.1306/05141312171.
- Sahimi, M., 2011, Flow and transport in porous media and fractured rock: From classical methods to modern approaches: New York, John Wiley & Sons, 718 p.
- Sando, W., 1988, Madison Limestone (Mississippian) Paleokarst: A Geologic Synthesis, in N. James, and P. Choquette, eds., *Paleokarst*, Springer New York, p. 256-277.
- Scott, J. H., and G. R. Olhoeft, 1980, Nonlinear Complex Resistivity Logging: SPWLA 21st Annual Logging Symposium, Lafayette, Louisiana, Society of Petrophysicists and Well-Log Analysts.

- Seleznev, N. V., 2005, Theoretical and laboratory investigation of dielectric properties of partially saturated carbonate rocks, DUP Science.
- Seleznev, N., T. Habashy, A. Boyd, and M. Hizem, 2008, Technique for determining properties of earth formations using dielectric permittivity measurements, U.S. Patent No. 7,363,160. 22 Apr. 2008.
- Seleznev, N. V., R. L. Kleinberg, M. M. Herron, and M. Machlus, 2011, Applications of Dielectric Dispersion Logging to Oil-Shale Reservoirs: SPWLA 52nd Annual Logging Symposium, p. 14-18.
- Sen, P., 1981, Relation of certain geometrical features to the dielectric anomaly of rocks: *Geophysics*, v. 46, p. 1714-1720.
- Sen, P. N., W. E. Kenyon, H. Takezaki, and M. J. Petricola, 1997, Formation factor of carbonate rocks with microporosity: Model calculations: *Journal of Petroleum Science and Engineering*, v. 17, no. 3-4, p. 345-352, doi:10.1016/S0920-4105(96)00005-8.
- Shen, S., and G. P. Eberli, 2008, The effects of rock texture and pore type on sonic velocity in dolomite: *GEO 2008*.
- Skalinski, M., and J. A. Kenter, 2015, Carbonate petrophysical rock typing: integrating geological attributes and petrophysical properties while linking with dynamic behaviour: *Geological Society, London, Special Publications*, v. 406, p. 229-259.
- Slater, L., D. Ntarlagiannis, and D. Wishart, 2006, On the relationship between induced polarization and surface area in metal-sand and clay-sand mixtures: *GEOPHYSICS*, v. 71, p. A1-A5.
- Smith, J., A. Chen, D. Gostovic, D. Hickey, D. Kundering, K. Duncan, R. DeHoff, K. Jones, and E. Wachsman, 2009, Evaluation of the relationship between cathode microstructure and electrochemical behavior for SOFCs: *Solid State Ionics*, v. 180, no. 1, p. 90-98, doi:10.1016/j.ssi.2008.10.017.
- Smith, L. B., G. P. Eberli, J. L. Masferro, and S. Al-Dhahab, 2003, Discrimination of effective from ineffective porosity in heterogeneous Cretaceous carbonates, Al Ghubar field, Oman: *AAPG Bulletin*, v. 87, no. 9, p. 1509-1529, doi:10.1306/041703200180.
- Smith, L. B., G. P. Eberli, and M. Sonnenfeld, 2004, Sequence stratigraphic and paleogeographic distribution of reservoir-quality dolomite, Madison Formation, Wyoming and Montana. In: Grammer, G. M., P. M. Harris, and G. P. Eberli (eds.), *Integration of Outcrop and Modern Analogs in Reservoir Modeling. AAPG Memoir 80*, p. 67-92.

- Snyder, D. D., R. Merkel, and J. Williams, 1977, Complex formation resistivity-the forgotten half of the resistivity log: SPWLA 18th Annual Logging Symposium, Society of Petrophysicists and Well-Log Analysts.
- Sok, R. M., T. Varslot, A. Ghous, S. Latham, A. P. Sheppard, and M. A. Knackstedt, 2010, Pore scale characterization of carbonates at multiple scales: Integration of micro-CT, BSEM, and FIBSEM: *Petrophysics*, v. 51, p. 379–387.
- Sonnenfeld, M. D., 1996, Sequence evolution and hierarchy within the Lower Mississippian Madison Limestone of Wyoming, in M. W. Longman, and M. D. Sonnenfeld, eds., *Paleozoic Systems of the Rocky Mountain Region*, SEPM Rocky Mountain Section, p. 165-192.
- Spalletti, L.A., J.R. Franzese, S.D. Matheos, and E. Schwarz, 2000, Sequence stratigraphy of a tidally dominated carbonate-siliciclastic ramp; the Tithonian-Early Berriasian of the Southern Neuquén Basin, Argentina. *Journal of the Geological Society*, 157, 433-446.
- Sternberg, B. K., D. E. Dunster, and K. D. Honeycutt, 1987, Method and apparatus for complex resistivity measurements with elimination of electromagnetic coupling effects, U.S. Patent No. 4,642,570. 10 Feb. 1987.
- Suman, R. J., and R. J. Knight, 1997, Effects of pore structure and wettability on the electrical resistivity of partially saturated rocks—A network study: *Geophysics*, v. 62, no. 4, p. 1151–1162, doi:10.1190/1.1444216.
- Swanson, B. F., 1985, Microporosity in reservoir rocks: Its measurement and influence on electrical resistivity: *The Log Analyst*, v. 26, p. 42–52.
- Tong, M., and H. Tao, 2008, Permeability estimating from complex resistivity measurement of shaly sand reservoir: *Geophysical Journal International*, v. 173, p. 733-739.
- Turcotte, D. L., 1997, *Fractals and chaos in geology and geophysics*: Cambridge, UK, Cambridge University Press, 398 p.
- Uliana, M., and L. Legarreta, 1993, Hydrocarbons Habitat in a Triassic-to-Cretaceous Sub-Andean Setting: Neuquén Basin, Argentina: *Journal of Petroleum Geology*, v. 16, p. 397-420.
- Urai, J., G. Nover, C. Zwach, R. Ondrak, R. Schöner, and B. M. Kroos, 2008, Transport processes, in R. Littke, U. Bayer, D. Gajewski, and S. Nelskamp, eds., *Dynamics of complex intracontinental basins: The Central European Basin System*: Berlin, Springer-Verlag, p. 367–388.

- Verwer, K., G. P. Eberli, and R. J. Weger, 2011, Effect of pore structure on electrical resistivity in carbonates: *AAPG Bulletin*, v. 95, no. 2, p. 175–190, doi:10.1306/06301010047.
- Vittore, F., D. T. Licitra, J. Quiroga, A. Rosensblat, and E. Lovrinchevich, 2014, Caracterización Estructural, Estratigráfica y Sedimentológica de la Fm Vaca Muerta en el Yacimiento Loma Campana, Cuenca Neuquina, Argentina: IX Congreso de Exploración y Desarrollo de Hidrocarburos, Simposio de Recursos No Convencionales: Ampliando el Horizonte Energético, Instituto Argentino del Petróleo y el Gas, Mendoza, p. 653-672.
- Wagner, K. W., 1914, Erklärung der dielektrischen Nachwirkungsvorgänge auf Grund Maxwellscher Vorstellungen: *Electrical Engineering (Archiv für Elektrotechnik)*, v. 2, p. 371-387.
- Wang, K., J. Sun, J. Guan, and Y. Su, 2005, Percolation network modeling of electrical properties of reservoir rock: *Applied Geophysics*, v. 2, no. 4, p. 223–229, doi:10.1007/s11770-005-0028-2.
- Wang, H., and A. Poppitt, 2013, The Broadband Electromagnetic Dispersion Logging Data in a Gas Shale Formation: A Case Study: SPWLA 54th Annual Logging Symposium.
- Wardlaw, N., and J. Cassan, 1978, Estimation of recovery efficiency by visual observation of pore systems in reservoir rocks: *Bulletin of Canadian Petroleum Geology*, v. 26, p. 572–585.
- Washburn, E. W., 1921, Note on a method of determining the distribution of pore sizes in a porous material: *Proceedings of the National Academy of Sciences of the United States of America*, v. 7, no. 4, p. 115–116, doi:10.1073/pnas.7.4.115.
- Waxman, M., and L. Smits, 1968, Electrical conductivities in oil-bearing shaly sands: *Society of Petroleum Engineers Journal*, v. 8, p. 107-122.
- Webb, P. A., 2001, An introduction to the physical characterization of materials by mercury intrusion porosimetry with emphasis on reduction and presentation of experimental data: Norcross, Georgia, Micromeritics Instrument Corp, 22 p.
- Weger, R. J., 2006, Quantitative pore/rock type parameters in carbonates and their relationship to velocity deviations: Ph.D. dissertation, University of Miami, Coral Gables, Florida, 232 p.
- Weger, R. J., G. P. Eberli, G. T. Baechle, J. L. Massafiero, and Y.-F. Sun, 2009, Quantification of pore structure and its effect on sonic velocity and permeability in carbonates: *AAPG Bulletin*, v. 93, no. 10, p. 1297–1317, doi:10.1306/05270909001.

- Weller, A., and F. Börner, 1996, Measurements of spectral induced polarization for environmental purposes: *Environmental Geology*, v. 27, p. 329-334.
- Weller, A., S. Nordsiek, and W. Debschütz, 2010, Estimating permeability of sandstone samples by nuclear magnetic resonance and spectral-induced polarization: *GEOPHYSICS*, v. 75, p. E215-E226.
- Weller, A., and L. D. Slater, in press, Induced polarization dependence on pore space geometry: Empirical observations and mechanistic predictions: *Journal of Applied Geophysics*.
- Westphal, H., G. P. Eberli, L. B. Smith, G. M. Grammer, and J. Kislak, 2004, Reservoir characterization of the Mississippian Madison Formation, Wind River basin, Wyoming: *AAPG bulletin*, v. 88, p. 405-432.
- Worthington, P. F., and F. A. Collar, 1984, Relevance of induced polarization to quantitative formation evaluation: *Marine and Petroleum Geology*, v. 1, p. 14-26.
- Zeller, M., 2013, Facies, Geometries and sequence stratigraphy of the mixed carbonate – siliciclastic Quintuco – Vaca Muerta system in the Neuquén, Argentina: An integrated approach. Ph.D. University of Miami, Open Access Dissertations. Paper 1099, 202pp.
- Zisser, N., A. Kemna, and G. Nover, 2010, Relationship between low-frequency electrical properties and hydraulic permeability of low-permeability sandstones: *Geophysics*, v. 75, p. E131-E141.